공학박사학위논문

항공기 착빙 형상 예측을 위한 통합 해석 프로그램 개발

Development of Integrated Icing Shape Analysis Platform for Generic Aircraft

2018 년 2 월

서울대학교 대학원

기계항공공학부

손 찬 규

Abstract

Development of Integrated Icing Shape Analysis Platform for Generic Aircraft

Chankyu Son
School of Mechanical and Aerospace Engineering
The Graduate School
Seoul National University

Federal Aviation Regulations specify the aircraft class according to the maximum takeoff weight and the number of seats. The regulations present icing environments for the certification of airworthiness. Most aircraft icing studies are on fixed-wing aircraft, which has more than ten passengers by following Federal Aviation Regulations Part 25. The flight speed was focused on the stall speed of the presented aircraft in the regulations. In the case of rotorcraft aircraft, it follows the regulations and icing environments established for the fixed-wing aircraft. Moreover, there are no regulations for unmanned aerial vehicle (UAV). Under the regulations, research on aircraft icing has the following problems.

First, the characteristics of icing shapes are not clear except for the aircraft types and regulations presented in regulations. It is difficult to apply the previous research

results on the stall speed of fixed-wing aircraft to other aircraft, which is operating with low-speed, because the non-dimensional parameters governing the icing shape are in unknown. Therefore, it is necessary to analyze the characteristics of the icing shapes and its aerodynamic performance on the aircraft having the different mission profile.

Second, it is the ultimate goal for aircraft icing research to determine the aviation safety of aircraft under given weather conditions. However, there have been no integrated procedures or methods for assessing the safety of aircraft. Under the given icing environment, icing research has been separately performed by following areas: the prediction of icing shape, the performance prediction of deformed shapes, the design of anti-/de- icing device, and the evaluation of operation safety.

Third, simulation tools have been developed focusing on fixed-wing aircraft. There is no accurate numerical tool to predict the ice shapes on helicopter fuselage. It is essential to consider the rotor-airframe interaction. However, in the latest icing research, the technique performed to the fixed-wing aircraft is directly applied to helicopter fuselage. For example, the icing wind tunnel tests for the helicopter fuselage neglected the rotor blades. In numerical research, the simple inflow model which can not account for the blade tip vortices was applied. It is necessary to develop an accurate icing analysis solver to evaluate the validity of previous research results that ignored the rotor effects, and by using the accurate code, the icing characteristics should be identified under the conditions of rotor-airframe interaction.

To this end, Ice Shape Estimation and Performance Analysis Code (ISEPAC), a simulation program to analyze icing phenomena occurring on the three-dimensional

body, is developed by applying the latest numerical technique. ISEPAC is a second-generation icing analysis tool that is based on the Navier-Stoke equations, Eulerian droplet field calculation, and Messinger model with a shallow water film. ISEPAC can handle not only for the fixed-wing aircraft but also for the helicopter fuselage including rotor wake effects. The latest actuator surface model loaded on ISEPAC is able to capture the behavior of individual blade tip vortices. By using ISEPAC, the icing characteristics of HALE aircraft and helicopter fuselage are analyzed. As a result, the following conclusions were drawn.

First, there are no ice horns on HALE aircraft and helicopter fuselages with low-speed flight (Mach number less than 0.1). The droplet with small inertia can avoid the body without collision, resulting in a small amount of water film on the surface. The generated water film flows by the shear force of the air, and concentrates on a specific region. At this time, the heat transfer is predicted to be small due to the low-speed characteristic, and only some of the concentrated water freeze. Therefore, the ice horn cannot be observed.

Second, a new procedure is proposed to determine whether an aircraft can be operated at the given icing environment for HALE aircraft which does not have anti-/de- icing devices due to the ultra-light design. Preferentially, the ice shapes and its aerodynamic performance changes are obtained from ground to the mission altitude in the climbing stage under the given icing conditions. Then, the quantitative correlation between aerodynamic performance coefficients and icing environment variables was established. It was possible to judge the success of the mission by comparing the required power and the mounted battery to reach the mission altitude.

The fixed-wing aircraft with high-speed is known to generate ice horns at high temperatures; thereby, the risk increases at high temperatures. However, ice horns cannot be observed under the stratiform clouds for HALE aircraft even in high temperature conditions. Since there is no ice horn, the high-risk region of HALE aircraft is diffident from that of fixed-wing aircraft. The high-risk region of icing for HALE aircraft appears under high humidity and low-temperature conditions.

Third, when analyzing the icing on the body of the helicopter, accurate flow analysis should be accompanied. A relatively high-pressure and low-velocity region is formed under the rotor surface and above the fuselage. Due to the low-velocity region that is induced by rotor wake, the droplet trajectories and heat transfer rate are different from the cases of isolated fuselage. Consequently, the differences of the total amount of ice and the ice distribution are clearly distinguished between the isolated fuselage and including rotor wake effect. In addition, a large amount of icing occurs in the area where the tip vortex collides the body. This meant the necessity of the accurate simulation code that can predict the generation, movement, and collision with fuselage of the individual tip vortex.

Keywords: Aircraft Icing, High-Altitude Long-Endurance Aircraft, Helicopter Fuselage, ISEPAC, Actuator Disk Method, Actuator Surface Method, Regression Analysis

Student Number: 2012-30182

Contents

List of Figures

List of Tables

1. Introduction

1.1 Overview of Aircraft Icing

When the aircraft operates in cold and humid environments, super-cooled droplets in the atmosphere collide with the aircraft surface, resulting in ice being accreted on the outer structure surfaces such as the wings, fuselage, engine intake, and other exposed parts of aircraft. Due to the ice accretion on the aircraft surface, the shape of aircraft is deformed. The icing on aircraft surface depletes the overall performance and leads to catastrophes in severe cases.

The accumulated ice can be divided into three categories called glaze, rime, and mixture ice (Fig. 1.1) [1]. The type of ice on a surface depends on the meteorological parameters such as humidity (Liquid Water Contents, LWC), size of droplets (Median Volume Diameter, MVD), and temperature. It is well known that the ambient temperature plays an important role in determining the type of ice.

Glaze ice usually occurs in high-temperature condition. The impinged droplets form water film on the surface. Then a partial of water film freezes due to the convective heat transfer. The remainder of water flows along the surface by the shear of air. The first feature of glaze ice is that the ice on the surface is transparent because the pure water freezes without air pocket. Ice horn is the second feature of glaze ice as shown in Fig. 1.2. Most of the flowing water which remains on the surface freezes where the heat convection is high. Now that the high-velocity region induces elevated heat transfer rate, the ice horn is formed on the suction side with a positive angle of attack.

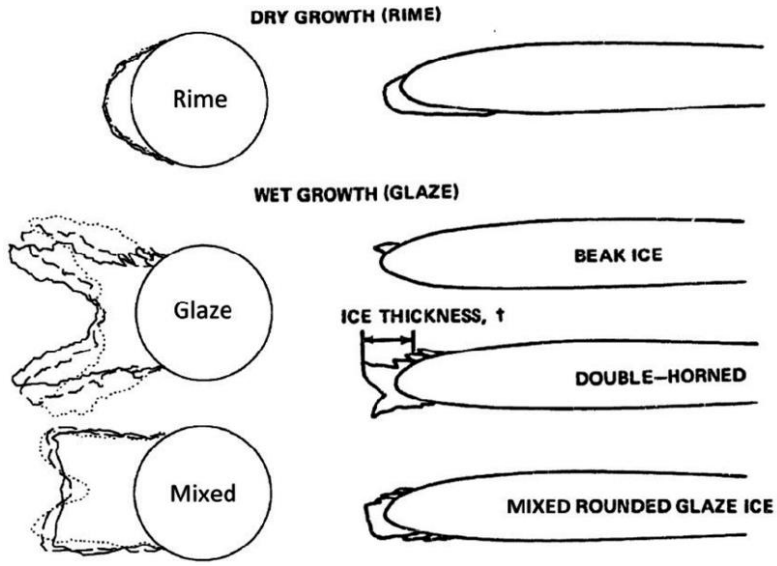

Fig. 1.1 The type of ice on the cylinder and airfoil [1]

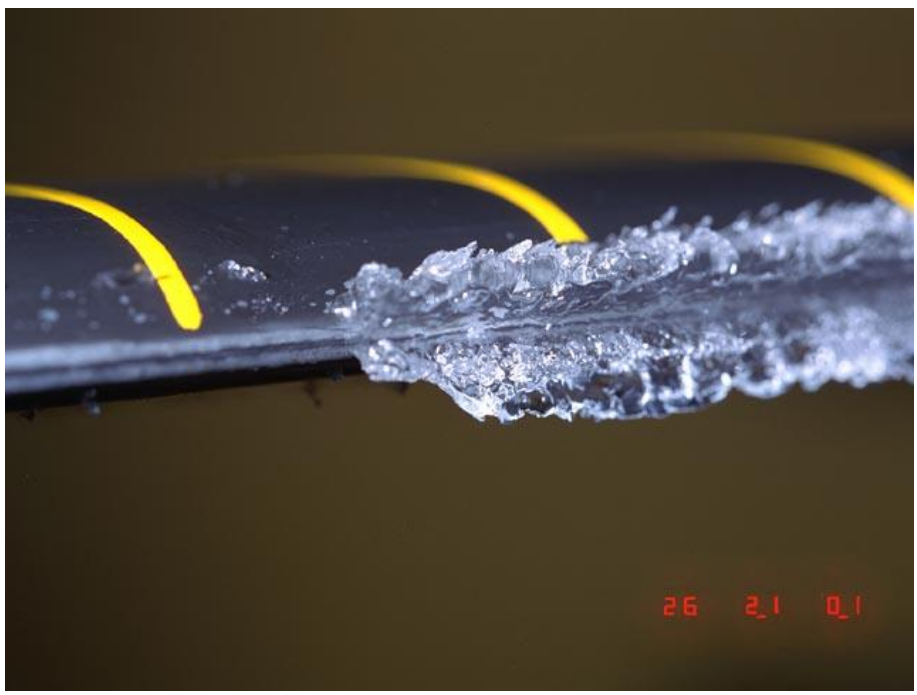

Fig. 1.2 Example of the glaze ice shape obtained by icing wind tunnel [1]

Rime ice, on the other hand, appears under low temperature. The water droplets immediately freeze when they impact on the surface without water film. The smooth ice shape is developed without the ice horn. Air pockets are placed in the intervals of ice crystals while the phase of water droplets is changed. Thus, the ice-covered area is opaque as shown in Fig. 1.3.

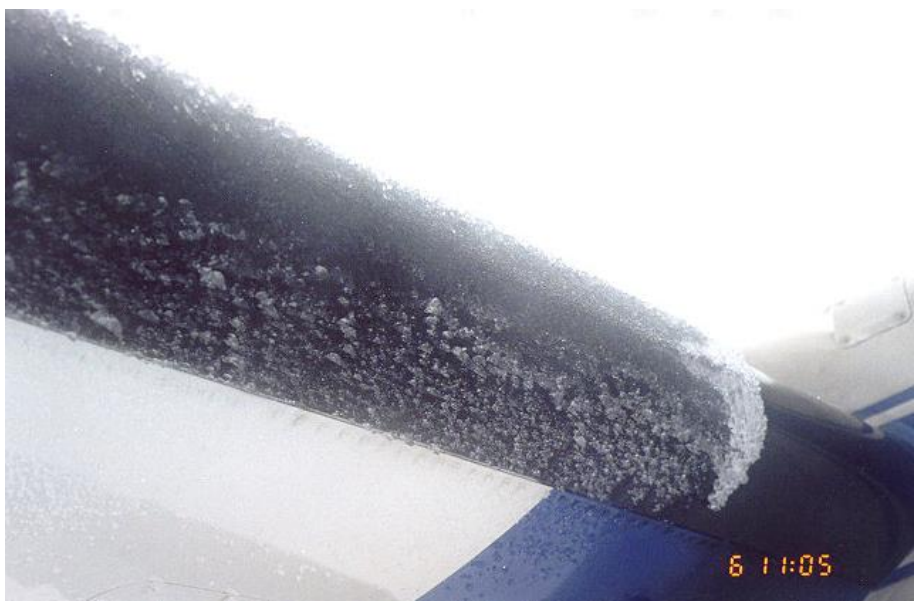

Fig. 1.3 Example of the rime ice shape obtained by natural icing flight (Photo by NASA Lewis research center)

It is difficult to classify the exact icing type because the glaze ice occurs near the stagnation region, and the rime ice appears in the area away from the stagnation region. The stagnation region has droplets of the high kinetic energy with low convective cooling; therefore, transparent glaze ice occurs as shown in Fig. 1.2. On the other hand, rime ice forms far away from the stagnation point. At that region, the

droplet immediately freezes due to high convective cooling and low kinetic energy. Therefore, mixture ice, in which glaze and rime ice coexist, is mainly present in most of the icing conditions.

Examples of the effect of ice accretion on the lift and drag of an airfoil are shown in Fig. 1.4. As long as the ice is accumulated on the wings in the initial state under icing conditions, the surface roughness is increased. Although there is no significant difference in leading edge shape, the surface roughness (1/1300 of the chord), the maximum lift coefficient drops by 18%. When the glaze ice which deforms the leading edge shape occurs, the maximum lift coefficient decrease by 40%, and maximum lift angle changes from 15.2° to 8.1°.

When in-flight icing occurs, increasing the drag also becomes a serious problem. As shown in Fig. 1.5, a relatively flat drag coefficient is maintained from the angle of attack of 0° to 6° for the clean airfoil. However, the zero-lift drag for the ice accumulated airfoil is increased about 138% compared to the clean airfoil. At the 6° angle of attack, the drag coefficient of ice accumulated airfoil soars by 452% due to the flow separation at the tip of the ice horn.

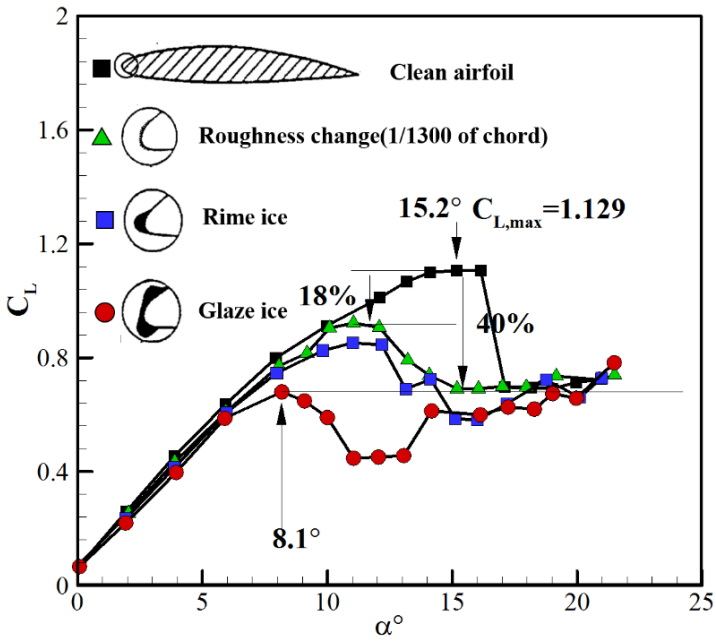

Fig. 1.4 Typical effect of ice accretion on airfoil lift [2]

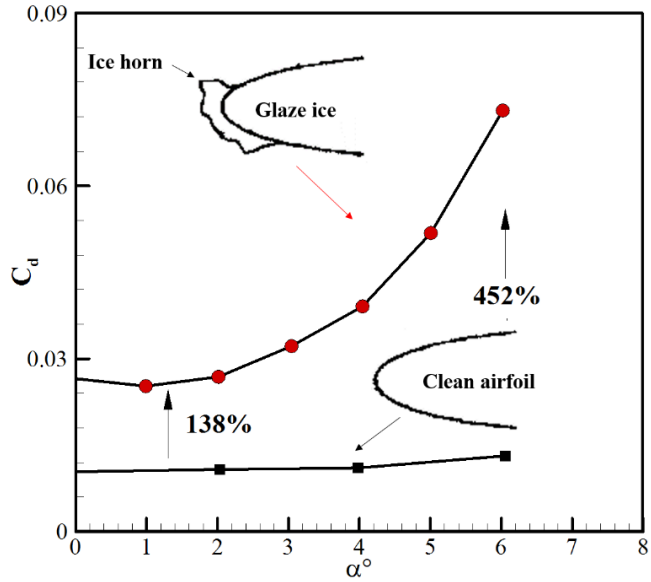

Fig. 1.5 Typical effect of ice accretion on airfoil drag [2]

Aircraft icing has a negative impact on operational safety as well as reduced aerodynamic performance. An example from the AGARD reported that a 35% loss in maximum lift leads to 24% increase in stall speed, which is significant in relation to the 13% margin generally allowed for operations in the clean airfoil [3]. The increased stall speed causes the loss of controllability. Thus aircraft icing is a critical issue in terms of operational safety.

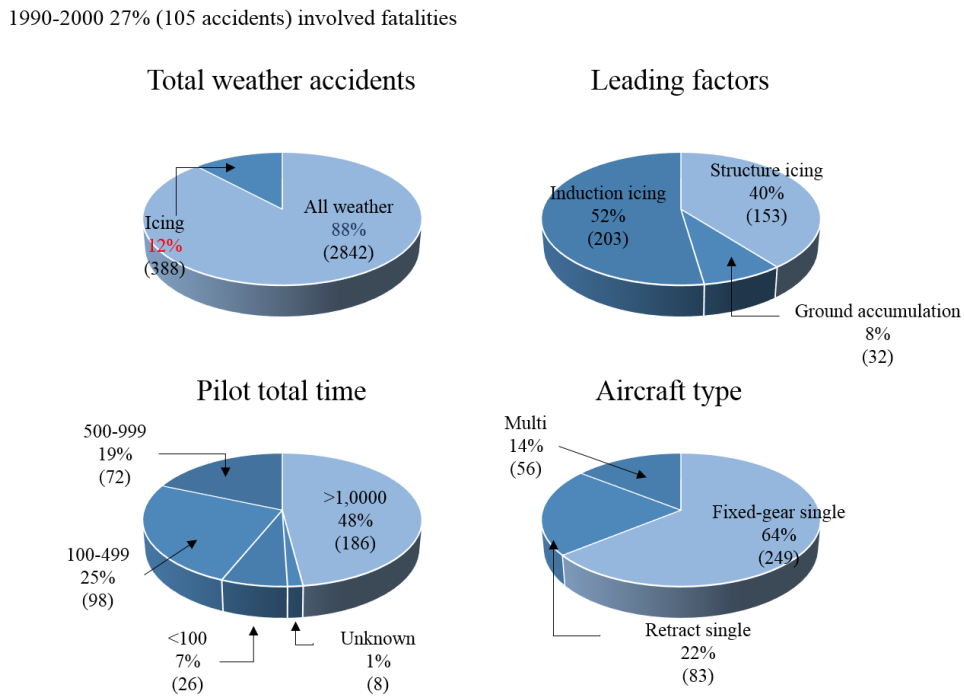

Fig. 1.6 The number of aircraft icing accidents and causes [4]

Fig. 1.6 summarizes the report published by Aircraft Owners and Pilots Association (AOPA). According to the report [4], the number of aircraft accidents

was 3230 in U.S. from 1990 to 2000. Twelve percent of these aircraft accidents were related to aircraft icing. Forty percent of aircraft icing accidents corresponded to ice accretion on external structures such as main wings [4].

In recent years, on February 12, 2009, Colgan Air Flight 3407, marketed as Continental Connection under a codeshare agreement with Continental Airlines, collapsed in the residential area of Buffalo, New York, resulting in 50 deaths. Fig. 1.7 depicts the scene at the time of the accident. National Transportation Safety Board (NTSB) [5] reported that the ice was accumulated on the main wings and windshield before the crash, and the aircraft was flying on an autopilot under the icing condition.

Table 1.1 shows forty accidents or incidents, which were related to in-flight icing on the wings, fuselage or control surfaces from 2006 to 2010 in U.S. During the same period, NTSB and NASA Aviation Safety Reporting System (ASRS) reports showed 228 icing-related accidents and 30 inflight icing-related incidents from 2006 to 2010. Forty of the accidents were directly related to in-flight icing occurring on the wings, fuselage or control surfaces [6].

Table 1.1 Inflight Icing Accidents (2006 to 2010) [6]

No	Date	Place	Aircraft No.	Report ID
1	12/25/2010	Troy, MI	N385AS	CEN11CA135
2	11/5/2010	Winchester, TN	N7SY	ERA11LA048
3	10/25/2010	Lander, WY	N201HF	WPR11FA032
4	10/21/2010	Greenbush, ME	N5118J	ERA10LA105
5	2/23/2010	Springfield, KY	N7778W	ERA10FA148

6	1/6/2010	Kearney, NE	N206AV	CEN10LA090
7	12/6/2009	Dodge City KS	N108L	CEN10LA068
8	11/20/2009	Susanville, CA	N2650R	WPR10LA059
9	5/6/2009	Bethel, AK	N629SP	ANCO9LA038
10	3/10/2009	Aberdeen, SD	N402BP	CEN09LA206
11	2/12/2009	Clarence Center, NY	N200WQ	DCA09MA027
12	1/17/2009	Lafayette, IN	N6509T	CEN09CA136
13	1/15/2009	Wray, CO	N840NK	CEN09FA135
14	1/6/2009	Three Rivers, MI	N92WT	CEN09LA122
15	12/19/2008	North Canton, OH	N9299N	CEN09FA099
16	11/29/2008	Rock River, WY	N6693A	WPR09CA051
17	11/14/2008	Napaskiak, AK	N36CF	ANC09LAO12
18	5/8/2008	Snow Hill, NC	N101BX	NYCO8LA176
19	3/16/2008	Atkins, VA	C-FRSK	NYCO8FA139
20	2/8/2008	Albany, OR	N329BW	SEA08LA072
21	12/10/2007	Salmon, ID	N925TT	SEA08FA042
22	11/18/2007	Nikolai, AK	N170BP	ANCO8CA020
23	10/7/2007	Naches, WA	N430A	LAX08MA007
24	10/7/2007	Ekalaka, MT	N85WT	SEA08FA006
25	6/28/2007	Wellsville, MO	N477MD	CH107FA183
26	4/14/2007	Vibumum, MO	N8969J	CH107FA102
27	3/17/2007	Beverly, MA	N511AT	NYCO7LA081
28	2/9/2007	Hinesville, GA	N506BC	ATLO7FA040
29	2/9/2007	Great Bend, KS	N45GM	DEN07FA059
30	1/12/2007	Harbor Springs, MI	N425TN	CH107LA059
31	12/26/2006	Johnstown, PA	N400CS	NYCO7FA051
32	12/26/2006	Jasper, TN	N55MB	CH107FA046
33	12/17/2006	Bucyrus, OH	N9073P	CH107FA041
34	10/25/2006	Meadview, AZ	N121LD	LAX07FA021
35	9/15/2006	Maybell, CO	N787SL	DEN06FA131
36	5/4/2006	Lincoln, NE	N71MT	CHI06IA127
37	3/20/2006	Emporia, KS	N33AFC	DEN06LA050
38	1/25/2006	Carson, WA	N69KM	SEA06FA147

39	1/13/2006	Childersburg, AL	N87HK	ATLO6LA035
40	1/2/2006	Santa Maria, CA	N390AE	LAX061A076

The helicopter also suffers from the icing problems while operating in the high humidity and low-temperature condition. The helicopter is more vulnerable to icing than fixed-wing aircraft. Due to the short chord length of the rotor blades, the size of the ice on the blades is relatively bigger than that of wings on fixed-wing aircraft. The accumulated ice on the rotor systems leads to increased vibration, rapid loss of lift and a substantial power increase to sustain flight. Shed ice from the spinning rotor is common and creates dangerous projectiles.

In terms of flight safety, the icing on the fuselage also becomes a serious problem. Because fuselage contains engine intake, sensors, and windshield, the ice on the fuselage also raises following issues: inaccurate data acquisition, low-quality flow to the engine intake, and obstructing the pilot's field of vision.

A survey undertaken during 2000/2001 on U.S. Army aircraft icing reveals that more than half of the U.S. Army commanders stationed in Europe, Korea, and several forts in the U.S. consider in-flight icing to have an above-moderate impact on a mission accomplishment [7]. One unit in Ketterback, Germany, reports that 11–25% mission disruptions were due to the unexpected icing encounters. The U.S. Army deals with the in-flight icing problem by not scheduling any missions between December and February over affected areas or by canceling the scheduled missions beforehand based on conservative icing forecasts.

Fig. 1.7 The scene of accident on February 12, 2009, Colgan Air Flight 3407

To prevent aircraft accidents and incidents, transport category airplanes should prove the airworthiness under the icing conditions. The type of transport category airplanes is presented by Title 14 Code of Federal Regulations (14 CFR) Part 25 [8]. Transport category airplanes are either: jets with 10 or more seats or a maximum takeoff weight (MTOW) greater than 12,500 pounds (5,670 kg); or propeller-driven airplanes with greater than 19 seats or a MTOW greater than 19,000 pounds (8,618 kg). For aircraft smaller than the mentioned regulation in Part 25, they are classified in Part 23. Rotorcraft is classified as Part 29.

Specific icing envelope to certify the airworthiness is presented in Appendix C in 14 CFR Part 25. Aircraft under Part 23 and Part 29 also follows the same icing envelope with Part 25.

Most aircraft associated with Part 23, Part 25, and Part 29 equip anti-/de-icing devices. In order to efficiently and effectively design the anti-/de-icing devices, aircraft manufacturers predict the ice accretion shapes on the aircraft and examine the performance of the ice accumulated aircraft. When they have obtained the ice

accretion shapes, and its aerodynamic performance of the aircraft, both experimental and numerical approaches are used.

The icing experiments are performed by icing wind tunnel or natural icing flight tests. The icing wind tunnel tests for scale models are limited because the similarity parameters such as Mach number and Reynolds number are not apparent in icing research fields, and scaling methodologies are not fully developed [9]. The enormous size of the facility which can include full-scale models is inevitable. It leads a lot of cost for acquisition and maintenance. The natural icing tests are difficult to find the icing cloud and control the ambient conditions. Further, it is dangerous because the test aircraft that has not been fully certified in icing environments. The primary constraint of both icing wind tunnel and natural icing flight tests is the number of test cases. Both approaches require a lot of resources in common to find the critical icing condition. To overcome these limitations of the icing experiments, numerical simulations have been widely used for the icing certification campaigns, since the 1980s.

1.2 Icing Simulation Codes

As shown in Fig. 1.8 Typical structure of the icing simulation codes, most icing analysis programs developed so far consist of four modules – 1) flow analysis module, 2) droplet-trajectory calculation module, 3) thermodynamic module, and 4) grid-regeneration module. It can be divided into the first generation and the second generation according to applied methodologies of each module and target objects.

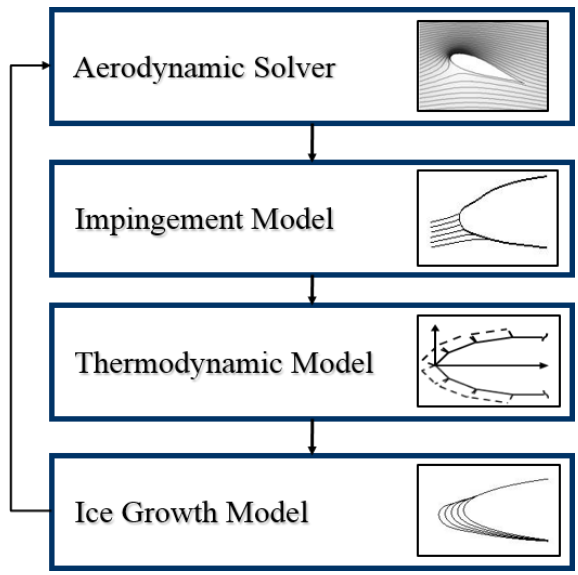

Fig. 1.8 Typical structure of the icing simulation codes

The first generation tool was based on two-dimensional (2D) airfoils. It used inviscid and incompressible aerodynamic solvers such as panel method. The Lagrangian approach was employed for the droplet-trajectory calculation module. Thermodynamic module adopted a 2D Messenger model [10].

The second generation tool was based on the compressible viscous Navier-Stokes equations. Three-dimensional (3D) Eulerian approach was applied for the droplet-trajectory calculation module. To handle the movement of the water film on the surface for both chord-wise and span-wise direction, the water film assumption was included in the Messiger model for the thermodynamic module. The characteristics of the representative tools and the detailed methods for each generation are described in the following parts 1.2.1 and 1.2.2.

1.2.1 First generation codes

Due to the development of computing technology, the prediction of ice shapes has been actively pursued through numerical analysis since the 1980s. The analysis codes have been mainly led by the government-funded research institutes.

NASA has developed a program that can analyze icing shapes and its aerodynamic performance based on the Hess-Smith 2D Panel Method called LEWICE [11], [12]. It was later updated to LEWICE / IBL (Interactive Boundary Layer) which was the modified by Cebici [13] to consider the viscosity effects. Potapczuk improved the aerodynamic module from panel method to 2D Euler equations to consider the compressible effects, and then enhanced version, LEWICE / E, was published. LEWICE / E was performed under Mach number of 0.58 as an example case in 1992 [14]. As modifying the code, the accuracy of the aerodynamic module has been improved. However, LEWICE consistently employed the Lagrangian approach to calculate the trajectories of the droplets, and Messinger model [10] is adopted as a thermodynamic module.

In 1986, the ONERA (Office National d'Etudes et Recherche Aerospatiales) in France began research on icing phenomena in collaboration with NASA and the Defense Research Agency (DRA) [15]. Based on the accumulated research results, a program was developed by Hedde and Guffond in 1995 for 2D and 3D icing shapes and its aerodynamic performance analysis [16]. They used 3D panel method or Euler equations as the aerodynamic solver. Mixing length theory coupled with strip-line

theory is applied to consider the heat transfer and viscosity of air. The ONERA icing code also used the Lagrangian approach to calculate the droplet trajectories. However, they extended the method to calculate the collection efficiency from 2D to 3D with the assumption that the directions of thin water film and the shear force of air are the same, the 3D analysis is performed indirectly in the thermodynamic module.

In 1990, the DRA in U.K., which was working on the icing phenomenon with the U.S. and France, developed a 2D analysis program called TRAJICE [17]. It is similar to NASA's LEWICE, but the heat transfer calculation is modified so as to take account of the compressibility effect and the conductive cooling is modified in the thermodynamic module to be influenced by the surface pressure. To improve the accuracy of long-term exposure time, multiple time interval approach was devised. TRAJICE adopted the different time interval in each time step [15].

A code similar to LEWICE, CANICE, was developed jointly by Ecole Polytechnique Montreal and Bombardier Aerospace [18]. The extension of this code to multi-element airfoils is described by Tran et al. [19]. The 2D panel method is used to analyze the flow field around the 2D airfoil, and the Karman-Tsien method is used to compensate for the compressibility effect. Modification of the Messinger model [18] is used as a thermodynamic module. The basic algorithms of these codes are similar to LEWICE. The modifications consisted of a correction for multiple stagnation points, a mass conservation scheme for the ice accretion, a stability limit for the allowable time step at each layer, a sublayer scheme for ice growth, and a

dual grid scheme to use different grid densities. These modifications are described in detail by Pueyo et al. [20].

The first generation tools opened the way for the idea of the structure to predict the ice accretion shapes on the 2D airfoil, but it had the following problems. First, the codes are based on the inviscid aerodynamic solver. By using the boundary layer theory, the viscous effects are correlated. Inherently, the inviscid solvers have a limitation in the high angle of attack that causes flow separation.

Although the inviscid solvers coupled with boundary layer theory was applicable for the low angle of attack, which does not make the massive separation, eventually the flow separation occurs at the tip of the ice horn as the ice horn grows under glaze ice conditions. The droplet trajectory module also has limitation to the flow separation. The dividing streamline of air is formed by the flow separation condition. Because the trajectories of the droplets are calculated from the far field, the droplet path line follows the dividing streamline. As a result, there are no particles inside the dividing streamline.

Second, the first generation codes were developed for 2D analysis (especially 2D airfoil). Using the strip-line theory, the solvers were extended from 2D to 3D. Together with the flow separation problems, there are limits to the wing tip region or fuselage where the 3D effect is dominant for the aerodynamic and droplet field modules. In addition, the 2D thermodynamic module based on the boundary layer theory requires the stagnation point as a starting point of the water film. The direction of the water film is assumed from the stagnation point to the trailing edge. However,

it is difficult to define the stagnation line and strip-line which are required to determine the direction of water film for the generic 3D problems.

1.2.2 Second generation codes

Due to the advancement of computing technology, flow analysis using CFD based on Navier-Stokes equations has been widely performed since the 1990s. As a result, the icing analysis programs were extended to Navier-Stokes equations from inviscid solvers. The 2nd generation solver which is based on the Navier-Stokes equations can consider the viscosity of air, and treat the generic 3D problems.

FENSAP-ICE is the most advanced 2nd generation icing simulation code. It was developed by McGill University [21]. FENSAP-ICE is consists of two parts. The first part, FENSAP (Finite Element Navier–Stokes Package), is responsible for air solver [22]. The second part takes charge of the impinging and thermodynamic module. The name of the impinging module is DROP3D [23], and the thermodynamic module is ICE3D [21]. FENSAP is based on Navier-Stokes equations using finite element method. It can consider viscous and compressible flow.

The turbulence model serves the changes in surface roughness. FENSAP-ICE adopts modified Spalart-Allmaras turbulence model which can handle the surface roughness [24]. An Eulerian approach is used for solving the droplet fields in 3D space. General droplet physical assumptions are used to model mass and momentum conservation equations. Source terms such as gravity, buoyancy, and droplet drag were considered in modeling. The discretization of droplet equations also follows

the same approach as in FENSAP. Finally, the ice shape is determined by ICE3D solver which is based on shallow water icing model (SWIM). By managing the thin water film driven by the shear force of air as convection term, the directions and amount of runback water can be captured. The time-derivative PDE based Messinger model enables the transient behavior of an ice accretion.

In 3D ice accretion modeling as a 2nd generation code, another attempt was named ICECREMO developed in U.K. [25]. ICECREMO is a collaboration project between British Aerospace, Rolls-Royce, GKN-Westland Helicopters Limited, and DERA. ICECREMO is a 3D ice accretion model, based on a structured approach. It does not include a CFD solver and therefore may be used in combination with a range of CFD packages. The code consists of a Lagrangian particle tracking module, a splash and bounce module, a water film thickness and motion module, a heat transfer module, and a freezing module. ICECREMO specially modified the theoretical thermodynamic model to deal with the problem of ice accretion when flowing water film occurs [26]. Messinger model [10] is that the ice and water layers are isothermal, and so conduction through these layers cannot be accounted for [27]. ICECREMO involves solving heat equations in the ice and water layers. At the moving ice/water interface, the energy balance leads to a phase change or Stefan condition, which takes the form of a first-order ordinary differential equation. This contains all of the terms of the standard Messinger model, as well as conduction terms between the layers. However, the accuracy of the ice shapes was not significantly improved despite the complexity of the numerical methods and the

increased number of governing equations. Due to the flow and impact of incoming droplets, the water layer may be well mixed, in which case the isothermal assumption may be approximately valid with glaze ice.

1.3 Implications and Motivations

In just 30 years, the icing analysis techniques have made great strides. The accuracy of numerical simulation codes have been improved, and the simulation targets have been expanded from 2D airfoil to 3D arbitrarily body such as full 3D aircraft that includes main and tail wings, and fuselage. The distinct techniques to obtain the ice accretion shapes on the helicopter blades and fuselage have yet to be established but are in the process.

The simulation codes have been transformed from academic research to practical applications. To avoid risks of natural icing flight tests, the 3D ice shapes can be predicted, and then the degradation of aerodynamic performance is estimated by using simulation programs. In addition, manufacturers can dramatically reduce the number of icing wind tunnel tests or flight icing tests by performing the simulation. Through a number of simulations, it is possible to predict the critical icing condition that is dangerous to conduct the flight icing tests. Ultimately, it aims to replace the experiment for the certification campaign. Recently, the numerical simulation code, FENSAP-ICE, is extended to aid the icing certification campaign for Fairchild RC-26B [28]. The CANICE code provides ice catch data: collection efficiencies, impingement limits, stagnation point locations, and catch rates. This information is

used to guide the sizing and the design of the wing anti-icing system of Bombardier CRJ700 [29]. In addition, the flight simulator is also operated with the help of the program in a virtual icing environment [30]. Although reliable numerical techniques have been developed and applied to aid the certification campaign, the icing studies still have quantitative and qualitative limitations that should be solved soon. The following Parts (1.3.1 - 1.3.4) point out the limitations of the previous icing research, and remark the motivation and objectives of this study.

1.3.1 Partitioned Platforms

An integrated platform which can handle various problems is needed. The published icing simulation codes were combined with segregated modules based on various in-house codes under different platforms. For example, NASA LEWICE consists of an aerodynamic module, droplet trajectory module, and thermodynamic module. In the initial stage of development, LEWICE started from a single platform, but each module was separated so that it can only work on its own platform to handle various problems. To update the aerodynamic module from panel method to 3D Navier-Stokes equations, the aerodynamic module was separated from the first platform. Each droplet trajectory module was also subdivided. LWICE uses different droplet trajectory modules according to 2D and 3D problems, while they adopted the single thermodynamic module based on the strip line theory.

For 2nd generation codes, FENSAP-ICE was developed for the 3D general problems. Droplet trajectory module and thermodynamic model are coupled with a

single platform. However, the aerodynamic module was separated, when FENSAP-ICE was recently merged into ANSYS FLUENT. Therefore, FENSAP-ICE depends on the ANSYS FLUENT, and additional communication program is need to link both simulation codes. On the other hand, ICECREMO specialized in the thermodynamic module cannot extract ice accretion shapes by itself. It always requires an independent aerodynamic and droplet field solver to predict the ice accretion shapes.

The user of the above-mentioned icing simulation codes has to selectively combine each separate module according to the problems. The results obtained from each module should be derived to the other modules due to the loosely coupled modules. At this time, it is necessary to build an additional program to control the data transfer, which impedes calculation efficiency. Since the icing analysis requires iterative calculations, the computational efficiency is severely hampered for each iteration. Therefore, the icing simulation code should be able to handle the generic problems and be operated in a single platform that integrates the core modules: aerodynamic module, droplet trajectory module, and thermodynamic module. The integrated platform can guarantee the computation efficiency and user convenience.

1.3.2 Restricted Research Subjects

The icing characteristics under low-speed is in unclear. Most experiments and numerical simulations have focused on commercial fixed-wing aircraft because safety is considered the top priority. The regulations for icing certification have also been concentrated and established for conventional fixed-wing aircraft which

corresponds to Part 25 which is described in the previous Section 1.1. The aircraft manufactures should prove the airworthiness of their aircraft under the defined icing conditions in the regulations.

For helicopter, the regulations for icing certification is guided in Part 29. However, some parts were revised, but most part regulations for the icing certification in Part 29 follows the regulations of Part 25. In particular, the icing environment in Part 29 had been exactly same with Part 25 regardless of the mission profile. What is more serious is that there are no regulations for unmanned aerial vehicle (UAV). Due to these reasons, most icing studies have been conducted for the fixed-wing aircraft which is related to Part 25.

There are scarcely any facilities which can perform the icing research for full-scale model. NASA and CIRA possess the icing research wind tunnels, which can perform the icing tests for aircraft or its significant parts. The published results that are performed in those facilities have focused on the speed about Mach number 0.3 because the cruising speed or the stall speed of conventional aircraft. Even if they have released a lot of icing experiment data in the public domain, it is difficult to apply those results to the low-speed aircraft. In the absence of well-known non-dimensional parameters such as Mach, Reynolds, and Prandtl numbers, it is difficult to infer and expect the ice accretion shapes and types (rime or glaze ice) under the different velocity.

Although numerical simulations have an advantage that there is no restriction on the size of models, the icing simulation codes are rare in the public domain.

Moreover, the main object of the simulation codes was complement of icing wind tunnel and natural icing tests. Therefore, the results of numerical simulations have been also concentrated on the fixed-wing aircraft corresponding to Part 25.

In recent years, demand for not only fixed-wing aircraft but also low-speed aircraft such as helicopter, High-Altitude Long-Endurance (HALE) aircraft, and drone has been increasing. The numerical and experimental studies for low-speed aircraft icing are very limited.

To understand the icing characteristics of low-speed aircraft, this study focuses on the HALE aircraft and helicopter fuselage. The icing characteristics of low-speed aircraft can be derived by extracting the common feature of ice shapes on those aircraft. Furthermore, this study contributes to solve the problems faced by the aircraft icing on HALE aircraft and helicopter fuselage.

For HALE aircraft, this study proposes a novel procedure to quantitatively judge the operation limits under the icing environment. HALE aircraft is inherently vulnerable to icing because HALE aircraft does not equip the anti/de-devices for ultra-light design. It is essential to comprehend the operation limits, but there is not enough information for HALE aircraft.

The accurate ice accretion shapes on the helicopter fuselage can be predicted by considering rotor wake. For fixed-wing aircraft, both air and droplet fields have been faithfully performed by 2nd generation codes. However, the rotor wake is not considered or a simple model is applied for the rotor wake effects. This study aims to systematically reveal the rotor wake effects to the helicopter fuselage icing by

using the precise model which can handle the generation, collision with fuselage, and dissipation of the tip vortexes.

The following Parts 1.3.3 and 1.3.4 are described literatures and limitations of the previous icing research for HALE aircraft and helicopter fuselage. The motivations and objectives of this study highlighted on both HALE aircraft and helicopter fuselage icing problems.

1.3.3 HALE aircraft

HALE aircraft can be used to perform a variety of missions such as communication relay, real-time disaster surveillance, reconnaissance, and others. Multiple advantages offered by HALE aircraft have led to growing interest in their design, manufacture, and operation. However, in-flight icing that can occur during the climbing stage is one of the significant problems restricting the aircraft's all-weather capability.

In-flight icing poses serious safety concerns for the operations of HALE aircraft. First, there is no room for icing/deicing equipment because of the aircraft's lightweight design. Therefore, once icing occurs during the climbing stage, the ice accreted on the surface could remain for a long period of the mission, leading to a continuous low-efficiency flight. Second, the ice-covered area is wide because a HALE aircraft has long and slender wings, and the ice accretion on such high aspect ratio wings would increase the total weight of HALE aircraft and induce a change in the flutter boundary, possibly leading to a mission failure. Third, ice on the wings

and other control surfaces could substantially deteriorate aerodynamic performance, reducing the rate of climb (ROC) and increasing the required power: in the worst case, the aircraft may not be able to reach the designated mission altitude with its given battery capacity. Fourth, icing has an adverse effect on the stall speed and the stall margin, and increased stall speed due to icing is one of the common causes of weather-related aircraft crashes. Finally, the surface roughness due to icing can induce an early transition around the stagnation region. As is well known, a rapid transition may contribute to increasing the required power and reducing the flight endurance.

In an effort to ensure operational safety, a few studies have analyzed icing environments for HALE aircraft, ice accretion shapes, and flight safety. Vogel, G. N. [33] recognized that the icing condition is one of the major atmospheric conditions that limit the aircraft's all-weather capability and studied the impact of icing phenomena on operations for HALE aircraft. He investigated previous research on the icing of transport category airplanes and identified certain icing issues that could affect operations of HALE aircraft. He found that a low ROC due to accreted ice on the wings is a significant concern for operations of HALE aircraft, and he also mentioned the need for ice detecting equipment during operations. Since the 1990s, a few studies have been performed to predict the ice shapes that accrete on a HALE aircraft. Through numerical simulations, Iya et al. [34] investigated the ice shapes accreting on a HALE airfoil under rime and glaze icing conditions. They also obtained the ice accretion shapes on a HALE airfoil during climbing and to estimate

the time required to sublimate the accumulated ice at the mission altitude. Bottyán, Z. [35] aimed to develop an integrated meteorological support system for HALE aircraft based on atmospheric data to help operators to ensure flight safety. A series of icing analyses was performed using an analytic model constructed for cylinders of the same diameter with various leading edge radius representing different HALE airfoil configurations. In this way, it was possible to estimate qualitative performance degradation from the characteristics of the ice accretion shapes on the cylinders. It was expected that as the ice shape transitions from rime ice to glaze ice, the performance degradation becomes severe, and the potential hazard due to icing would increase as the lengths of the ice horns grow.

The icing research on HALE aircraft that has been performed to date has shown that there is an urgent need for an integrated meteorological support system for operators of HALE aircraft [33]. Toward the objective of minimizing the effects of ice accretion on mission performance, Srikumar, P. [36] suggested the necessity of developing a model to predict the ice formation as a function of flight conditions and associated incremental aerodynamic coefficients. In other words, operators should be able to clearly determine whether or not to operate the HALE aircraft under given icing conditions. However, developing such the model is difficult because of the following unresolved problems.

First, the meteorological and flight conditions used for the icing analysis must reflect actual mission profiles and specifications of HALE aircraft. In particular, transport category airplanes corresponding to be Title 14 CFR, Part 25 [8]. The flight

speed of transport category airplanes is around Mach 0.3. Furthermore, twin-jet transports cruise at Mach 0.8 or higher which corresponds to transonic speed. Those transport category airplanes, meanwhile, have a relatively high ROC compared to HALE aircraft. Previous studies that address problems of HALE aircraft icing [34], [35] had not considered the notable differences in MTOW, ROC, and flight speed between the HALE aircraft and transport category airplanes. They simply followed mission profiles and specifications of transport category airplanes.

The second challenge is that 3D icing analyses should be conducted in conjunction with 3D aerodynamic performance analyses. Previous research has mainly focused on predicting ice accretion shapes on a 2D airfoil [34] or cylinder [35]. Since HALE aircraft has straight and high aspect ratio wings, 2D or quasi-2D such as strip approach are probably sufficient for accurate ice-shape prediction. However, the previous studies [34], [35] qualitatively concluded the potential hazard due to icing without aerodynamic performance analyses. Therefore, fully 3D simulation including the fuselage, main wing, and tail wings is essential to provide not only accurate ice accretion shape but also an assessment of the effects of ice on aircraft performance.

Third, a quantitative relationship between meteorological parameters and aerodynamic performance must be identified [36]. The operators of aircraft can use equipment such as balloon-borne radiosondes, rawinsondes, profilers, satellite sounders, and radar to collect the necessary meteorological data, such as Liquid Water Contents (LWC), Median Volumetric Diameters (MVD), etc., to determine ice

accretion shapes and icing intensity. However, a massive number of experiments or numerical analyses are necessary to identify the quantitative correlations between atmospheric variables and aerodynamic performance coefficient, and to date, there have been only a few attempts to construct such a quantitative correlation.

Beyond the predictions of ice accretion shapes and aerodynamic performance, the present study proposes a novel procedure for HALE aircraft to determine the mission success or failure under given atmospheric and meteorological parameters. Toward this objective, a typical type of HALE aircraft with a maximum takeoff weight of 20 kg is selected [37]. The icing environment is constructed based on the mission profile of the selected HALE aircraft. From the given environment, the ice accretion shapes and resulting aerodynamic performance are obtained for 3D HALE aircraft configuration using an advanced 3D icing analysis. Then, response surface models (RSMs) are constructed to correlate meteorological parameters quantitatively, and the aerodynamic performance of the ice accreted HALE aircraft. Finally, instead of just evaluating the aerodynamic performance changes under various icing conditions, the total required power for the ice accreted aircraft to climb to the mission altitude is calculated and compared with the given battery capacity. The total required power is a practical indicator by which the operator can directly judge whether the mission is successful or not.

1.3.4 Helicopter Fuselage

The ice that is accreted on the helicopter fuselage causes a substantial performance reduction and is a threat to aviation safety. First, the accreted ice on the engine inlet or nacelle deteriorates the flow quality, resulting in performance reduction. Moreover, when the ice accretes on foreign object damage (FOD) screens that are designed to prevent the injection of debris, the mass flow rate may decrease unexpectedly, and abrupt engine stalling may occur. Second, when the windshield on the front fuselage experiences ice accumulation, it may obstruct the pilot's vision, possibly resulting in mission failure. Third, the loss of communication or mismeasurement may result from severe ice accumulation on sensors or communication devices. In addition, the weight of the fuselage may increase because of ice accretion. In particular, the lighter the helicopter, the greater is the likelihood that ice accretion will lead to mission failure [38]. Finally, the ice-accreted surface may undergo a substantial increase in drag. When the fuselage is exposed to icing conditions, the frictional drag increases because of the surface roughness. Moreover, depending on the ice geometry, there may be a massive separation, which would adversely affect the maximum range and endurance of the helicopter.

As mentioned above, ice accretion on the fuselage plays an important role in the performance and airworthiness of a helicopter. However, there have been few related studies on the fuselage icing. Recently, with the development of numerical analysis techniques as well as increased computational power, there have been a few studies

aimed at numerically predicting ice accretion and the subsequent performance degradation of helicopter fuselages.

Unlike the flow fields of fixed-wing aircraft, helicopter fuselages are positioned below the rotors and are affected by the rotor wake. Therefore, rotor inflow analysis is crucial to obtaining an accurate prediction of ice accretion on the fuselage. The induced inflow from the rotor may alter the droplet trajectory, resulting in a change in the areas of collision with the fuselage. Next, the droplet-trajectory analysis module and thermodynamic module are required to consider the 3D effects. Because a helicopter has a long slender rotor with a high aspect ratio, it is reasonable to assume that the 3D effects may be confined to the tip region. Hence, the extension of the 2D blade element theory (BET) method can be justified for rotor blades. However, it is not possible to apply this concept to the helicopter fuselage because 3D effects are inherent for the fuselage.

Szilderm, K. [39] attempted to predict the ice shape that is accreted on the Bell 412 helicopter fuselage without rotor effects, where the collection efficiency on the fuselage surface was calculated based on Euler equations and the Lagrangian droplet-trajectory calculation module. Heat transfer was not considered; hence, only rime ice was handled. Later, Szilder, K. extended his research to include the rotor inflow [40], and he monitored the alterations in the droplet trajectory, which were due to the rotor wake. However, their studies still relied on the Euler equations and Lagrangian droplet-trajectory module. As is well known, the Lagrangian-based droplet-trajectory module has an inherent limitation in that it is unable to predict the

collection efficiency in the massive separation region because the released droplets cannot penetrate this “shadow region.” Moreover, because of the absence of a thermodynamic module, it could not handle the glaze ice conditions.

Aliga, C. N. [41] assumed an unsteady flow field for the analysis of helicopter ice accretion. The numerical analysis was conducted using the commercial software, FENSAP-ICE, for the configuration with a two-bladed rotor and a cylindrical fuselage (Georgia Tech. model). FENCEP-ICE is based on Navier-Stokes equations for the flow-field analysis, Eulerian droplet-trajectory module. The unsteady rotor and fuselage icing code required extensive computational resources. They estimated the collection efficiency of the rotors and the fuselage at an instant in time. It was challenging to apply the 3D thermodynamic module to extract ice-accretion shapes.

Myong et al. [42] investigated the ice shape on a real-scale helicopter engine inlet by conducting an icing wind-tunnel test at the Centro Italiano Ricerche Aerospazilai (CIRA) and comparing the experimental results with the numerical results obtained from FENSAP-ICE. Because the primary purpose was the determination of the heat capacity of anti-icing devices, the downwash due to the rotor wake was not considered in this study.

The previous studies conducted up to now have several limitations. First, most of the studies attempted to predict ice shapes on the fuselage without including the rotor wake effects [39], [42]. Even when the rotor wake effects were considered, the ice accretion was simulated for relatively high-speed forward flights [40], where the rotor-wake effects are negligible. It was because it is costly and time-consuming to

perform simultaneous simulations for the rotor and fuselage. The effects of the rotor wake on the helicopter fuselage are dominant when hovering and low forward flight, and should be considered to obtain the correct ice shape in these flight conditions. Second, there have been theoretical issues concerning the numerical methods for the water-droplet trajectory and thermodynamic model. The Lagrangian method, which is commonly used for droplet-trajectory calculations, is unable to handle the separated flow region. In addition, some of the studies do not include the thermodynamic module, and therefore have the intrinsic limitation of being unable to handle the glaze ice.

Recently, ice-accretion analysis on the ROBIN body has been accomplished by Fouladi, H. [43], who applied the actuator disk model (ADM) coupled with the inflow model to determine the rotor effects, and the Eulerian droplet-trajectory module. For forward flights with advance ratios of 0.15 and 0.23, the thermodynamic module was applied for various icing conditions, and corresponding ice shapes were extracted. The aerodynamic performance analysis and weight analysis were also performed for the geometries. In Drees's linear inflow model [44], the rotor inflow was determined based on the thrust coefficient as a linear function of the radial and azimuthal locations on the rotor disk. Hence, the detailed local features induced by the interaction tip vortices and inboard sheets with the fuselage cannot be included in this inflow model, as they will have an adverse effect on the accurate prediction of the droplet trajectories and flow field.

The recent study [43] has focused mainly on the development of numerical techniques to predict the ice shapes accreted on the fuselage surface. However, it has limitations such as the low-fidelity rotor-inflow model. With this in mind, in the present study, an attempt to obtain the accurate prediction of the ice shape on the fuselage surface is made, along with up-to-date numerical techniques such as the high-fidelity rotor-wake method. This study aims to perform a systematic comparison of the different actuator models, namely the recently developed actuator surface model (ASM) [45] and the conventional ADM [46]. The ASM used in this study was developed by Kim [45], and it removes the ambiguity of setting the reference line at which the induced velocities are measured. While the ADM used by Fouladi, H. [43] can handle only steady flow fields, the current ASM can consider unsteady flow, in addition to modeling the formation and propagation of tip vortices from each blade.

The Eulerian droplet-trajectory module and 3D thermodynamic module were introduced using the water-film model to realize efficient and accurate prediction of ice accretion on the helicopter fuselage. The flow solver was validated using the fixed-wing aircraft DLR-F6, and because of the absence of available experiments, the computed ice shapes were compared with those obtained by FENSAP-ICE both quantitatively and qualitatively [65].

Based on the numerical analysis packages, a series of numerical calculations was performed to investigate the detailed aspects of ice shapes on the fuselage under the influence of the rotor wake. First, the wake effects due to the rotors on ice accretion

under icing conditions were examined. To this end, the difference in ice shapes was investigated in detail both with and without the wake effects. Next, the effects of existing rotor-wake models were carefully reviewed. In this study, ice-accretion analyses were performed for the same icing conditions using different wake models, ASM and ADM, and the effects of each model on the ice shapes were observed. Finally, it was targeted to elucidate the relations between the ice shapes and forward flight speed. Forward flight speed has dominant effects the bounds of the fuselage exposed to wake, leading to the change in the location and extent of ice accretion.

1.4 Summary

So far, the issues, problems, and literature were addressed, and motivations and objectives of this dissertation were derived in the previous Section 1.3. This study tried to solve the limitations of the previous icing simulation codes and to expand the research objectives.

The first aim of this study is to develop the integrated icing simulation solver that is constructed in the single platform to treat the generic icing problems. As the problems have been diversified, the core modules of up-to-date icing simulation codes have been divided from the initial platform. It can inhibit the computational efficiency and require manual works.

The second is understanding the icing characteristics under low-speed conditions. Despite the many challenges for low-speed aircraft that should be addressed, most research capabilities have been concentrated on the fixed-wing aircraft satisfying

PART 25. To expand the research subjects, HALE aircraft and helicopter are selected as the representative low-speed aircraft, and the ice accretions shapes are predicted by using the 2nd generation code. To draw the icing characteristics under low-speed flight, the common characteristics of the ice shapes on both low-speed aircraft are analyzed.

Third, this research suggests the novel procedure that can quantitatively judge the operation limits from the operator's point of view for HALE aircraft icing, beyond the prediction of ice accretion shapes and aerodynamic performance. In order to prove the usefulness of the suggested procedure, the new procedure is applied to a typical HALE aircraft. Through the results obtained in the process, the characteristics of icing and the overall performance changes in HALE aircraft could be understood. Finally, the icing environment which cannot perform the mission was quantitatively confirmed.

Lastly, the effects of the forward flight speed and rotor wake to the ice accretion shapes on the helicopter fuselage are systematically analyzed. The ice accretion shapes are analyzed with various forward flight including hovering, low- and high-speed forward flight. The up-to-date simulation codes, ADM and ASM, are applied for the rotor wake effects. Previous studies did not consider the rotor wake effect [39], or linear inflow model was applied for the rotor wake [43]. Since, the inflow model [43] yields distorted wakes for the condition of wake-body interaction, the previous research analyzed the ice accretion shapes for the high-forward flight speed. However, the proposed ASM and ADM calculate the inflow by the Navier-Stokes

solver without the inflow model, it is possible to analyze low-speed and hovering flight accompanying wake-body interaction. In addition, ASM can capture the generation and dissipation of the individual tip vortexes. Before achieving the research objective, the validity of the previous icing studies, which have been performed on isolated fuselage should be checked, and then the necessity of the accurate rotor aerodynamic solver will be proved by comparing the difference of ice accretion shapes between the results of ADM and ASM.

1.5 Scope of the Dissertation

This paper is organized in the following order: After the introduction of Chapter 1, numerical methods are described in Chapter 2. This chapter introduces the details about the 2nd generation ice accretion code named ISEPAC which is constructed on OpenFOAM platform with four modules: aerodynamic module, impingement module, and thermodynamic module, and ice growth module. The validation results of each module and the final ice shapes on a 2D airfoil, 3D aircraft, and helicopter fuselage will be presented.

Chapter 3 deals with the HALE aircraft icing problems. The suggested procedure to quantitatively decide the operation limits of a HALE aircraft under icing conditions. The characteristics of ice accretion shapes and its aerodynamic performance changes are discussed. The application results on the typical HALE aircraft will be presented.

The icing problems on the helicopter fuselage will be discussed in Chapter 4. First, the ice accretion shapes on the fuselage which includes and excludes rotor wake effects will be compared. Next, the results of ASM will be contrasted with that of ADM. Finally, the effects of the forward flight speed form hovering to high advance ratio will be analyzed in sequence.

In Chapter 5, both results for HALE aircraft and helicopter fuselage will be summarized, and conclusions will be remarked. Lastly, a suggestion for the future works will be noted.

2. Numerical Methods and Validations

2.1 Introduction of the Developed Simulation Code

Ice Shape Estimation and Performance Analysis Code (ISEPAC), a simulation program to analyze icing phenomena occurring on the 3D body, is developed by applying the latest numerical technique. ISEPAC is a second-generation icing analysis tool that is based on the Navier-Stoke equations, Eulerian droplet field calculation, and Messinger model [10] with a shallow water film. ISEPAC can handle not only for the fixed-wing aircraft but also for the helicopter fuselage. The latest actuator disk and surface model loaded on ISEPAC is able to capture the behavior of individual blade tip vortices. By using ISEPAC, the icing characteristics of HALE aircraft and helicopter fuselage are analyzed.

The most important feature of ISEPAC is that ISEPAC can perform the icing simulations both the fixed-wing aircraft and the helicopter fuselage including rotor wake effect without changing the platform. It is the trend that each module is divided as the independent solver in the published codes to simulate various problems as mentioned above (Part 1.3.1). However, divided modules are functionally dependent. It decreases the computation efficiency, and requires manual works.

The additional advantage of ISEPAC is constructed on the OpenFOAM® which is the free, open source CFD software released and developed primarily by OpenCFD Ltd since 2004. The newly developed ISEPAC inherits the merits of open source code. First, the code can be easily added with new modules and fixed the existing modules as same as in-house codes, because the source codes are public.

Second, the latest research results can be immediately reflected. OpenFOAM has a large developer base across most areas of engineering and science, and the developers regularly upload their results to the public domain. Third, ISEPAC is the tightly coupled solver in the single platform. It is efficient because there is less loss in exchanging data for each module. Forth, extensive parallel computing involving the present icing-analysis package could be performed because OpenFOAM itself supports OpenMPI-based parallel computing [47]. Above all, a single platform can be maintained even if certain modules are changed since ISEPAC follows the object-oriented programming.

As shown in Fig. 2.1, ISEPAC consists of four modules: aerodynamic module, droplet module, thermodynamic module, and ice growth model. All of the modules were developed on the same platform. ISEPAC follows the manner of the 2nd generation icing codes. As an aerodynamic solver, 3D Reynolds-Averaged Navier-Stokes equations are applied. Though the icing occurs under the incompressible condition, the energy conservation was applied to consider the heat transfer. The surface roughness is considered in the turbulent model. The droplet field is calculated by using Eulerian approach. It is possible to calculate the collection efficiency even with complicated 3D objects and the massive separation problems. The thermodynamic module is applied for both rime and glaze ice condition. As the runback water is treated by the convection term under thin water film assumption, ISEPAC is able to treat the generic 3D geometries.

Although real icing phenomena are unpredictable by nature, in this study, because of the limited computational resources, quasi-steady flows are assumed. Except for the ice growth model, the previous three modules proceed sequentially under quasi-steady assumption. The total exposure time under icing condition is divide by multiple steps, and each module operates in steady-state assumption under the time interval. In the procedure, the converged results are used as the input value of the following module. For example, droplet trajectories based on the velocity vectors obtained from the converged flow-field solutions are computed. Then, using these results, the thermodynamic analyses are performed. The ice shapes are deliberately determined from the evaluation of the ice mass accreted on the surface.

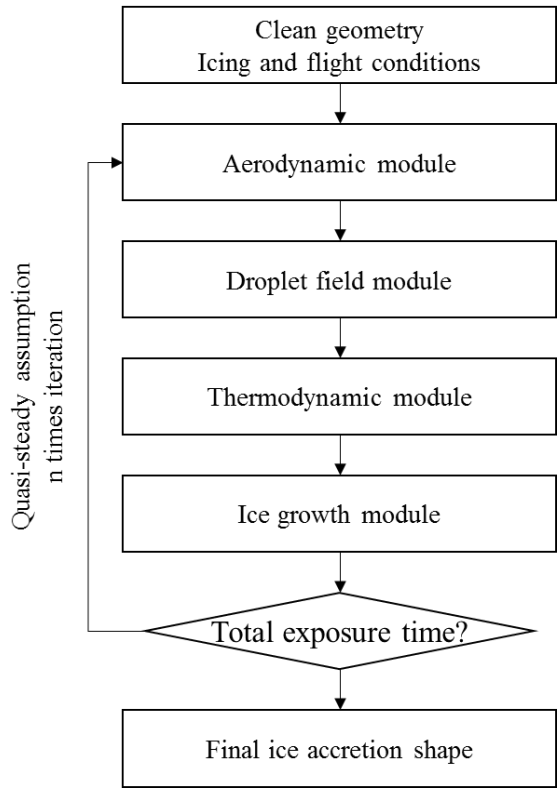

Fig. 2.1 The structure of ISEPAC

2.1.1 Aerodynamic module

In this study, OpenFOAM was employed as the flow solver. The unsteady compressible Navier-Stokes solver, called rhoPimpleFOAM, was employed to take the heat transfer on the surface. The governing equations are following:

$$\frac{\partial \rho_a}{\partial t} + \frac{\partial \left(\rho_a u_{a,i}\right)}{\partial x_i} = 0, \tag{2-1}$$

$$\frac{\partial \rho_a u_{a,i}}{\partial t} + \frac{\partial \left(\rho_a u_{a,j} u_{a,i}\right)}{\partial x_j} = -\frac{\partial p}{\partial x_i} + \frac{\partial}{\partial x_j}\left(\tau_{ji} + T_{ji}\right) + \vec{S}_{act}, \tag{2-2}$$

$$\frac{\partial \rho_a H}{\partial t} + \frac{\partial \left(\rho_a u_{a,j} \mathrm{H}\right)}{\partial x_j} = -\frac{\partial}{\partial x_j}\left(q_j + Q_j\right) + \frac{\partial p}{\partial t}, \tag{2-3}$$

$$\begin{aligned}\frac{\partial \rho_a E}{\partial t} + \frac{\partial \left(\rho_a u_{a,j} \mathrm{E}\right)}{\partial x_j} \\ = -\frac{\partial}{\partial x_j}\left(q_j + Q_j\right) + -\frac{\partial \left(p u_{a,j}\right)}{\partial x_j} \\ + \frac{\partial}{\partial x_j}\left(\tau_{ji} + T_{ji}\right) u_{a,j} + \frac{\partial}{\partial x_j}\left(\alpha_T \left(\frac{\partial e}{\partial x_j}\right)\right) \quad .\end{aligned} \tag{2-4}$$

Here ρ_a is density, p pressure, u_a is the velocity vector, H is the total enthalpy, and E is the total internal energy. These last two quantities are related to the specific enthalpy h and internal energy e through $H = \mathrm{h} + 0.5 u_a u_a$ and $E = \mathrm{e} + 0.5 u_a u_a$, and are related through each other by $E = \mathrm{H} - \mathrm{p}/\rho$. In turbulent simulations, the above equations and all flow fields are interpreted as being Favre-averaged, according to either Reynolds-Averaged Navier-Stokes (RANS). Molecular transport is represented by the Newtonian stress tensor τ_{ji} and the Fourier heat conduction q_j, with the viscosity and the thermal conductivity being either constant or temperature dependent according to Sutherland's formula:

$$\mu = \mu_0 \left(\frac{T}{T_0}\right)^{1.5} \frac{T_0 + 110.4}{T + 110.4} \quad . \tag{2-5}$$

μ_0 and T_0 are reference values depending on the gas. The thermal conductivity is obtained with $k = c_p\mu/Pr$ for a given value of the Prandtl number Pr, with $c_p$being the specific heat capacity. The turbulent transport is modeled with RANS through the Reynolds stress tensor T_{ij} and the turbulent heat flux Q_j . In laminar flow $T_{ij} = Q_j = 0$.

The origin rhoPimpleFoam is based on Eq. (2-3). Hence, Eq. (2-3) and (2-4) not only differ on their underlying solution algorithms, explained next, but also use different governing equations. In particular, notice that Eq. 3 neglects the viscous dissipation term of the energy equation, i.e., the last term on the right-hand side of Eq. (2-4). This can lead to significant errors in the direct numerical simulation of turbulent flows. When the ice accumulated, flow tends to transit rapidly from laminar to turbulent flow. To achieve an accurate solution for viscous dissipation under turbulent flow, this numerical code modifies the energy equation from Eq. (2-3) to Eq. (2-4)

OpenFOAM solvers use the finite volume method to solve the integral form of conservation equations such as Eqs. (2-1) - (2-4). For this purpose, these solvers consider a collocated cell-centered variable arrangement, a feature that allows them to handle complex unstructured meshes. Fluxes through the cell faces can be reconstructed from variables adjacent to them using a different type of reconstruction methods. These methods include total variation limited (TVD) schemes and central schemes. The references for the numerical methods used by OpenFOAM are Ferziger and Peric [48], and Jasak [49].

rhoPimpleFoam is a transient, implicit, pressure-based solver. As indicated in Fig. 2.2, rhoPimpleFoam uses an inner iterative loop to correct the velocity field using the output of a pressure equation, as in the well-known PISO algorithm [50], [51]. It also uses an outer iteration loop for additional corrections. A detailed discussion of the implementation of the PISO algorithm in OpenFOAM is given in Jasak [49]. Various temporal and spatial discretization options are available for rhoPimpleFoam. In the following, unless said otherwise, gradients and Laplacians are discretized with central schemes, and convective fluxes are discretized using a second order, upwind-biased, and unbounded 'linearUpwind' scheme is applied. Time is discretized with local time stepping called 'CoEuler' scheme that uses under quasi-steady assumption for fixed-wing aircraft. For ADM and ASM, Time discretized with a first-order backward-differencing scheme.

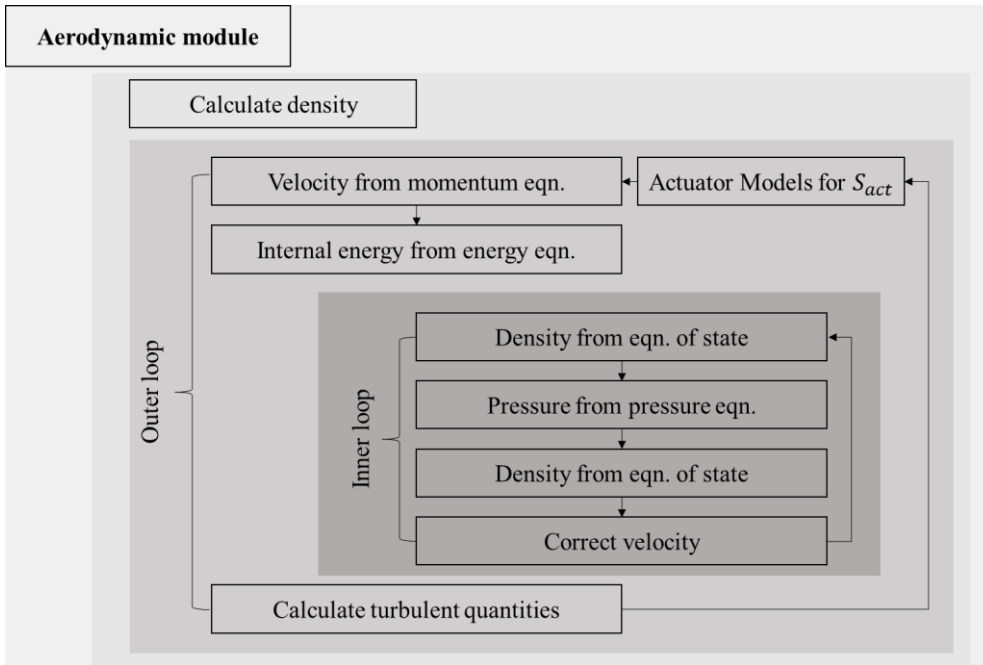

Fig. 2.2 Structure of the aerodynamic module

A. Actuator Disk and Surface Model

For fixed-wing aircraft such as HALE aircraft application, the source term, S_{act}, is excluded in the Eq. (2-2). However, to accurately predict the ice accretion shapes on the helicopter fuselage, the rotor wake effects should be considered. To treat the rotor wake effects to the flow-fields, the additional model is added in the aerodynamic module. In this study, ADM and ASM are applied to consider the rotor wake effects.

The ADM and ASM used in this study were the latest methods developed by Kim [45]. The ADM and ASM are considered by inserting the pressure difference across the rotor disk into the momentum-conservation equation as the source term. The pressure difference was calculated from the lift and drag of the corresponding

locations using BET. However, ADM and ASM developed by Kim [45] do not consider the heat transfer. The origin ADM and ASM deal with the compressible effect while the codes invoke aerodynamic force data from the C81 tables. This study extends the origin ADM and ASM as compressible solver by adding the mass and energy conservation, and equation of state as shown in Eq. (2-1) and (2-4).

To consider the effects of the rotor blades or disk(s), the source term is added to the momentum equation. The source term represents the local thrust as shown in Eq. (2-6).

$$\vec{S}_{act} = \frac{d\vec{T}}{dV} \tag{2-6}$$

The thrust obtained from the BET is transformed into terms of force per unit volume. To estimate the local thrust on an unstructured mesh, the local induced angle of attack α_i was calculated to determine the aerodynamic coefficients c_l, c_d, and c_m, at each element as written in Eq. (2-7). The aerodynamic coefficients were obtained from the aerodynamic performance lookup tables to determine the coefficients for the given local effective angle of attack.

$$dT = d\psi(dLcos\alpha_i + dDsin\alpha_i) = \frac{dA}{2}\rho V^2(c_l cos\alpha_i + c_d sin\alpha_i) \tag{2-7}$$

The local thrust dT at each cell on the blade region for ASM was calculated through a combination of the local lift (dL) and drag (dD), which is calculated by each cell area and the aerodynamic coefficients. Therefore, the activated region of the source term varies with time. For ADM, the time averaged thrust (dT) is exerted to the disk region.

In this study, a novel ASM suggested by Kim et al. [45] has been applied. As shown in Eq. (2-7), actuator methods require the local induced angle of attack. The previous ASMs have ambiguity to set the location of reference points or lines to calculate the induced velocity. There is no theoretical ground to set the reference points or lines.

It should be noted that the velocity components obtained from CFD calculations include not only the induced velocities due to the trailed and shed vortices but also the velocity components induced by the bound circulation on the rotor blades. When the reference line is too far away from the blade, it tends to yield relatively low induced velocities. On the other hand, when it is too close, it is difficult to separate the induced velocities due to the tip vortex from that of the bound circulation on the blade. Therefore, the results of the previous ASMs were dependent on the problems and experience.

However, the new actuator surface model based on the lifting line theory has been suggested to distinguish velocity components from the trailed and shed vortices and the bound circulation on the rotor blades. The first component comes from the lifting blade, and the second component is related to the vortexes. The latter is the pure

induced velocity. However, the velocity calculated by CFD includes both components at the reference line, which is depicted in Fig. 2.3.

To calculate the velocity component from lifting blade, the new ASM allocates the divided sectional bound circulations along the blade location as shown in Fig. 2.3. From the sectional lift forces, which calculated from BET, the strength of the divided sectional bound circulations (Γ_s) can be calculated. Since the velocity induced by the distributed circulations along the blade describes lifting blade effect, the pure induced velocity can be obtained by deleting the calculated velocity from the CFD results. The detailed methodology for the ASM is attached in Appendix 6, and the validation results are presented in Ref. [45].

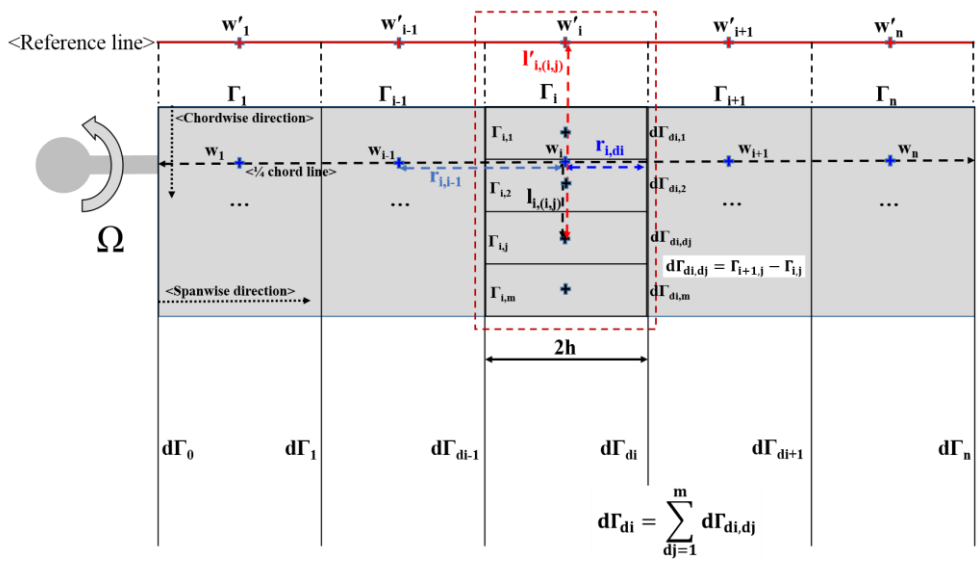

Fig. 2.3 The sectional circulation according to the blade location [45]

There was an attempt to predict the ice accretion shapes on the helicopter fuselage including rotor wake effects [43]. The previous study systematically analyze the ice accretion shapes on the fuselage by considering wake-body interaction using the inflow model. However, the inflow model is correlated by the thrust without the fuselage. It has limitations for the case of strong interaction between the rotor wake and fuselage. Therefore, they extracted and evaluated the ice shapes under high forward flight speed which can ignore the wake-fuselage interaction. On the other hand, the applied ADM and ASM yield the inflow form the Navier-Stoke equations. It does not requires the specific inflow model. Therefore, the accurate inflow can be calculated with strong wake-body interaction. In this study, the effects of various forward flight speed can be evaluated including hovering, low- and high flight speed.

B. Turbulent Model

Once the ice is accreted on the solid surface, it changes not only the outer boundary of the surface but also the surface roughness, which again affects the turbulence of the flow. Most of the turbulence models used in the numerical calculation were derived based on the smooth surface. Hence, they have a general tendency to underestimate the convective heat-transfer coefficients, leading to the inaccurate prediction of ice length and direction. Moreover, the surface-friction coefficients also increase because of the enhanced turbulence induced by the surface roughness. Accordingly, it is essential to employ a turbulence model that includes

the surface roughness to obtain an accurate prediction of the ice shape and the resulting increase in drag.

Under the icing conditions, the surface roughness is dependent on the ambient temperature, liquid-water content (LWC), medium volumetric diameter (MVD), and flight speed. Fouldai, H. et al. [43] applied a constant surface roughness of 0.5 mm irrespective of the icing conditions. In this study, the more advanced surface-roughness model developed by NASA LEWICE was applied [12], where the surface roughness is given as a function of the temperature, velocity, LWC, and MVD.

Normally, the surface roughness is considered by modifying the boundary condition of existing turbulence models, such as k-ω, k-ε, and the Spalart-Allmaras model. In the present study, Spalart-Allmaras turbulence was chosen as the baseline, and the original model was modified to include the surface-roughness effects, as in Ref. [52].

To account for roughness, the distance function d_{new} is replaced by the standard version of Spalart-Allmaras. The modified version is given by the following equation:

$$\frac{\partial \rho_a \hat{v}}{\partial t} + u_{a,j}\frac{\partial(\rho_a \hat{v})}{\partial x_j} = c_{b1}\hat{S}\rho_a \hat{v} - c_{w1} f_w \rho_a \left(\frac{\hat{v}}{d_{new}}\right)^2 + \frac{1}{\sigma}\frac{\partial}{\partial x_j}\left(\mu \frac{\partial \hat{v}}{\partial x_j}\right) + \frac{1}{\sigma}\frac{\partial}{\partial x_j}\left(\sqrt{\rho_a}\hat{v}\frac{\partial \sqrt{\rho_a}\hat{v}}{\partial x_j}\right) + \frac{c_{b2}}{\sigma}\frac{\partial \sqrt{\rho_a}\hat{v}}{\partial x_i}\frac{\partial \sqrt{\rho_a}\hat{v}}{\partial x_i}, \tag{2-8}$$

To account for roughness, the distance function, which represents the distance from each field point to the nearest wall, is augmented to read

$$d_{new} = d + 0.03k_s, \tag{2-9}$$

where d is the (original) distance to the nearest wall and k_s is the conventional Nikuradse sand roughness scale height. The function χ is also modified to be:

$$\chi = \frac{\hat{\nu}}{\nu} + 0.5\frac{k_s}{d_{new}} \tag{2-10}$$

The wall boundary condition for the smooth wall is set to $\hat{\nu}_{wall} = 0$. However, due to the surface roughness, the value of $\hat{\nu}_{wall}$ is defined by the following the Nikuradse's experiments.

$$\left(\frac{\partial \hat{\nu}}{\partial n}\right)_{wall} = \frac{\hat{\nu}_{wall}}{0.03k_s}\ , \tag{2-11}$$

where n is along the wall normal.

Form the energy equation, the gradient of the temperature at the wall $\partial T/\partial n$ is calculated, and then the convective heat transfer can be determined by the definition of heat convection coefficient in Eq. (2-12).

$$h_c = \frac{-(k_l + k_t)\partial T/\partial n}{T_s - T_\infty} \tag{2-12}$$

To consider the wall roughness effect to the heat transfer, thermal conductivity of turbulent flow (k_t) is applied as shown in Eq. (2-13).

$$k_t = \frac{\mu_t c_p}{Pr_t} \tag{2-13}$$

2.1.2 Droplet-Trajectory Module

The droplet-trajectory analysis was performed to estimate the mass of the droplets that are collected on the surface. The droplet-trajectory calculation methods were classified as the Lagrangian method and the Eulerian method. In the Lagrangian approach, a set of droplets was released in front of the surface, and the trajectory of each droplet was monitored to determine the collection efficiency. On the other hand, for the Eulerian approach, the controlled-volume concept was employed, and the same grid system was used to calculate the droplet fields. In this study, the Eulerian approach was adopted because of its superiority when considering the icing phenomenon under massive separation.

Since the air volume in the arbitrary space is much greater than that of the droplets, the droplet field was calculated separately from the airfields. The droplet fields were calculated based on the converged velocity vectors in the flow-field analysis module,

and for the computation, the mass- and momentum-conservation equations were used, as shown in Eq. (2-14), and Eq. (2-15), respectively [53].

$$\frac{\partial \bar{\rho}_d}{\partial t} + \frac{\partial \left(\bar{\rho}_d \vec{u}_{d,i}\right)}{\partial x_i} = 0 \tag{2-14}$$

$$\frac{\partial \bar{\rho}_d u_{a,i}}{\partial t} + \frac{\partial \left(\bar{\rho}_d u_{d,j} u_{d,i}\right)}{\partial x_j} = \frac{3}{4}\frac{\bar{\rho}_d \mu_a C_D Re_d}{\rho_w MVD^2}\left(\vec{u}_{a,i} - \vec{u}_{d,i}\right) + \bar{\rho}_d \vec{g}_i \left(1 - \frac{\rho_a}{\rho_w}\right) \tag{2-15}$$

The external forces acting on the single droplet is illustrated in Fig. 2.4. The drag, gravity, and buoyancy that act on the droplets were substituted into the momentum-conservation equation as source terms. The drag on the droplet was used, as in Eq. (2-16).

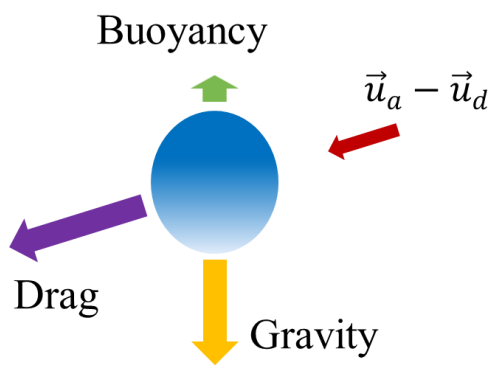

Fig. 2.4 The external forces acting on a droplet

$$C_D = 24/Re_d\left(1 + 0.197{Re_d}^{0.63} + 2.6 \times 10^{-4}{Re_d}^{1.38}\right) \quad (2\text{-}16)$$

The boundary conditions were imposed based on the relation between the droplet velocity vector and the surface normal vector, which is written as [54]:

$$\vec{u}_d \cdot \vec{n} > 0, \qquad \vec{u}_d = \vec{u}_d, \qquad \bar{\rho}_d = \bar{\rho}_d \quad (2\text{-}17)$$

$$\vec{u}_d \cdot \vec{n} < 0, \qquad \vec{u}_d = 0, \qquad \bar{\rho}_d = 0 \quad (2\text{-}18)$$

The collection efficiency is determined based on the computed velocity vector and bulk density.

$$\beta = \frac{\bar{\rho}_d \vec{u}_d \cdot \vec{n}}{LWC_\infty \cdot U_\infty} \quad (2\text{-}19)$$

From the calculated collection efficiency, total impinging mass is determined by the following relation.

$$\dot{m}_{com} = \beta \cdot LWC_\infty \cdot U_\infty \quad (2\text{-}20)$$

2.1.3 Thermodynamic Analysis Module

The role of the thermodynamic analysis module is to estimate the fraction of the mass that freezes on the surface. When a droplet hits the surface, a water film is formed on it. Then, the water film starts to run along the flow because of the shear force. The resulting runback water freezes into ice through convective heat transfer. To model this phenomenon, a thermodynamic model similar to that in FENSAP-ICE was employed, where the ice mass, the thickness of the water film, and the surface temperature based on the water-film model were obtained, as well as the mass- and energy-conservation equations [54].

The velocity of the water film was represented as a function of the water-film thickness. Only the shear forces were assumed to act on the water film; it was also assumed that the water flows in the direction of the shear force. Because the water film is extremely thin, it is possible to assume a linear velocity distribution within the water film as shown in Fig. 2.5. Then, the velocity can be written as a function of the shear force and water-film thickness, as in Eq. (2-21). The shear force is already known from the flow solver, and the other unknowns, such as the water-film thickness, ice mass, and surface temperature, can be determined based on the mass- and energy-conservation equation.

$$\overline{U}_f = f(\mathrm{h}_f) = \frac{1}{h_f}\int_0^{h_f} u_f dh = \frac{h_f}{2\mu_w}\vec{\tau}_{wall} \tag{2-21}$$

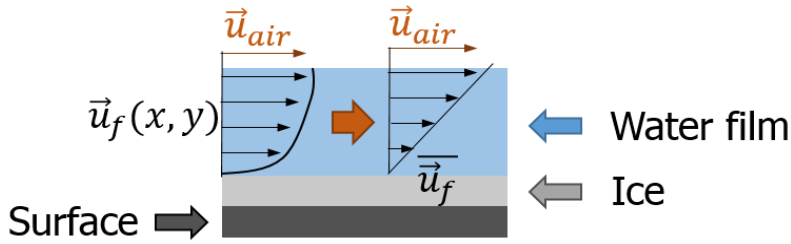

Fig. 2.5 Thin water film model

The convection terms in the mass- and energy conservation equations are related to the fraction of water that does not freeze, and which flows. The net flux of the water film in the control volume was calculated in the same manner as the flow solver, and the convection terms were calculated using the 1st-order upwind scheme, which is based on the velocity vector of the calculated water-film.

Each of the terms and directions of energy covered in the thermodynamic model are illustrated in Fig. 2.6. The first term on the right side of Eq. (2-22) represents the water mass that hits the surface, while the 2nd term shows the ice mass that freezes on the surface. The first term on the right-hand side of Eq. (2-23) is the kinetic energy of the water droplet, while the second and third terms represent the latent heat and heat convection, respectively.

The impinging mass and kinetic energy of the water droplet are the input value for the thermodynamic module because those were calculated form the droplet-trajectory module.

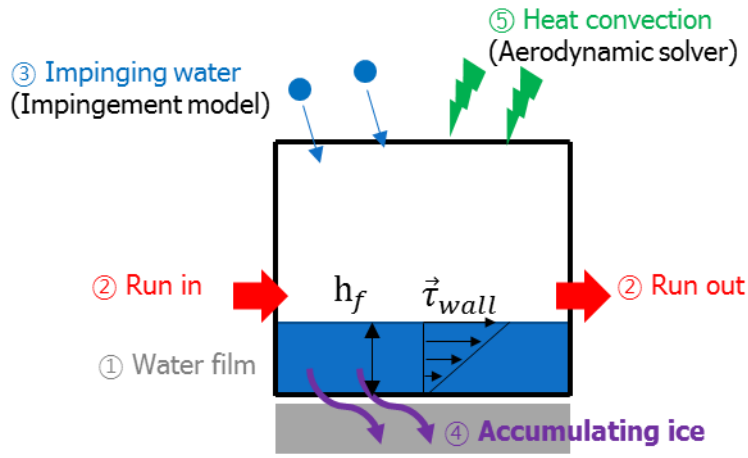

Fig. 2.6 Terms and direction of energy in thermodynamic model

$$\rho_w \int \frac{\partial h_f}{\partial t} dV + \int \nabla \cdot (\rho_h \vec{U}_f) dV = \dot{m}_{com} - \dot{m}_{ice} \tag{2-22}$$

$$\rho_w \left[\int \frac{\partial h_f c_{p,w} \tilde{T}_{eq}}{\partial t} dV + \int \nabla \cdot (h_f c_{p,w} \tilde{T}_{eq} \bar{U}_f) dV \right] = \dot{E}_{com} + \dot{E}_{ice} + \dot{E}_{conv} \tag{2-23}$$

Here, the source terms of the energy conservation can be written as :

$$\dot{E}_{com} = \dot{m}_{com} \left[c_{p,w} \tilde{T}_{d,\infty} + \frac{1}{2} |\vec{U}_d|^2 \right] \tag{2-24}$$

$$\dot{E}_{ice} = \dot{m}_{ice} \left[L_{fus} - c_{p,i} \tilde{T}_{eq} \right] \tag{2-25}$$

$$\dot{E}_{conv} = h_c A\left(T_{eq} - T_{\infty}\right) \tag{2-26}$$

The heat convection coefficient (h_c) in Eq. (2-26) is calculated in the aerodynamic module as referred in Eq. (2-12). When the equilibrium temperature (T_{eq}) is updated in the thermodynamic module, the heat convection coefficient should be changed by following the definition. Since ISEPAC is developed in a single platform, the updated heat convection coefficient can be immediately delivered to the thermodynamic module. However, the aerodynamic model and thermodynamic module are separated in FENSAP-ICE. The entire value of the heat convection ($\dot{E}_{conv}$) is delivered from the aerodynamic model to the thermodynamic module. Therefore, there is a disadvantage that the calculated equilibrium temperature cannot be considered. It slows down the convergence of the solver.

There are three unknowns in the previous equations, namely the ice mass, water-film thickness, and surface temperature. This number is less than the number of equations, and the unknowns, therefore, cannot be uniquely determined. To determine the unknowns, an additional relation proposed by Messinger was used [10]. First, the state of the surface from the Messinger model was assumed, and then the mass- and energy-conservation equations were solved. Finally, the physically valid state of the surface was determined, as in Fig. 2.7. More specific description is attached in Appendix 6.1.

(1) Water only

Under this condition, pure water exists on the surface. Therefore, the ice mass is set to zero. Using these conditions, the water-film thickness was calculated from the mass-conservation equation, and the surface temperature was obtained from the energy-conservation equation. If the resulting water-film thickness is greater than zero, and the surface temperature is above 0°C, the “water only” assumption is regarded as valid. Otherwise, the “water and ice” surface condition is assumed as a next step.

(2) Water and Ice

Under this condition, water is assumed to coexist with ice. The surface temperature is set to 0°C, and the water-film thickness is calculated using the mass-conservation equation. Then, the ice mass from the energy-conservation equation was determined. If both the water-film thickness and ice mass are greater than zero, the current assumption is valid. Otherwise, the state of the surface is determined as “ice only.”

(3) Ice only

Here, only ice exists on the surface. Hence, the water-film thickness was set to be zero. The ice mass and surface temperature were determined using the conservation equations. If the ice mass is greater than zero and the surface temperature is below 0°C, the current “ice only” assumptions become valid. Otherwise, the “water and ice” surface condition is assumed, and the iteration continues until the criterion is met, as shown in Fig. 2.7.

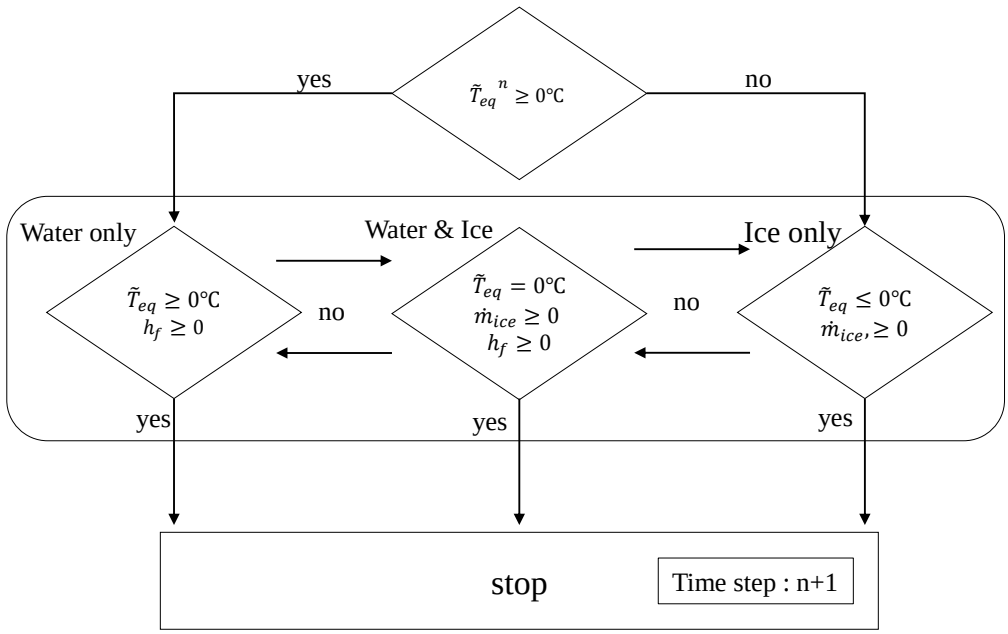

Fig. 2.7 Flow chart of the thermodynamic model.

2.1.4 Surface Grid Regeneration Module

Based on the ice mass obtained in the thermodynamic module, the ice thickness was determined, and the surface grid forward was shifted. The ice thickness was calculated using Eq. (2-27). The ice density was set at 920 kg/m³.

$$h_t = \frac{\dot{m}_{ice}\Delta t}{\rho_{ice} A_{sur}} \tag{2-27}$$

As shown in Fig. 2.8, a newly formed surface was generated due to ice accretion by interpolating the ice thickness and normal vector at each surface to the node points. The ice thickness and the surface normal vector at the center of each surface were

calculated. The calculated ice thickness and the surface normal vector are then linearly interpolated to adjacent node points, and the newly formed surface is generated by the interpolated node values.

Then, the volume grid system was generated using the surface that is newly formed due to the ice accretion. Depending on the computational resources available, the grid generations were repeated three or four times to obtain ice shapes for the time that it was exposed to icing conditions.

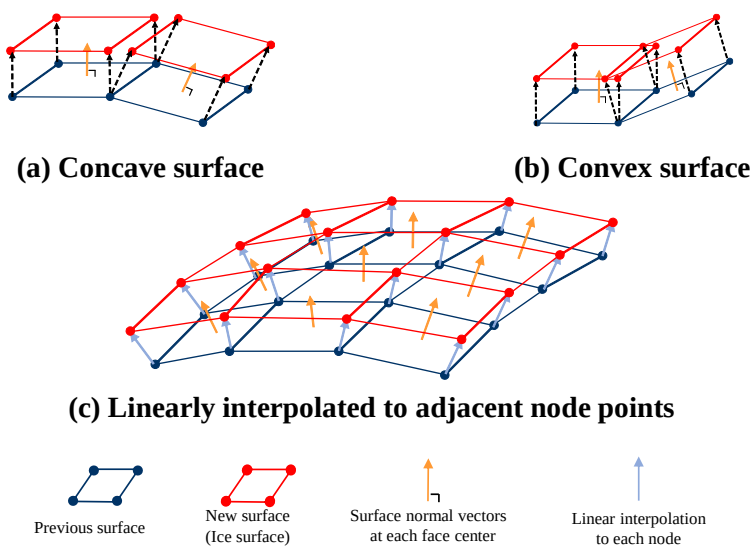

Fig. 2.8 Surface re-meshing method

2.2 Validations of Numerical Methods

2.2.1 Aerodynamic Module

A. 2D Airfoil

The flow solver for a fixed-wing aircraft was verified by comparing the computed aerodynamic performance under rime and glaze ice conditions with the experiment results. Broeren et al. [55] conducted a dry wind-tunnel test to obtain the aerodynamic performance of an airfoil with ice accreted on the surface. The comparison with Broeren's data is depicted in Fig. 2.9, where the freestream Mach number is 0.2, and the Reynolds number based on the chord length is 1.69×10^7.

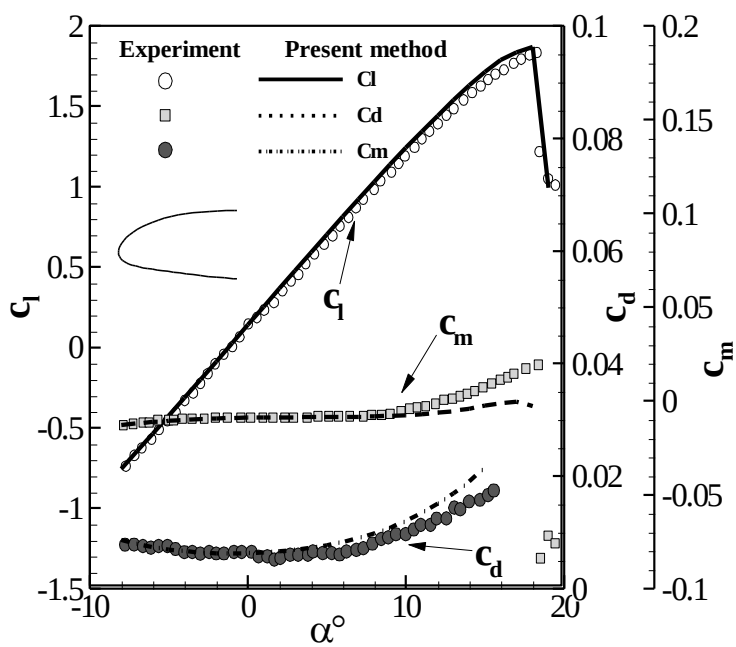

(a) Clean airfoil

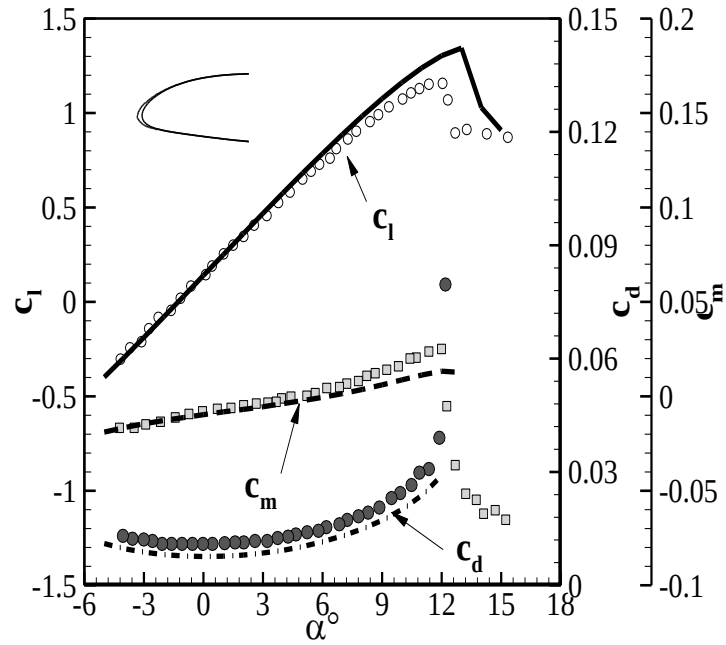

(b) Rime ice shape

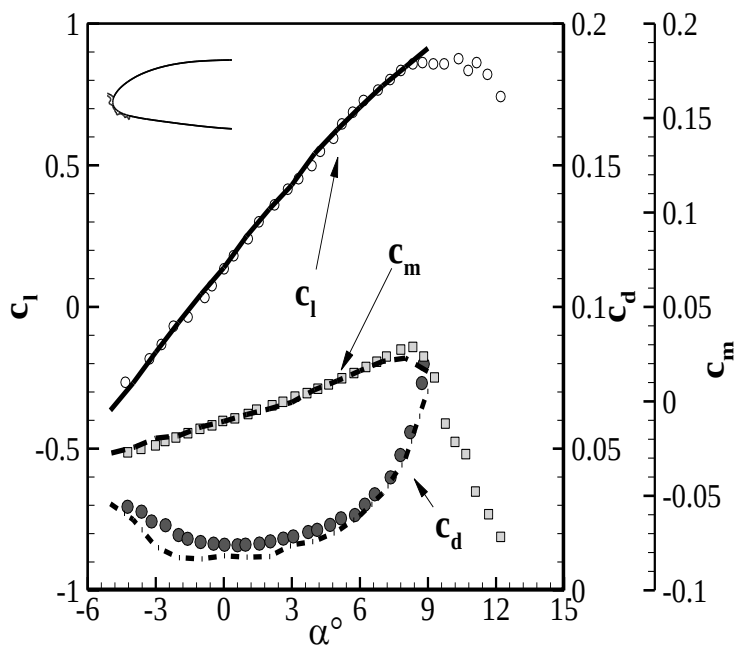

(c) Glaze ice shape

Fig. 2.9 Lift, drag, and moment coefficients of the clean airfoil, rime and glaze ice shapes [55].

B. 3D HALE aircraft

To validate the accuracy of the 3D aerodynamic analysis code, the aerodynamic performance of the baseline HALE aircraft used for this study is computed, and the computed results are validated against those from KARI [37], [56]. Because of the long wingspan, the experiment could not be conducted in KARI's wind tunnel. Instead, KARI designed and operated the HALE aircraft using ANSYS FLUENT. Although the aerodynamic data were obtained through numerical analysis, KARI was nonetheless able to successfully operate the HALE aircraft. Therefore, KARI's numerical results for the baseline HALE aircraft are compared with those of the 3D aerodynamic solver.

The grid system and boundary conditions for the numerical calculation are summarized in Fig. 2.10. A total of 260,000 surface grid cells and 7,000,000 space grid cells are used to construct a computational domain. For the first grid height, the y^+ value is set to 30, and 15 prism layers are implemented with a growth ratio of 1.2 to consider the wall function. The icing analysis and the aerodynamic performance calculation are performed in the same grid system.

Unlike in this research, KARI employs ANSYS FLUENT. The numerical analysis is performed for $Re = 2.78 \times 10^5$, and $M_\infty = 0.022$. The lift and drag coefficients are obtained for the angle of attack of 0, 2.5, 4, and 8°. The computed results are compared in Fig. 2.11, where both the lift and drag coefficients can be seen to agree well with each other. In comparison with KARI, the drag calculated by the proposed 3D aerodynamic solver seems to be slightly overestimated, possibly

due to the fact that the first grid height of the present calculation is set fairly high compared to KARI in order to consider a wall function. In contrast, KARI keeps the y^+ value under 1.0 over the entire surface. However, as long as the angle of attack remains less than 3˚, the difference in the drag coefficient appears to be negligible.

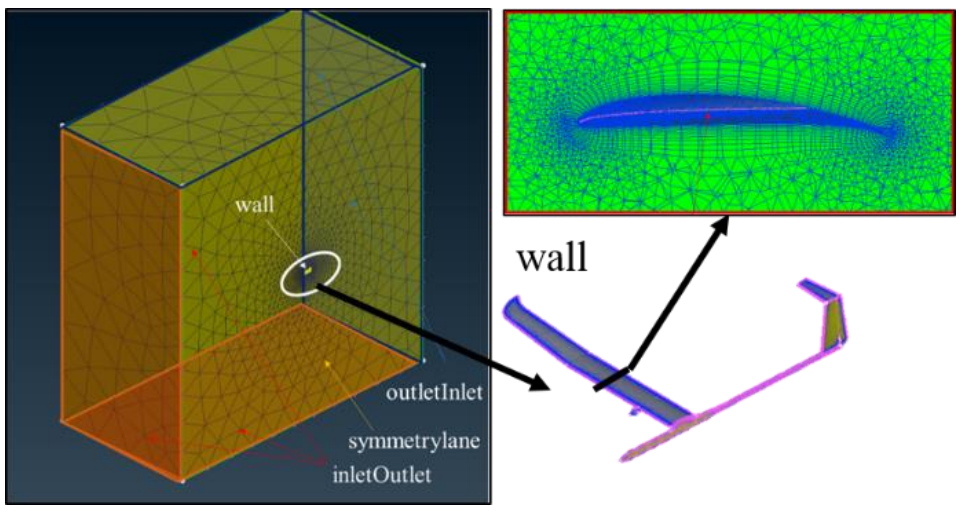

Fig. 2.10 Boundary conditions and the grid system

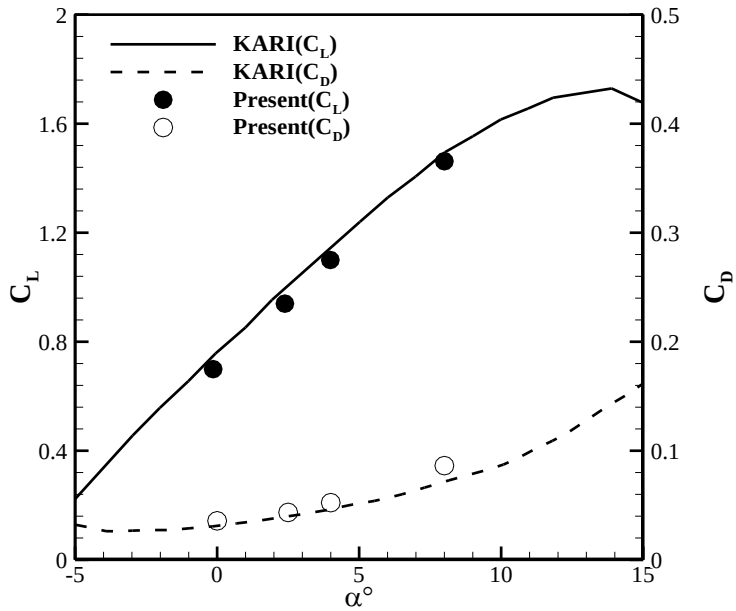

Fig. 2.11 Validation results for lift and drag coefficients ($Re = 2.78 \times 10^5$, and $M_\infty = 0.022$)

C. Rotorcraft – Actuator Models

Using the experiments performed by Elliot et al. for the forward flight of a helicopter [57], the present actuator disk and actuator surface methods were evaluated individually. The rotor has four rectangular blades, and the fuselage has the rotor body interaction (ROBIN) geometry. In their experiment, Elliot et al. measured a series of inflows on the rotor disk with respect to the advance ratios, and they carefully observed the aerodynamic interaction between the rotor and fuselage. In the present study, numerical computations were performed for an advance ratio of 0.15 and a thrust coefficient of 0.0064 for the rotor system with four rectangular planform blades. The blades have a NACA 0012 airfoil, an aspect ratio of 13, and a

negative 13 degree linear twist. The rotor has a root cut at 0.24R and 3° forward-tilt shaft angle.

To construct the entire computational domain, around 14 million grid points were used, and the same grid system was applied to both ADM and ASM models. The computational grid system is depicted in Fig. 2.12. The computed results are shown and compared with the results obtained experimentally and with other computations [57]-[59].

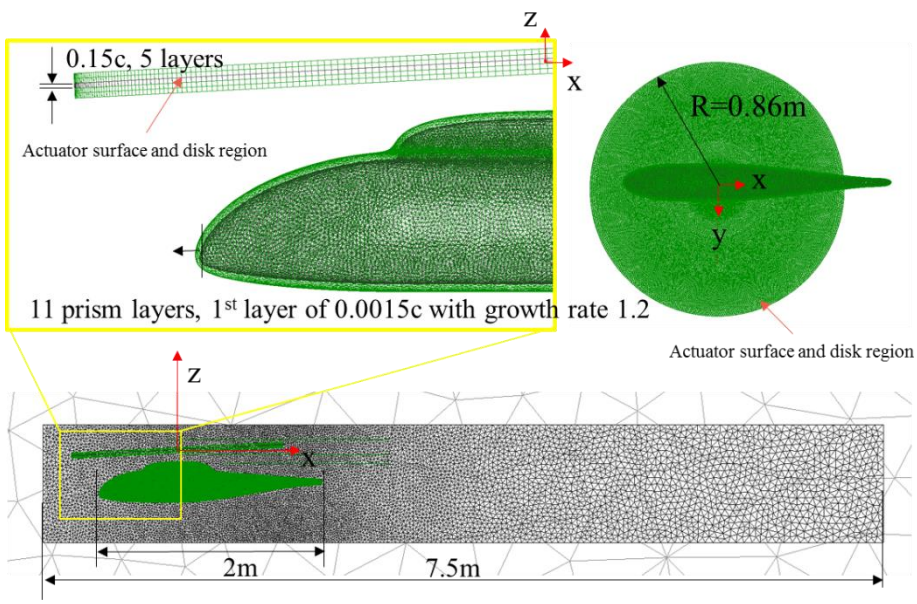

Fig. 2.12 Grid used for computing rotor and fuselage.

The longitudinal and lateral time-averaged inflow distributions at $\mu = 0.15$ are compared in Fig. 2.13. The inflows were measured one chord above the rotor disk and were non-dimensionalized by the rotor tip speed. Irrespective of the measured

directions, the computed inflows obtained from ASM were shown to be in excellent agreement with experimental and other computation results. In particular, the ASM solver yields a good prediction of the inflow distribution along the longitudinal direction. A small discrepancy was observed for the inflows at azimuth angles of 90°, 240°, and 300° compared to the full computational fluid dynamics (CFD) results [59]. This is because ASM can handle the generation of tip vortices and the resulting induced velocities with sufficient accuracy.

On the other hand, the results provided by ADM are not consistent with the experiments. ADM underestimates the inflow distribution along the longitudinal direction, which is inconsistent with the experiment and ASM results. As shown in Fig. 2.13 (b), ADM has some difficulty with predicting the lateral inflow for a forward-flight helicopter. Although ADM can predict the asymmetric distribution of the inflow ratios at the advancing and retreating sides, there is a slight discrepancy of the inflow in the regions of the retreating side. In particular, for ADM, it is difficult to predict the exact inflow at azimuth angles between 240° and 300°, where the effect of the trailing vortex is dominant.

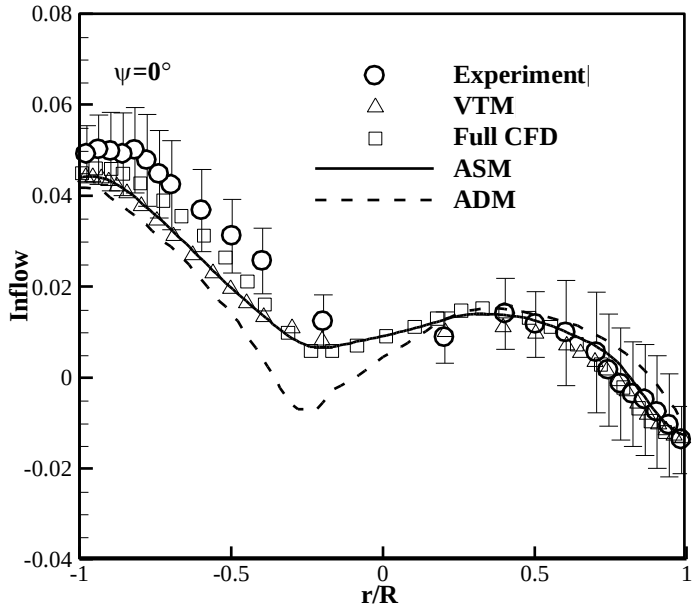

(a) Comparison of longitudinal inflow for forward-flight helicopter

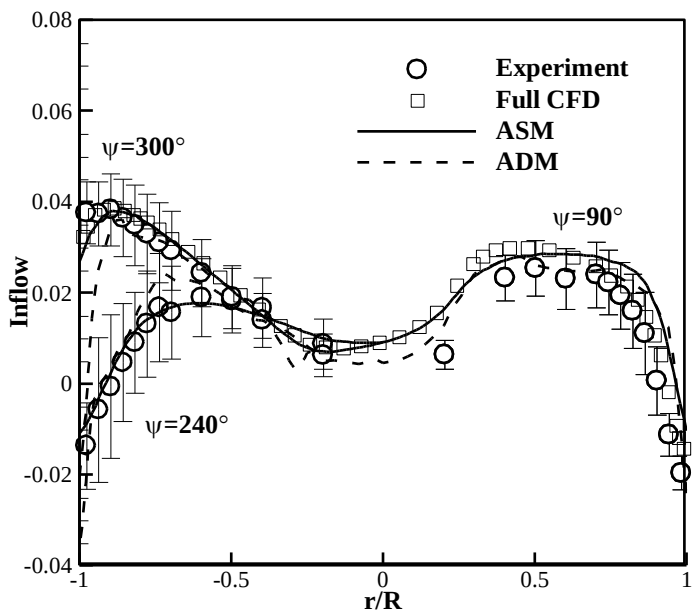

(b) Comparison of lateral inflow for forward-flight helicopter

Fig. 2.13 Comparison of longitudinal and lateral inflow for helicopter in forward flight, $\mu = 0.15$, $C_T = 0.0064$, $\alpha_s = -3^\circ$

Fig. 2.14 shows the time-averaged pressure distribution on the fuselage surface at $\mu = 0.15$ for one rotor revolution. The pressure distribution that was applied to the fuselage surface was compared to the experiment and simulation results of the isolated fuselage, ASM, and ADM. The pressure distribution of the experiment and that of the isolated fuselage on the surface made a big difference because the pressure distribution on the fuselage surface was obtained by including the rotor effects in the experiment. On the other hand, the numerical results obtained considering the rotor effects showed that the results are well matching to the experimental results, regardless of the rotor analysis methods. The pressure distribution on the fuselage's surface depends on the longitudinal inflow distribution. Compared to the experiment and ASM, ADM generally underestimated the longitudinal inflow at the hub towards 0° as shown in Fig. 2.13 (a). However, the pressure distribution on the fuselage surface had a very small difference when different methods were used to interpret the rotor results. Both ADM and ASM also predict the separation caused by the shape of ROBIN because while predicting the inflow, they can precisely simulate the flow phenomenon on the fuselage, where the CFD is performed.

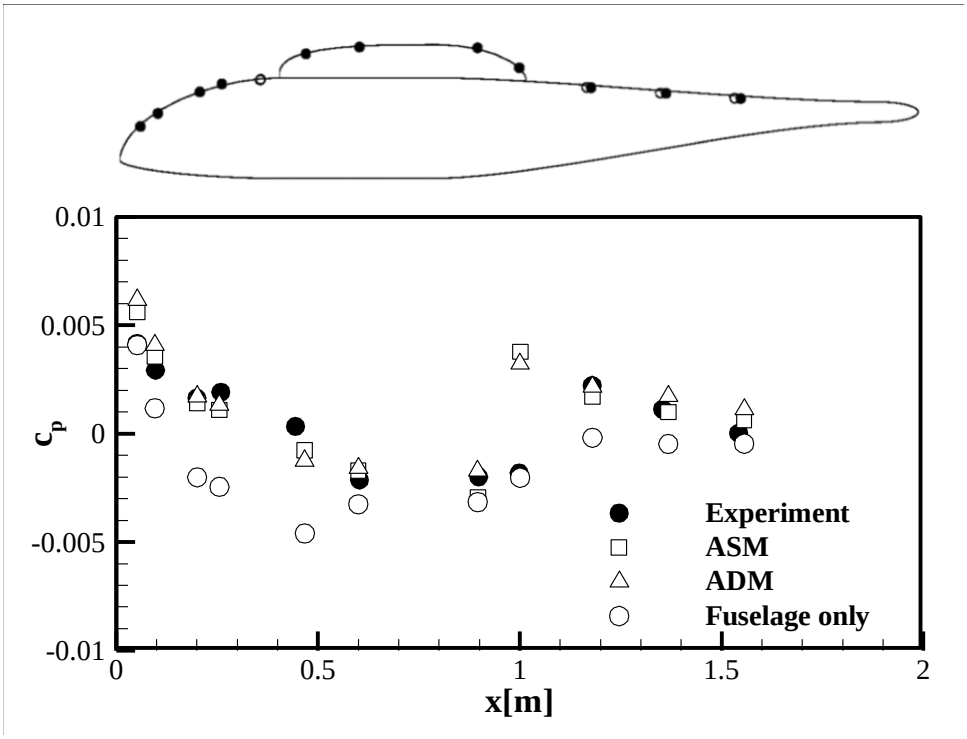

Fig. 2.14 Averaged C_p distribution on the fuselage surface for 1 rotor rev., $\mu = 0.15$, $C_T = 0.0064$

D. Surface Roughness Model

To confirm whether the surface roughness model is correctly included, the surface friction coefficients along the flat plate were compared with those obtained in the available experiment. The Reynolds number based on the distance from the beginning of the flat plate ranges from zero to 5×10^6. The computed results were obtained for a non-dimensional surface roughness of 0.00025 and 0.001, and the results were compared with Hang & Mills's empirical relation [60] in Fig. 2.15. As can be seen in the Fig. 2.15, the effectiveness of the surface roughness was accurately considered even for the relatively high surface roughness value.

Because of a lack of available experiment, the convective heat-transfer coefficients were verified against those of the other numerical codes, such as LEWICE and FENSAP-ICE, in Fig. 2.16. The computation of the NACA 0012 airfoil with a chord length of 0.5334 m and constant surface roughness of 0.55 mm was performed.

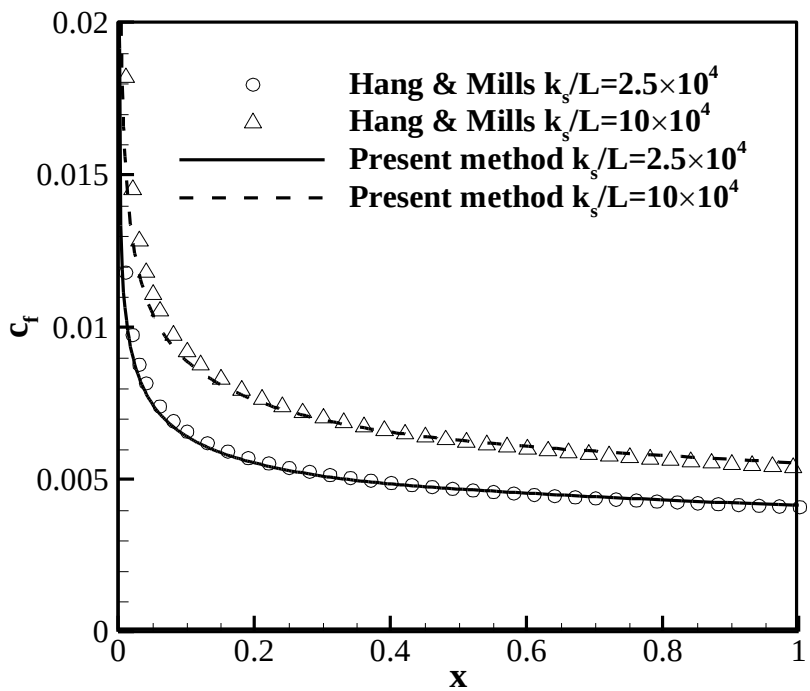

Fig. 2.15 Skin-friction coefficient of flat plate

As indicated, the present results are similar to those obtained by FENSAP-ICE [24]. Unlike the present solver and FENSAP-ICE, LEWICE was developed based on the boundary-layer model to include viscous effects as well as transition model. Once ice begins to accrete on the surface, the enhanced surface roughness accelerates

the transition. Therefore, in the present study, the transition model was not considered separately. It should be noted that there exists a significant deviation at the trailing edge. Because the boundary-layer theory is unable to predict separation, LEWICE tends to overestimate the heat-convection coefficients at the trailing edge.

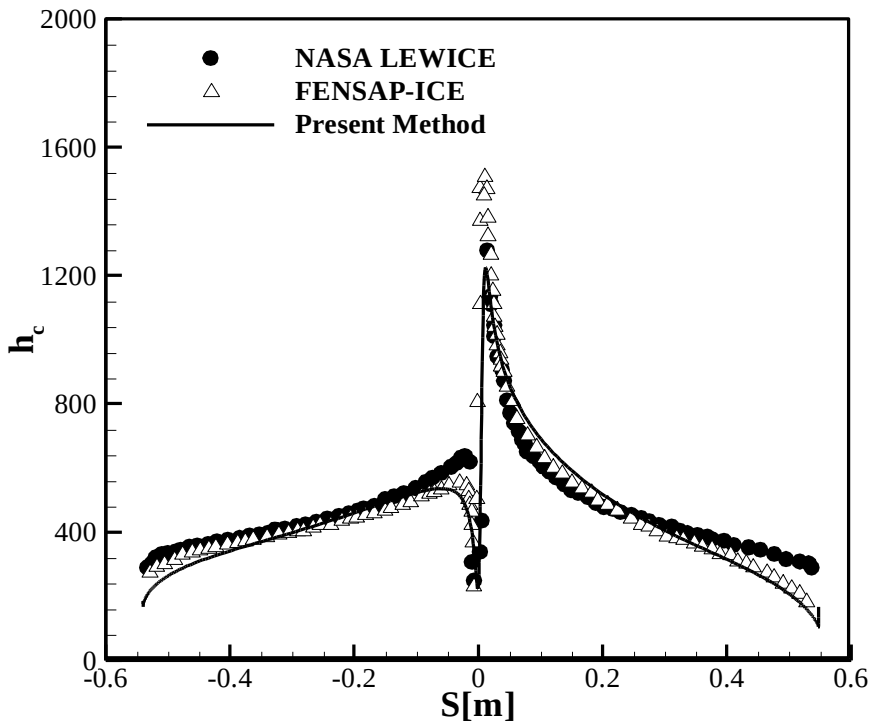

Fig. 2.16 Heat-convection coefficient of NACA0012 airfoil, $\alpha = 4^\circ$, T_∞ = 262.04 K, U_∞ =102.8 m/s.

2.2.2 Droplet-Trajectory Analysis Module

The droplet-trajectory analysis module was verified by comparing the computed collection efficiency with the experimental results obtained. As shown in Table 2.1 ,

a set of validation cases was chosen considering various factors such as the airfoil geometry, MVD, LWC, and freestream velocity [61].

Table 2.1 Validation conditions [61].

	A	B
Airfoil	GLC305	NACA652145
α [˚]	6	0
c [m]	0.9144	0.9144
V_∞ [m/s]	78.68	78.68
LWC [g/m³]	0.22	0.15
MVD [μm]	92	21

A comparison of the collection efficiency obtained by the present calculation, icing wind-tunnel test by NASA, and NASA LEWICE is summarized in Fig. 2.17 and Fig. 2.18. In case A of the GLC305 airfoil, the size of the droplets is large, and the resulting drag is significant. Hence, the droplet trajectory tends to take straight paths, and the collision area covers a wide range of the surface. In case A, there is large discrepancy between the experiment and numerical simulations. This is caused by the distributed polydispersed droplets in the experiment. Droplets are released through the spray system. As the droplet size increases (92μm), the spray system has difficulty to maintain the specific size of droplet. Therefore, the droplet cloud has various size of droplets.

On the other hand, the droplet size is relatively small for NACA65$_2$145 (Case B), and as a result, the drag on the droplets is smaller. Accordingly, the droplets tend to detour the airfoil surface, and the collection efficiency decreases. For both cases, the collection efficiency has its maximum at the stagnation points and tends to decrease towards the trailing edge.

LEWICE overestimates the collection efficiency around the impinging limits of the upper and lower surfaces. The present method appears to achieve an improved prediction of the impinging limits because of the clustering of grid points near the stagnation point. It was developed based on Navier-Stokes equations, and the droplet trajectories were calculated using the Eulerian approach.

A negative collection efficiency was confirmed to not appear in the present calculation because of the improved boundary conditions described in Ref. [53]. Stable convergence was obtained in comparison with the boundary implementation where the droplet velocity and bulk-density gradient on the surface are set to be zero.

Droplets clouds in the nature, usually present themselves with a distribution of droplet diameters instead of the single size droplet. The Langmuir D distribution is a typical one for an icing cloud [62]. Bourgault, Y. et al. [23] studied the effect of the droplet distribution. They compared the collection efficiency between the monodispersed and polydispersed droplets. The Langmuir D distribution was considered for the polydispersed droplets. Their study discovered that impingement limits are more accurately predicted with polydispersed droplets. However, if the droplets do not exceed the supercooled large droplet (diameter of droplets > 50 μm),

the overall distribution and peak value of the collection efficiency using the monodispersed droplets also agree with the experiment for small droplet size as illustrated in Fig. 2.18.

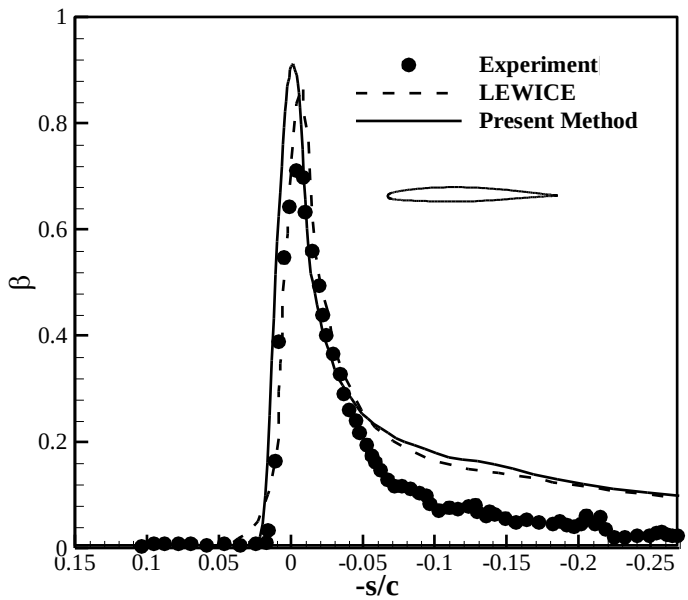

Fig. 2.17 Collection efficiency of GLC305 airfoil, α = 6 ˚, c = 0.9144 m, LWC = 0.22 g/m³, U_∞ = 78.68 m/s, MVD = 92 μm [61].

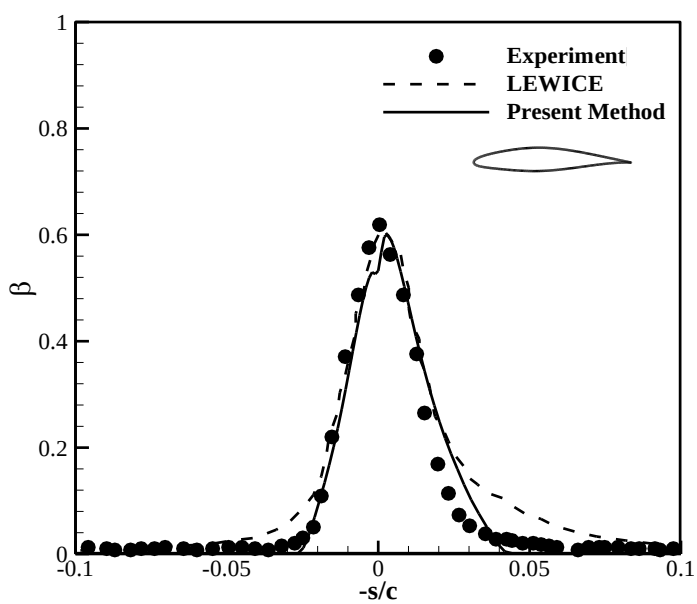

Fig. 2.18 Collection efficiency of NACA65$_2$145 airfoil α = 0 ˚, c = 0.9144 m, LWC = 0.15 g/m³, U_∞ = 78.68 m/s, MVD = 21 μm [61].

2.2.3 2D Ice-Accretion Shape for 2D Airfoil

To validate present solver, 2D ice horn shape, and rime ice shape and are compared with experimental data and other numerical simulations. Each icing condition is summarized in Table 2.2. In both cases, the ice accretion shapes are calculated by four-time steps, and the final ice shapes are depicted in Fig. 2.19. Fig. 2.19 (a) shows the rime ice shape. Due to low temperature, most impinging droplets freeze immediately without heat transfer. In this case, the predicted local collection efficiency determines the overall ice shapes. Since the present result agrees with the experimental ice shape in the maximum thickness of the ice and impingement limits, it can be inferred that the local collection efficiency was well predicted. Fig. 2.19 (b) shows ice horn shape. NASA IRT test [63] and FENSPA-ICE [64] results are overplotted in Fig. 2.19 (b). An ice horn occurs because of the high temperature and LWC. In the glaze ice horn case, not only the collection efficiency but also the heat convection coefficient is important to predict the ice horn. The length and the angle of ice horn are well predicted by the present code compare to NASA LEWICE [63] and FENSAP-ICE [64].

Table 2.2 Validation conditions for 2D airfoil

Condition	Rime ice [63]	Glaze ice [63], [64]
Geometry	NACA0012	NACA0012
α [°]	4	4
T_∞ [K]	250.3	262.4
V_∞[m/s]	102.8	102.8
LWC [g/m³]	0.55	1.0
MVD [μm]	20	20
Time [s]	420	231
y/b [%]	-	-
Chord [m]	0.5334	0.5334

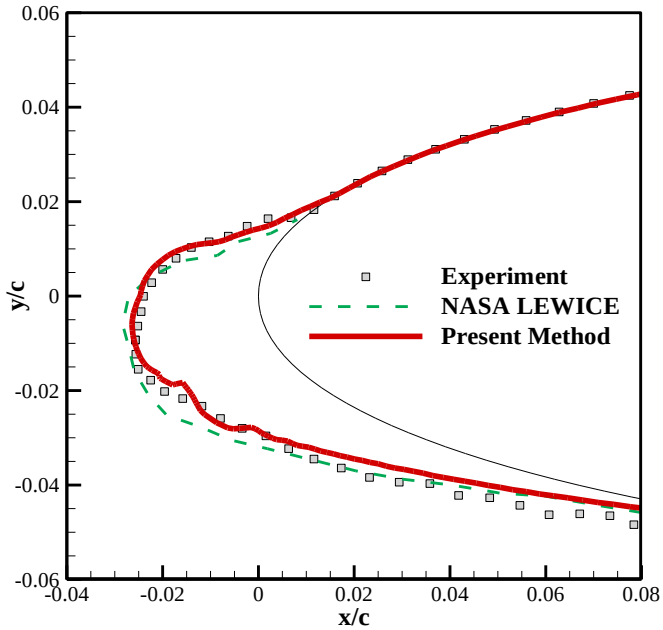

(a) Rime ice

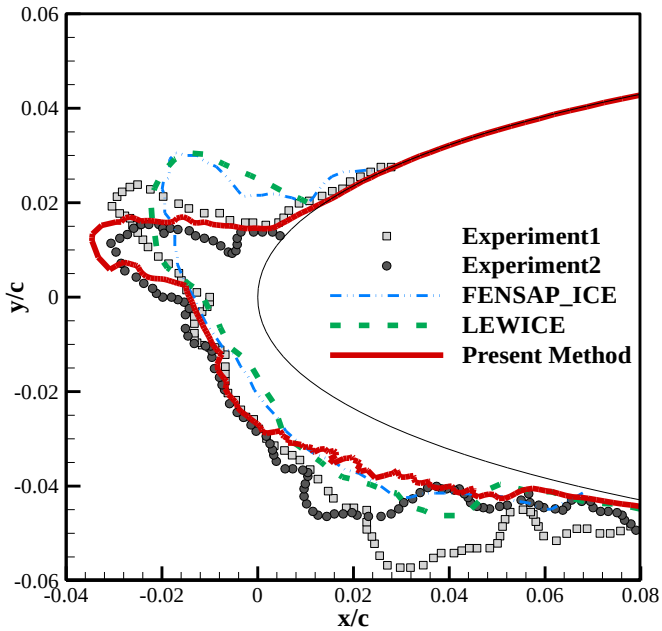

(b) Glaze ice

Fig. 2.19 NASA IRT test results and numerical results

2.2.4 Fixed-wing aircraft (DLR-F6)

To validate the accuracy of the current numerical methods when applied to 3D bodies, DLR-F6 was chosen. Because there are few available experimental data for the ice accretion around the 3D aircraft configuration, the calculation results were verified against those of FENSAP-ICE [65]. The corresponding flow and ambient meteorological conditions are summarized in Table 2.3. The total number of cells used in FENSAP-ICE was 3.9×10^6, whereas around 4.2×10^6 cells were used for the present calculation.

Table 2.3 Validation condition for fixed-wing aircraft [65].

	Icing conditions
Geometry	DLR-F6
α [°]	6
T_∞ [K]	261.5
V_∞[m/s]	76
LWC [g/m³]	0.1
MVD [μm]	20
Time [s]	180
Location (y/S) [%]	10, 30, 50, 70, 98
Chord [m]	0.229, 0.123, 0.104, 0.087, 0.065

The computed ice shapes that accreted on the aircraft surface are shown in Fig. 2.20 and Fig. 2.21, where it is clearly shown that ice is accreted not only at the

leading edge region but also at the trailing edge region. This is because of the angle of attack and cambered geometric features of the wing.

Relatively thick ice shapes are formed around the nose region of the fuselage and the leading edge region because stagnation points exist in those regions, leading to a high collection efficiency. It was clearly illustrated that the present icing-analysis package yields qualitatively similar trends to FENSAP-ICE at locations such as the front part of the fuselage, the leading edge of the wings, and the trailing edge of the lower surface. Compared to those of FENSAP-ICE, the computed cross-sectional ice shapes at 10%, 30%, 50%, 70%, and 98% span-wise locations generally show quantitative agreement. However, the proposed solver slightly overestimates the ice shapes compared to FENSAP-ICE, especially at the 70% and 98% span representing the tip region. Fixing the leading edge as a reference point for y/S = 70% case, the maximum thickness occurs at 0°. The difference of the maximum thickness between FENSAP-ICE and present method is 24%. For y/S = 98% case, the maximum thickness occurs at 35° on the upper surface. The difference of the maximum thickness between FENSAP-ICE and present method is 40%. Except for the maximum thickness at the wing tip region, other major ice-shape parameters, such as the ice-horn direction, and upper and lower icing limits, are in excellent agreement.

(a) Perspective view by present method

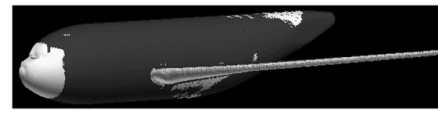

(c) Perspective view by FENSAP-ICE

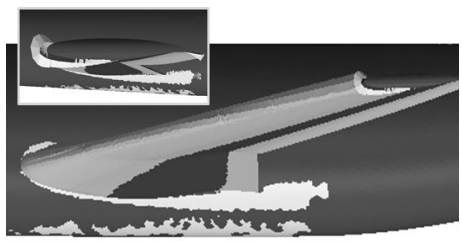

(b) Close view of the main wing region by present method

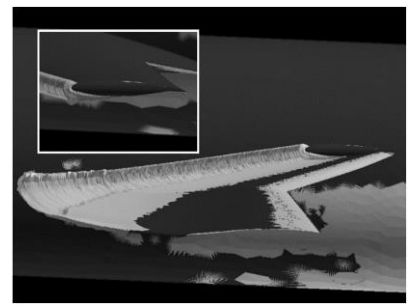

(d) Close view of the main wing region by FENSAP-ICE[65]

Fig. 2.20 Comparison of ice-accretion shapes

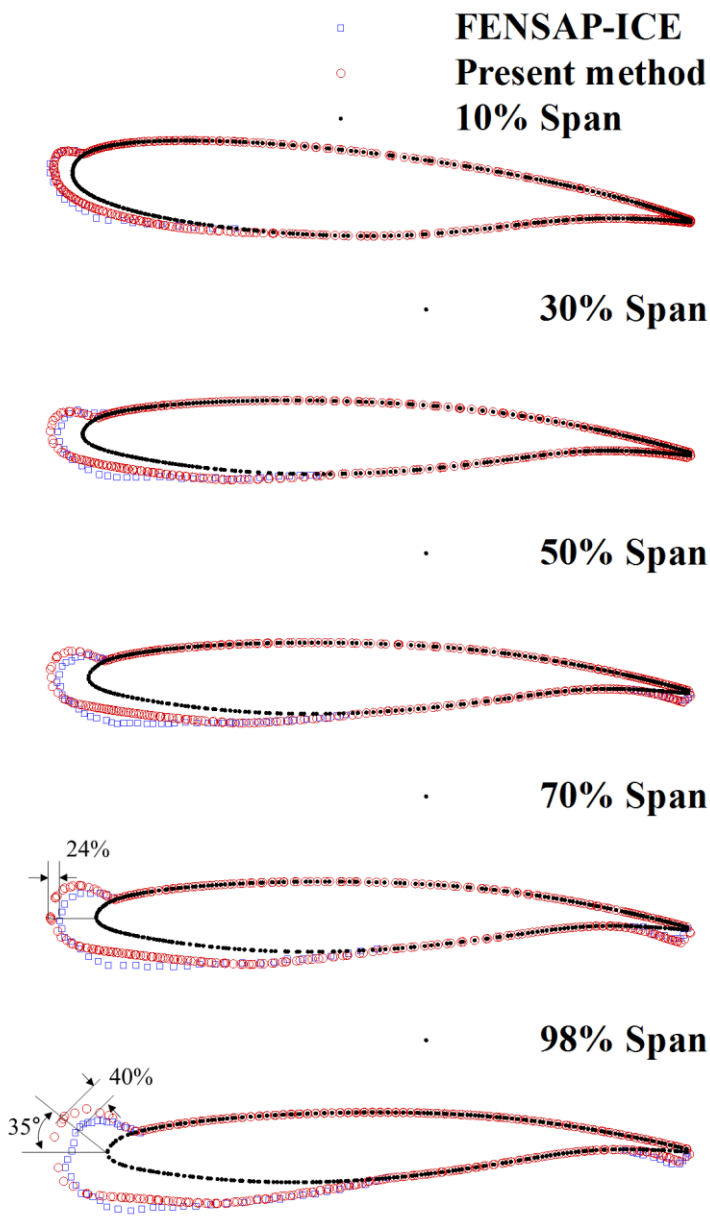

Fig. 2.21 Sectional ice accretion shapes [65]

2.2.5 Helicopter Fuselage

To validate the current numerical methods when applied to the helicopter fuselage, ROBIN was chosen. Because there are few available experimental data for the ice accretion around the ROBIN configuration, the calculation results were verified against those of FENSAP-ICE [43]. The corresponding flow and ambient meteorological conditions are summarized in Table 2.4. The surface roughness value is set as 1.7 mm based on the empirical formula proposed by LEWICE [12]. The same grid system as that used for the flow-field analysis was employed.

Table 2.4 Validation condition for helicopter fuselage [43].

	Icing conditions
Geometry	ROBIN
Advance ratio	0.15
C_T	0.0064
T_∞ [K]	263.15
LWC [g/m³]	0.6
MVD [μm]	20
Time [m]	30

The ice accretion shapes obtained by FENSAP-ICE, ADM and ASM, are compared along the center line of the fuselage as shown in Fig. 2.22. The ice accretion shapes from ADM and ASM well agree with the result of FENSAP-ICE.

For quantitative comparison of the ice accretion shapes, maximum thickness (t_{max}), and its location, upper and lower icing limits are selected as shape parameters.

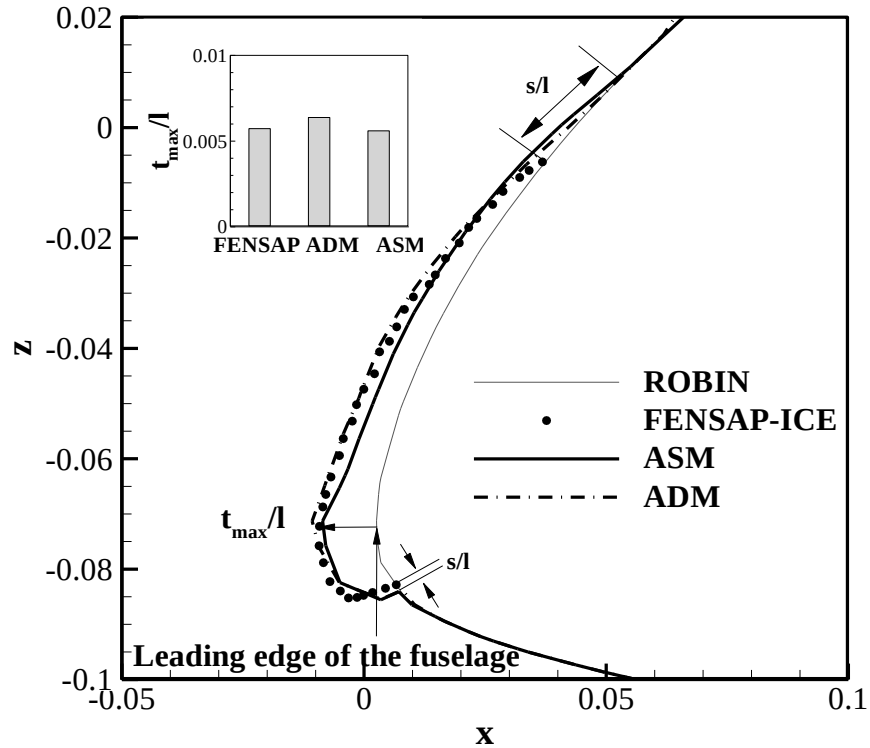

Fig. 2.22 Sectional ice accretion shapes (y=0) , LWC = 0.6 g/m³, MVD = 20 μm, T = -10 °C, 30 min, μ = 0.15.

FENSAP-ICE, ADM, and ASM predict the location of maxim thickness at the leading edge of the fuselage where the mass of impinging water is high. The difference of the maximum thickness is under 11% between FENSAP-ICE and present methods. The icing limit of the upper surface depends on inflow as can be expected. FENSAP-ICE, ADM, and ASM yield the inflow in different ways. As mentioned above, FENSAP-ICE adopts Drees's linear inflow model. Therefore,

there is a discrepancy of the upper icing limit. The distance of the upper icing limits (s/l) between the FENSAP and ADM is 0.64%, and ASM is 0.73%. However, the influence of the inflow to the lower icing limit is relatively lower than that of the upper surface. The distance of the lower icing limits between the FENSAP and ADM within 0.067%.

3. HALE Aircraft Icing

3.1 Establishing the Analytical Procedure

By the following procedures as depicted in Fig. 3.1. The procedure to determine the operational limits of HALE aircraft, the success or failure of a mission can be forecasted based on the meteorological data. (1) The EAV-2H+ is selected as a baseline HALE aircraft: developed by the Korea Aerospace Research Institute, this aircraft has been successfully flown as a communications and internet relay [37], [56]. (2) The icing conditions are selected based on the mission profile; the icing environment is chosen from FAR, Part 25 Appendix C [8], which presents an industry standard for airworthiness certification. (3) A series of numerical analyses are performed to obtain the ice accretion shapes on the 3D HALE aircraft under the selected icing conditions. (4) The aerodynamic performance degradation of the HALE aircraft due to icing and the mass of the ice is calculated; in addition, the relation between the configurational characteristics of accreted ice and aerodynamic performance are qualitatively investigated. (5) To correlate the icing environment variables with the aerodynamic performance degradation, the RSMs are constructed: the aerodynamic performance degradation is given as a function of meteorological data such as LWC and ambient temperature. (6) The constructed RSMs are applied to calculate the total power required to reach the mission altitude. By comparing the calculated total required power with the installed battery capacity, the success or failure of the mission can be inferred. Therefore, from the proposed model, the

operator can determine the meteorological conditions that are potentially hazardous to flights.

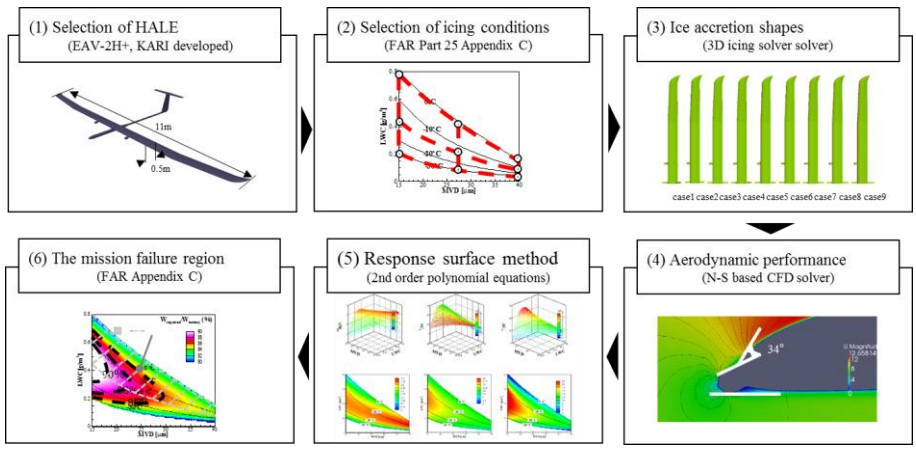

Fig. 3.1 The procedure to determine the operational limits of HALE aircraft

3.1.1 Baseline Configuration: EAV-2H+

The baseline HALE aircraft used in this study is EAV-2H+, developed by KARI in 2014 [37], [56] and shown in Fig. 3.2. This HALE aircraft holds a record for performing a seven-hour mission at an altitude of 10 km. Thrusted by two propellers, EAV-2H+ is equipped with communications and observation devices. To supply these devices with electric power, solar cells are used as the power source in the daytime, and a rechargeable Li-ion battery is used at night. The rechargeable battery capacity is 3 kWh. The MTOW is 20 kg, and the empty weight is 13 kg. The structural weight to wing loading ratio is only 1.27 to maintain the ultra-light structure of EAV-2H+, and therefore, the aircraft is not equipped with ice protection systems.

For the main wing, EAV-2H+ uses a single airfoil, SG6043, which has excellent aerodynamic characteristics at low Reynolds numbers. Solar cells are attached to the outboard upper surface of the main wing at the span of 11 m and a chord length of 0.5 m. NACA0010 and NACA0012 are chosen for the horizontal and vertical tail wings, respectively [37]. Table 3.1provides more detailed data on EAV-2H+.

Table 3.1 Specifications of baseline HALE aircraft

Description	Values
MTOW	20 kg
Empty weight	13 kg
Main wing	Airfoil: SG6043; span: 11 m; chord: 0.5 m
Horizontal tail	NACA0010, Area: 0.4 m²
Vertical tail	NACA0012, Area: 0.386 m²
ROC	1 m/s
Battery capacity	3 kWh
Incidence angle	2.3
$\overline{C_L}$	1.0
$\overline{C_D}$	0.033
$V_{\infty, \text{clean}}$	7.6 m/s at ground, 13.13 m/s at 10 km

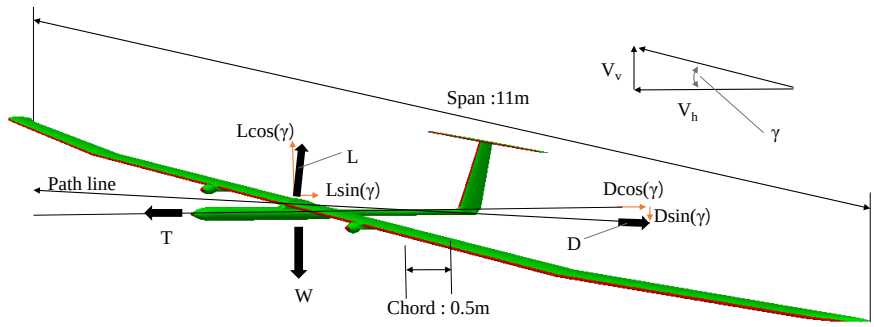

Fig. 3.2 EAV-2H+ appearance and free body diagram

A pair of propellers is installed under the wing at y/b = 20%. Depending on the ambient conditions, ice may accumulate on the propellers as well, which degrades the propeller efficiency and increases the required power. In addition, the propeller wake may affect the droplet behaviors and ice accretion shapes. However, considering the high aspect ratio of the wing and the relatively narrow area influenced by the wake, the effects of the propellers are assumed to be negligible in the present icing analysis and aerodynamic performance analysis.

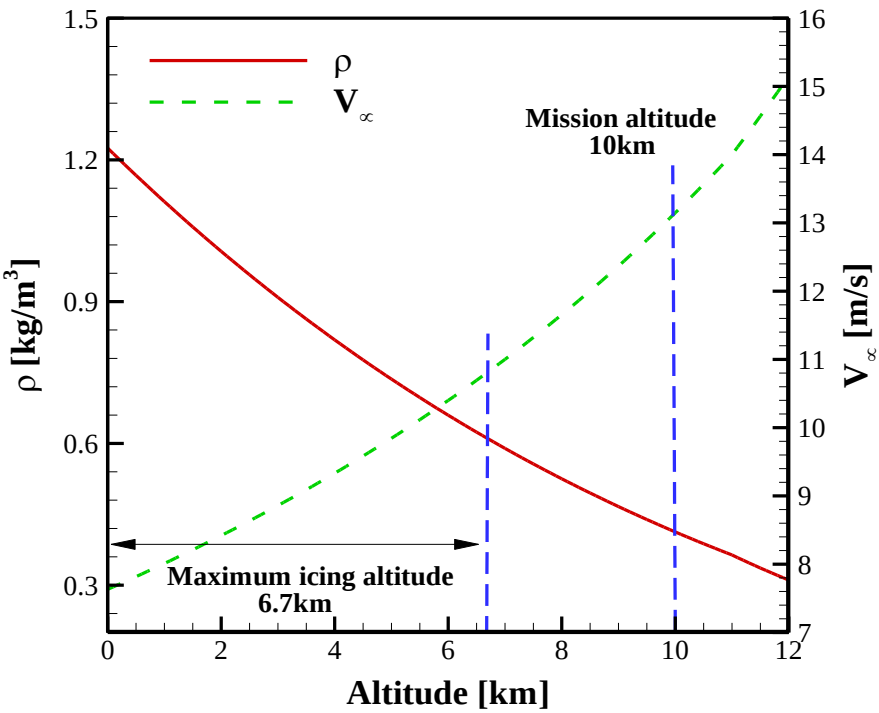

Fig. 3.3 Changes in density and flight speed according to altitude

The EAV-2H+ climbs to the mission altitude at the constant ROC of 1 m/s regardless of altitude. At the mission altitude, the EAV-2H+ uses solar cells to charge the battery and operates the propellers and mission equipment during the day. As shown in Fig. 3.3, because the air density decreases with altitude, the EAV-2H+ slowly speeds up with altitude to compensate for the lift loss. As a result, the EAV-2H+ flight speed is 7.6 m/s near the ground level and is increased to 13.13 m/s at the mission altitude.

3.1.2 Selection of the Icing Environment

The icing environment is determined based on the designated mission profile of baseline HALE aircraft. Toward this objective, it is necessary to determine the cloud type, exposure time, LWC, MVD, and ambient temperature. Each parameter and its range are set through the following process. Here, FAR Part 25 Appendix C, which describes the icing environments for airworthiness certification, is used as a reference [8].

FAR Part 25 Appendix C classifies the range of meteorological parameters under which an aircraft is certified according to the cloud type, which is broadly categorized as cumulus and stratus. Although cumulus clouds usually indicate severe meteorological conditions, their range of distribution is narrow (< 4 km), and they are therefore less frequently encountered by operators. Hence, in this research, stratus cloud conditions are applied to set the ranges of ambient temperature, LWC, MVD, and exposure time.

FAR Part 25 Appendix C specifies the maximum vertical extent and the maximum icing altitude of stratus clouds as 2 km and 6.7 km, respectively. It can take into account a single stratus cloud layer with the 2 km vertical extent. According to a study of varied vertical cloud structures from a 20-year global rawinsonde dataset [66], the frequency of layered clouds is very high. Globally, 58% of clouds are single layers, and 42% are multilayered; almost 33% of the latter are consist of more than three layers. In addition, other research [67] on vertical cloud structure has shown that when layered clouds are formed, high humidity is maintained

between each the cloud layers, and this condition results in the persistent accumulation of ice on the HALE aircraft, which does not have ice protection systems. Therefore, the total exposure time is assumed to be 1.86 hours to provide an extremely conservative model of the conditions. This duration corresponds to the time required for the HALE aircraft to reach the maximum icing altitude of 6.7 km, above which the water droplets no longer exist in the atmosphere. The limitation of this research is that the icing conditions are assumed as constant from sea-level to 6.7 km. By considering variations of MVD, LWC and temperature with altitude and vertical cloud structure, more realistic icing conditions could have been achieved Future work should include realistic variations of icing conditions according to altitude and cloud structure in order to improve the fidelity of the icing predictions.

The ranges for the LWC, MVD, and ambient temperature are determined according to the FAR Part 25 Appendix C conditions as illustrated in Fig. 3.4, where LWC ranges from 0.04 to 0.8 g/m³, and the ambient temperature varies from -30 to -1.4°C. Because the icing phenomenon does not occur at 0°C, the highest stagnation temperature is set as -1.4°C [63]. Two independent variables are used to construct RSMs in this study: the LWC and temperature. In Fig. 3.4, the variables LWC, MVD, and temperature appear to be independent; however, these are not, in fact, independent. When two variables are given, the other variable is uniquely determined from the first two. For example, if the LWC is 0.2 g/m³ and the MVD is 25 μm, the temperature is -20°C. RSMs could be made from the two independent variables, LWC and MVD; however, because direct MVD measurements are

difficult, it is advantageous for operators to be able to use temperature instead of MVD.

Eventually, nine sets of analysis conditions were set for the selected LWCs and ambient temperatures. The nine selected cases from the FAR Part 25 Appendix C that were selected for icing analysis and meta-model construction are summarized in Fig. 3.4 and Table 3.2.

Table 3.2 Constructed icing conditions from FAR Part 25 Appendix C [8]

Case No.	LWC [g/m³]	T [°C]	MVD [μm]
1	0.77	-1.4	15
2	0.456	-14.25	15
3	0.2	-30	15
4	0.41	-1.4	27.5
5	0.21	-14.25	27.5
6	0.083	-30	27.5
7	0.144	-1.4	40
8	0.08	-14.25	40
9	0.04	-30	40
Common values			
ρ[kg/m³]	0.8784 at 3.35km		
Time[h]	1.86h until 6.7km 2.78h until 10 km		

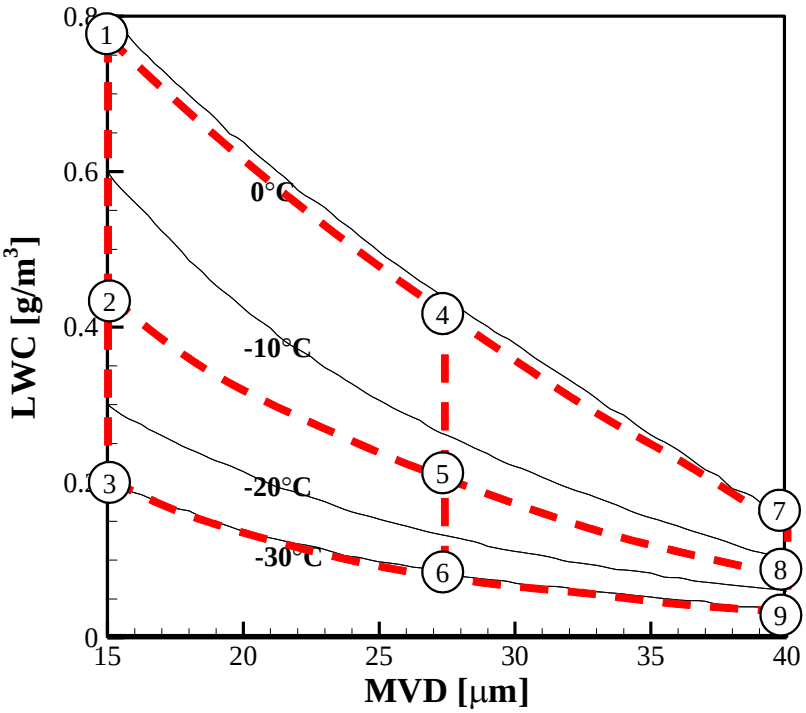

Fig. 3.4 Selected icing conditions from FAR Part 25 Appendix C [8]

3.1.3 One-Shot Method

From Fig. 3.3, in order to consider the changes in density and speed that occur with increasing altitude, the unsteady approach is appropriate for modeling the flow fields, droplet fields, and thermodynamic analyses. However, the enormous computing resources required for the unsteady 3D icing analysis over an icing exposure time of 1.86 hours would prohibit icing and aerodynamic analyses for the nine selected analysis conditions. Therefore, a one-shot method is used to obtain the ice shapes, and then the resulting aerodynamic performance for all conditions. Here

the one-shot method means that ice shapes without any mesh deformation during the entire icing exposure time by the quasi-steady-state approximation.

To confirm the validity of the one-shot method, the results using the one-shot method are compared against those of the multi-step method, where the mission altitude is divided into five equal intervals by quasi-steady assumption, and then the ice shape prediction and aerodynamic analysis are performed for each interval based on a quasi-steady assumption as shown in Fig. 3.5. In principle, the multi-step method should yield more accurate results than the one-shot method.

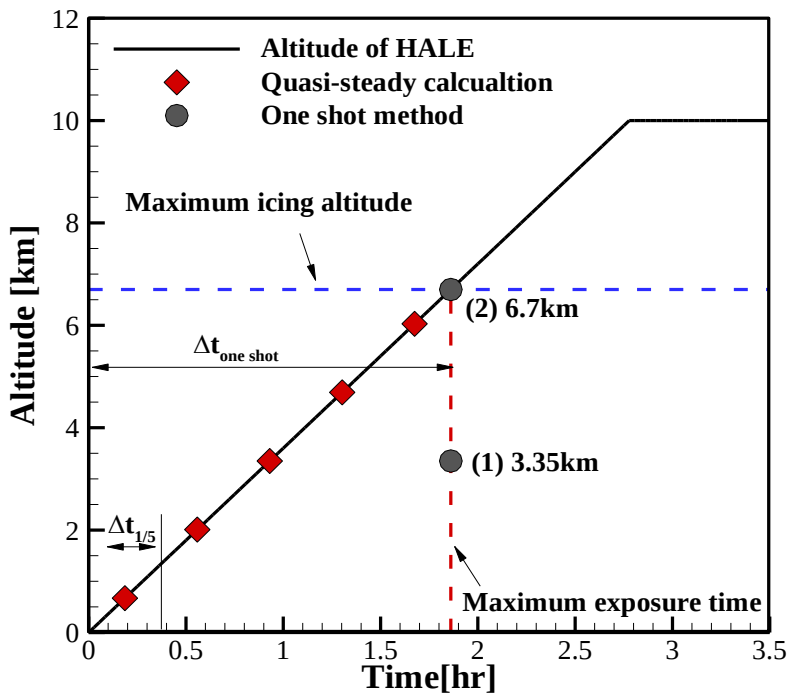

Fig. 3.5 Calculated points from one-shot and multi-step methods

Since the 3D multi-step method requires tremendous calculation resources and time, the 2D analysis was performed from the given icing conditions. This comparison was made for an SG6043 airfoil, which is used for the main wing of the baseline HALE aircraft. The ice shape in the first interval is obtained by performing icing analysis on the initial clean airfoil. This first ice shape is then used as the initial shape to produce the aerodynamic performance for the second interval, and the same process is repeated until the final interval, adjusting the flight speed to keep the lift constant regardless of altitude. Thus, the aerodynamic coefficients at each interval are obtained from the ice shape in the previous interval.

In the one-shot method, it is unclear at which altitude the air density and flight speed should be taken. At the altitude of 3.35 km, the air density is 0.8784 kg/m^3, and the flight speed is approximately 9.03 m/s, whereas, at the altitude of 6.7 km, the air density and flight speed are 0.610 kg/m^3 and 10.82 m/s, respectively. Hence, air density and flight speed are taken at the altitudes of 3.35 km and 6.7 km, and both results are compared with those of the multi-step method. The relative changes in the aerodynamic performance coefficients and the maximum ice thickness are systematically compared, with the results of the multi-step method set as the reference values used to calculate the relative changes.

Fig. 3.6 compares the ice accretion shapes obtained for Cases 1, 5, and 9. The Fig. 3.6 shows that the ice shapes based on the air density and flight speed at 3.35 km are qualitatively and quantitatively closer to the results of the multi-step method. To quantitatively compare the ice accretion shapes, the maximum ice thickness

measured from the leading edge is used as an ice shape parameter. For the three cases, the relative changes in the maximum thickness from the one-shot method at 3.35 km are 26%, 6%, and 16%, respectively, whereas the one-shot method at 6.7 km yields relative changes in maximum thickness of 39%, 21%, and 28%, respectively. This indicates that the relevant parameters such as air density and flight speed should be taken in the middle of the entire interval when using the one-shot method.

The validity of the one-shot method for 3D HALE aircraft is also examined. Fig. 3.6 (b) shows the sectional ice shape of the wing obtained at the mid-span using the one-shot method at 3.35 km for Case 5. The ice accretion shape of the 3D wing center (y/b =50 %) matches the ice shapes obtained by the multi-step method. Based on this result, the 3D ice accretion shapes obtained using the one-shot method were considered reasonable at the 3.35 km altitude.

Fig. 3.7 summarizes the lift and drag coefficients from the ice shapes for Cases 1, 5, and 9. The lift and drag coefficients in the final step of the multi-step method show a good match with those from the one-shot method using the data at 3.35 km. For all cases, the maximum relative change in the lift coefficient is only 2.5%, and for the drag coefficient, the maximum relative change is less than 3.5%. On the other hand, the results at 6.7 km produce maximum relative changes in the lift and drag coefficients of 1.8% and 11.2%, respectively. To ensure an accurate required power calculation, a more precise drag prediction is essential. Accordingly, all of the following computations are performed based on the one-shot method, where all the meteorological and flight parameters are taken in the middle of the entire interval.

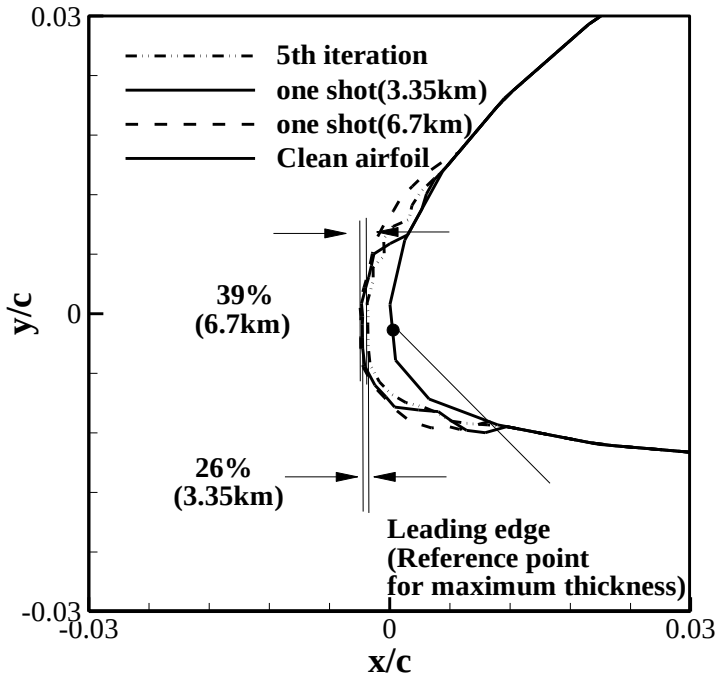

(a) Case 1 (LWC = 0.77 g/m³, T = -1.4°C, MVD = 15 μm)

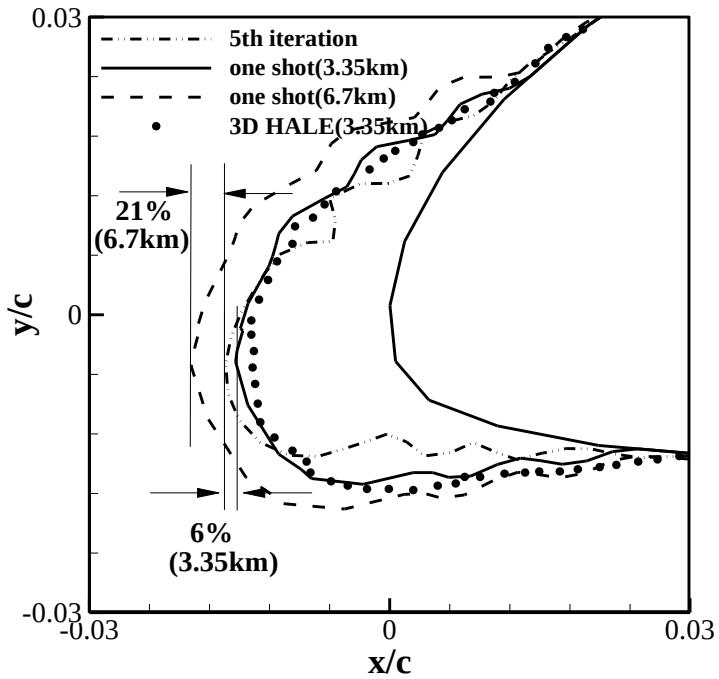

(b) Case 5 (LWC = 0.21 g/m³, T = -14.25°C, MVD = 27.5 μm)

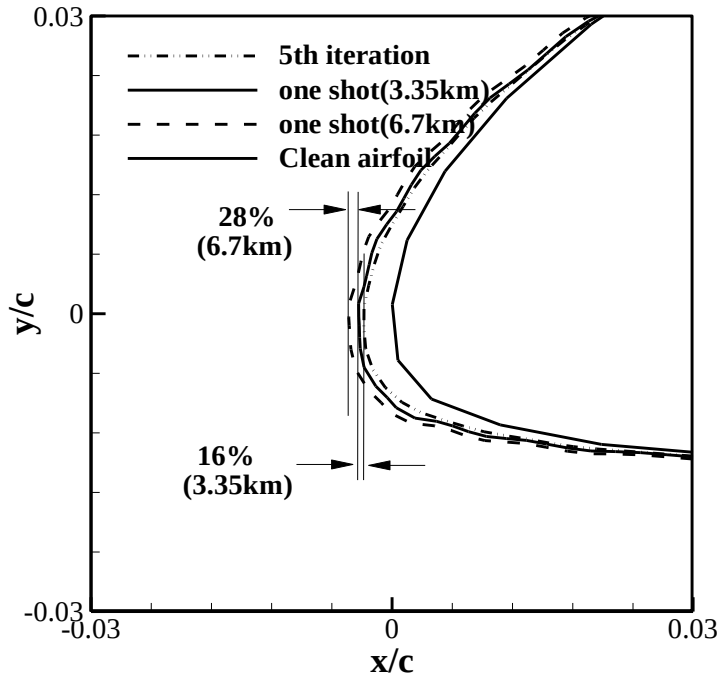

(c) Case 9 (LWC = 0.04 g/m³, T = -30°C, MVD = 40 μm)

Fig. 3.6 Comparison of ice accretion shapes between the multi-step method and the one-shot method

To estimate the required power to reach the mission altitude, the time-varying lift and drag forces should be calculated. However, the one-shot method is inherently limited in its capacity to consider changes in the lift and drag coefficients over the exposure time. Therefore, proper assumptions are required to estimate the time-varying lift and drag forces before using the one-shot method. Fortunately, the ice shape grows gradually, maintaining the direction of the ice formation without ice horns. As a result, the lift and drag vary almost linearly over time, as illustrated in Fig. 3.7. When the lift and drag coefficient are calculated, each icing conditions are applied including clean airfoil. In all cases, the maximum lift and drag discrepancies

were found to be within 2.6% and 3%, respectively, at each step along the straight line between the clean airfoil and the final ice shape. A similar observation was made by Sand et al. [68], who performed a series of experiments to evaluate changes in aerodynamic performance under icing conditions. These researchers also found that the lift-to-drag ratio almost linearly decreased over time. Hence, it is reasonable to assume hereafter that the lift and drag coefficients change in a linear manner over the exposure time under icing conditions.

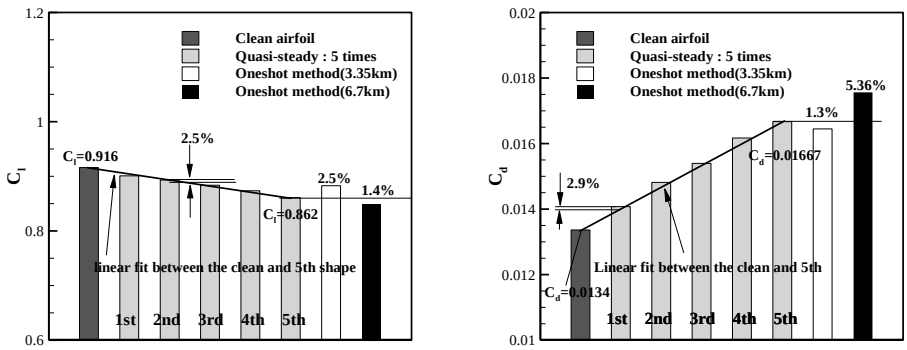

(a) Case 1 (LWC = 0.77 g/m³, T = -1.4°C, MVD = 15 μm)

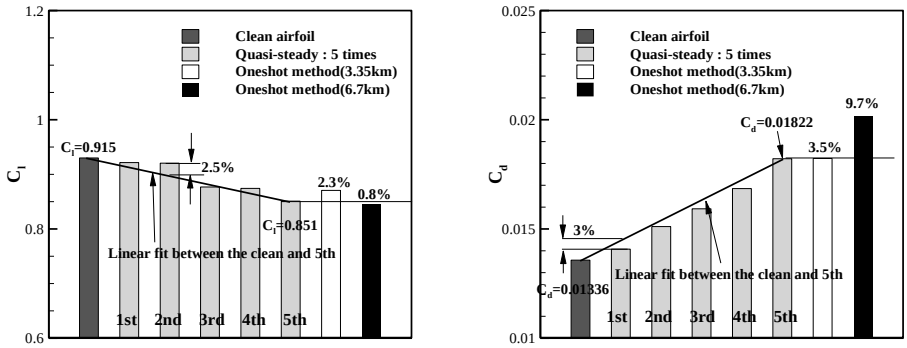

(b) Case 5 (LWC = 0.21 g/m³, T = -14.25°C, MVD = 27.5 μm)

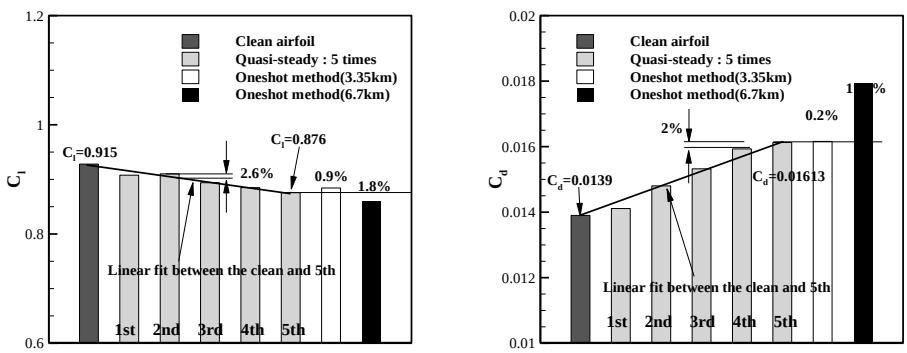

(c) Case 9 (LWC = 0.04 g/m³, T = -30°C, MVD = 40 μm)

Fig. 3.7 Comparison of lift and drag coefficients between the multi-step method and the one-shot method

3.1.4 Response Surface Models (RSMs)

When icing is expected, operators should collect meteorological data such as LWC, ambient temperature, pressure, and density. However, determining whether an actual mission flight is possible based on atmospheric data is difficult without knowing the predicted ice accretion shapes and the resulting aerodynamic performance. In this research, second-order polynomial RSMs are constructed to quantify the performance degradation of HALE aircraft as a function of the icing environment variables as explained in Eq. (3-1) [69]. Operators can use these regression models to make a decision based on a quantitative assessment of the performance when icing occurs.

$$y_i = C_0 + C_1 x_1 + C_2 x_2 + C_{11} {x_1}^2 + C_{12} x_1 x_2 + C_{22} {x_2}^2 \quad (3\text{-}1)$$

Here, x_1 and x_2 are the LWC and ambient temperature, respectively; and y_1, y_2, and y_3 denote ΔM_{ice}, ΔC_L, and ΔC_D. Eqns. (3-2) – (3-4) define the percent change in the mass, lift, and drag coefficients, respectively.

$$\Delta M_{ice} = m_{ice}/MTOW \quad (3\text{-}2)$$

$$\Delta C_L = \left|C_{L,clean} - C_{L,ice}\right| / C_{L,clean} \quad (3\text{-}3)$$

$$\Delta C_{\mathrm{D}} = \left|C_{\mathrm{D},clean} - C_{\mathrm{D},ice}\right| / C_{\mathrm{D},clean} \quad (3\text{-}4)$$

The constructed RSMs are verified with cross-validation, R^2, and R_{std}, where R^2 is a measure of the amount of reduction in the variability of y_i obtained using the input variables x_1, and x_2 in Eq. (3-1); and R_{std} is the standardized residual, determined from the division of a residual by an estimate of its standard deviation. Fig. 3.8 shows the cross-validation results, where the x-axis represents the performance changes from the meta-models (ΔM_{ice}, ΔC_L, and ΔC_D), and the y-axis represents the performance changes from the CFD calculation. When both sets of values are located along the x = y line, it can be said that the RSM matches well with the CFD calculations. The ΔM_{ice}, ΔC_L, and ΔC_D values obtained using the RSMs are located within the range of three standard deviations.

It is known that the R_{std} of a well-constructed RSM has a value between -3 and 3 [69]. In the models constructed here, the values are between -2 and 2, and the R^2 values of ΔM_{ice}, ΔC_L, and ΔC_D are 0.8602, 0.8084, and 0.8822, respectively. Although the RSMs have a relatively low R^2 because of the small number of sampling points and the inherent nonlinearity of the problem under consideration, they are nonetheless sufficient to indicate the general relationship between the meteorological parameters and aerodynamic performance degradation.

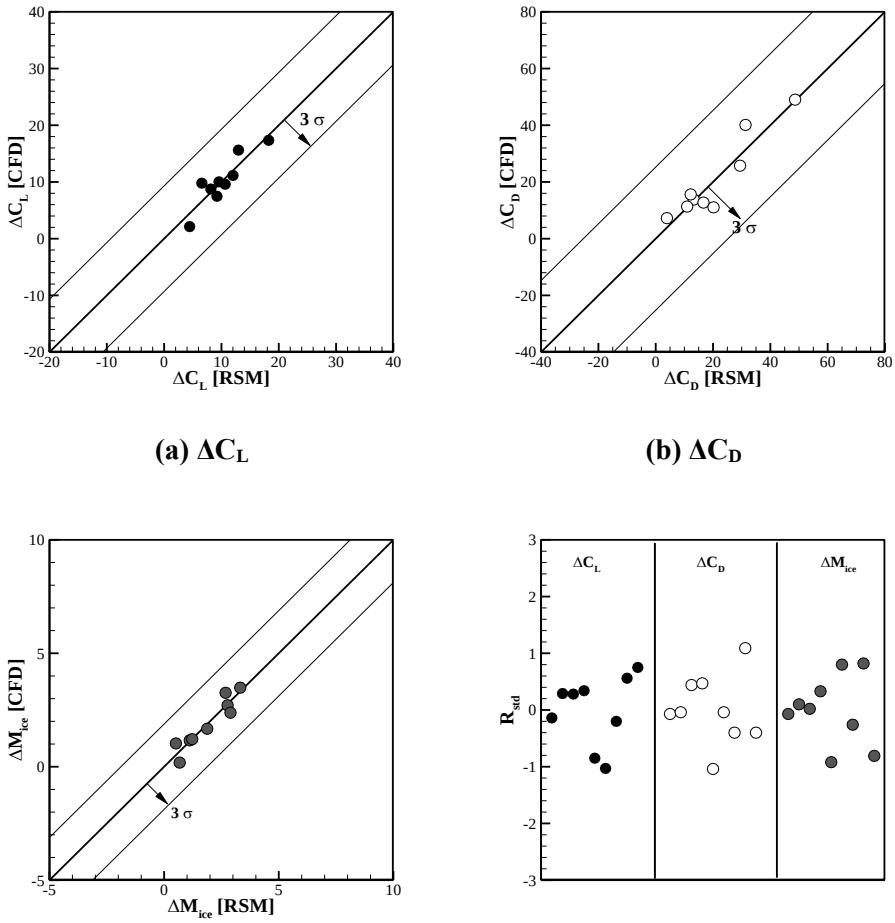

(a) ΔC_L **(b) ΔC_D**

(c) ΔM_{ice} **(d) R_{std}**

Fig. 3.8 Comparison of lift and drag coefficients between the multi-step method and the one-shot method

3.1.5 Performance Analysis

Quantitative correlations between the meteorological data and aerodynamic performance are essential to assess the operational capability of the HALE aircraft under icing conditions. However, operators cannot judge the success of missions by

the quantitative correlations alone, and this paper, therefore, suggests that required power is an appropriate indicator. When icing occurs on the HALE aircraft, the power required to reach the mission altitude increases because of the aerodynamic performance degradation. In this research, it is assumed that if the iced HALE aircraft can attain the mission altitude using the installed battery, the mission can be successfully completed because the ice accreted on the HALE aircraft will disappear after a certain amount of time with sublimation at the mission altitude [34]. In order to calculate the power required for the HALE aircraft to reach the mission altitude, the following assumptions are made.

First, the ROC is kept constant at 1 m/s. If no special adjustment is taken, the ROC of the HALE aircraft will be reduced due to icing. In this case, the time to reach the mission altitude is delayed, and there will not be sufficient time for the solar cells to charge the battery capacity that is used at night. Second, the reduction in lift due to icing and low density is compensated for by increasing the flight speed instead of adjusting the angle of attack: because the stall margin is already reduced with icing, an increased angle of attack may pose a potential hazard to flight safety. Third, the lift and drag coefficients and ice mass alter in a linear manner from the ground to the maximum icing altitude (6.7 km) as in Eqns. (3-5) – (3-7). Above the maximum icing altitude, the aerodynamic performance and ice mass are assumed to be constant because the ice shape no longer changes in the absence of water droplets.

$$D(t) = \frac{1}{2}\rho(t){V_h}^2(t)AC_{D,clean}[1 + \Delta C_D t/t_{ice}] \quad (3\text{-}5)$$

$$L(t) = \frac{1}{2}\rho(t){V_h}^2(t)AC_{L,clean}[1 - \Delta C_L t/t_{ice}] \quad (3\text{-}6)$$

$$M(t) = M_{clean}[1 + \Delta M_{ice} t/t_{ice}] \quad (3\text{-}7)$$

Fourth, the efficiency parameters of the propeller, battery, motor, and motor controller are taken from the clean condition. Here, the efficiency values of the battery (η_{bat}), propellers (η_{pro}), motors (η_{mot}), and controllers (η_{con}) are 90%, 60%, 88%, and 95%, respectively. The propeller surfaces are usually coated with antifreeze before the flight, and it is therefore reasonable to assume a constant propeller efficiency, although there is a possibility that the propeller efficiency will decline with icing.

Fig. 3.2 depicts the free body diagram of forces acting on the HALE aircraft. The vertical and horizontal force equilibria are set as in Eqns. (3-8) and (3-9), respectively. The flight path angle (γ) can be calculated using the ROC and the angle of attack.

$$L(t)cos(\gamma) = W(t) + D(t)sin(\gamma) \quad (3\text{-}8)$$

$$T(t) = D(t)cos(\gamma) + L(t)sin(\gamma) \quad (3\text{-}9)$$

The required power is calculated from the thrust, flight speed, and total efficiency (η_{tot}) of the propeller as in Eq. (3-10), where the total efficiency (η_{tot}) is given by Eq. (3-11). The total power (W) required to reach the mission altitude is then obtained by integrating the power ($P(t)$) during the climbing stage (t_m) as in Eq. (3-12).

$$P(t) = T(t)V_h(t)/\eta_{tot} \tag{3-10}$$

$$\eta_{tot} = \eta_{bat}\eta_{pro}\eta_{mot}\eta_{con} \tag{3-11}$$

$$W_{req} = \int_0^{t_m} P(t)\, dt \tag{3-12}$$

3.2 Results and Discussion

In this section, the configurational characteristics of ice accretion shapes on a low-speed HALE aircraft are analyzed to elucidate the cause of the aerodynamic performance degradation. In addition, the constructed RSMs are analyzed and subsequently used to estimate the total power required to climb to the mission altitude under the icing conditions presented in the FAR Part 25 Appendix C. Finally, the range of meteorological parameters under which the HALE aircraft could successfully accomplish its mission is presented.

3.3.1 Features of Ice Shapes on 3D HALE aircraft

The ice accretion shape on the entire surface of the HALE aircraft is illustrated in Fig. 3.9, which corresponds to Case 5 with the highest total ice mass. Fig. 3.9 clearly shows that most of the ice is accumulated on the fuselage nose and in a narrow region on the leading edge of each wing. As can be seen in Fig. 3.9 (c), there is no ice on the solar cell surface; therefore, icing has little impact on the charging capability of solar cells.

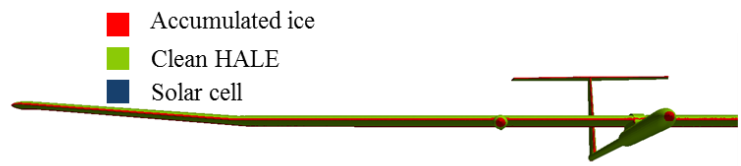

(a) Front view

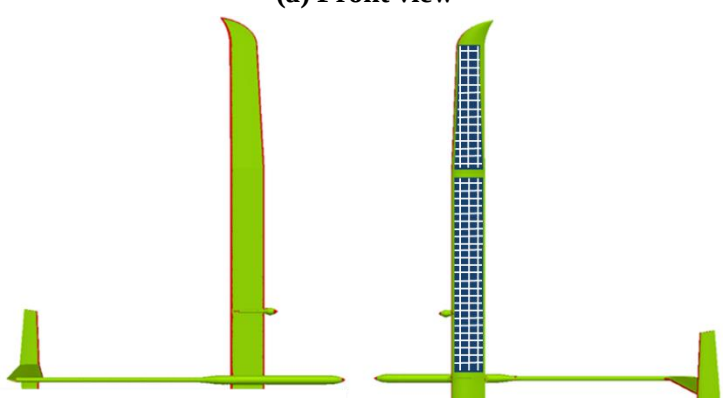

(b) bottom view **(c) top view**

Fig. 3.9 Ice accumulated on the HALE aircraft (Case 5: LWC = 0.21 g/m³, T = -14.25°C, MVD = 27.5 µm, V = 9.029 m/s)

Fig. 3.10 illustrates the sectional ice shape at the location of y/b = 50% from the 3D calculations for nine icing conditions, from which the influence of each meteorological parameter on the ice accretion shapes can be identified. In this figure, the vertical axis represents the change in MVD, and the horizontal axis represents LWC and temperature differences.

As MVD increases from 15 μm to 30 μm, the wetted area where the icing occurs becomes larger. The ice-covered frontal area in Case 7 is 2.3 times larger than that in Case 1. The upper icing limit also increases in high MVD conditions from x/c = 0.3% to x/c = 3%. Fortunately, in all cases, ice does not accrete on the upper surface where the solar cells are distributed.

Severe changes in ice accretion shape are detected at mid-temperature (-14.25°C) for the LWC and MVD given in the FAR Part 25 Appendix C. Cases 1, 4, and 7 have the highest LWC and temperature, where unfrozen water film remains on the surface in spite of the high LWC, because of the high temperature. Cases 3, 6, and 9 have the lowest LWC and temperature. In these cases, the temperature is low enough to freeze water; however, the amount of impinging water is insufficient; consequently, only a thin ice layer accretes. Cases 2, 5, and 8 have low LWC and low temperature, which causes all water that impinges on the surface to freeze immediately upon contact and therefore results in the most severe ice shape.

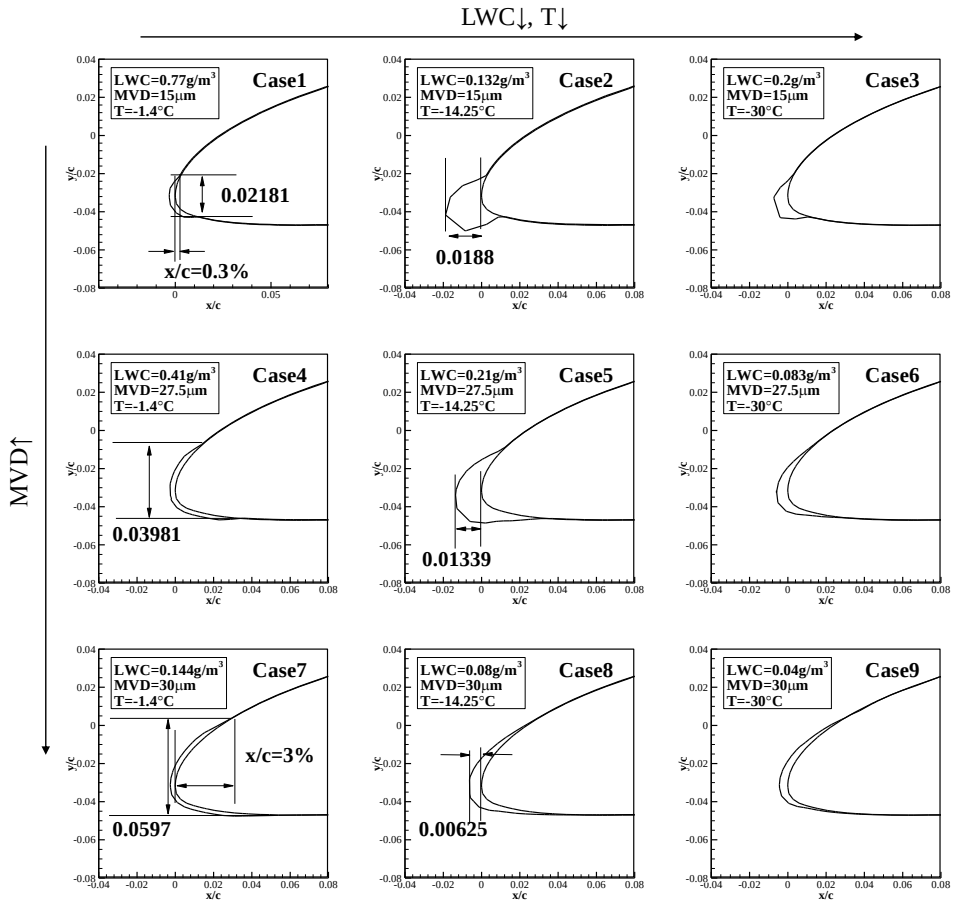

Fig. 3.10 Sectional ice shapes of 3D HALE aircraft at y/b = 50%

The most noteworthy feature of the ice shapes on HALE aircraft is that there is no ice horn even at the relatively high temperature. The characteristics of the ice accretion shape for the low-speed HALE aircraft with various Mach numbers are systematically analyzed using the icing code. Here, the icing condition is applied by following the NASA Icing Research Tunnel (IRT) experiment [63] as depicted in Fig. 2.19 (b) as an ice horn condition.

To investigate the effect of velocity, a numerical analysis was performed on the 2D SG6043 airfoil used in EAV-2H+ under the same icing condition (LWC, MVD, and static temperature) as the IRT test [63] except for the freestream velocity and exposure time. The free-stream Mach numbers are set to 0.033, 0.1, and 0.3, where Mach 0.033 corresponds to the freestream velocity at the maximum icing altitude (6.7 km). The exposure times for numerical simulations are adjusted to be the same as the total mass of impinging water of IRT test condition because the mass of impinging water is the product of LWC, flight speed, and exposure time.

The ice accretion shapes on the SG6043 airfoil are depicted in Fig. 3.11. The rime ice shapes can be observed at Mach 0.1 and 0.033, whereas glaze ice is found at Mach 0.3. At low velocities, below Mach 0.033, the ice shape grows gradually, maintaining the direction of the ice formation without ice horns, whereas in high-velocity conditions of Mach 0.3, the directions of the ice formations grow 70.6˚ upward and 80.5˚ downward, respectively.

There are two main reasons why ice horns do not develop a HALE aircraft even at the relatively high ambient temperature. The first reason is that the total water impinging on the surface of HALE aircraft is less than that of transport category airplanes. The second reason is the low heat transfer rate. Both of these reasons are due to the low flight speed of HALE aircraft.

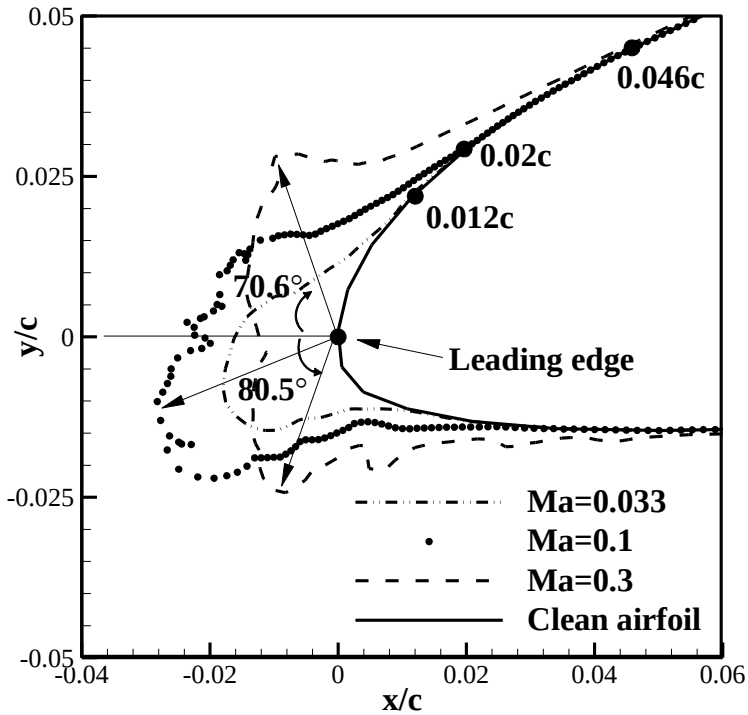

Fig. 3.11 Ice accretion shapes for the airfoil of HALE aircraft at Mach 0.033, 0.1, and 0.3

Eq. (3-13) states that the mass flow rate of impinging water droplets is determined by the total collection efficiency (β_{tot}), LWC, and freestream velocity. Here, the total collection efficiency means the integrated value of the local collection efficiency. For any given LWC, the low freestream velocity results in a smaller mass of impinging water.

$$\bar{\dot{m}}_{com} = \beta_{tot} \cdot LWC_{\infty} \cdot U_{\infty} \tag{3-13}$$

The free flow velocity also affects the droplet trajectory. Because of the low droplet inertia (K) based on the water droplet diameter (MVD), as expressed in Eq.

(3-14), the water droplet tends to detour around the surface instead of impacting on the surface. Therefore, the HALE aircraft has a lower peak collection efficiency value. Fig. 3.12 clearly shows that the peak collection efficiency value falls by 40% when the Mach number decreases from 0.3 to 0.033.

$$K = \frac{\rho_w V_\infty MVD^2}{18\mu c} \tag{3-14}$$

The low-speed offers the advantage of reducing the frontal area covered by the ice. This can prevent the deterioration of the solar cell efficiency. Because the low inertia of the droplets causes them to avoid colliding with the body, not only the peak collection efficiency value but also the impingement limits are changed. The droplet impingement limit is formed in a narrow region around the stagnation point, as shown in Fig. 3.12. Accordingly, the icing boundary on the upper surface is located at 1.2% of the chord length when the Mach number is 0.033, as shown in Fig. 3.11.

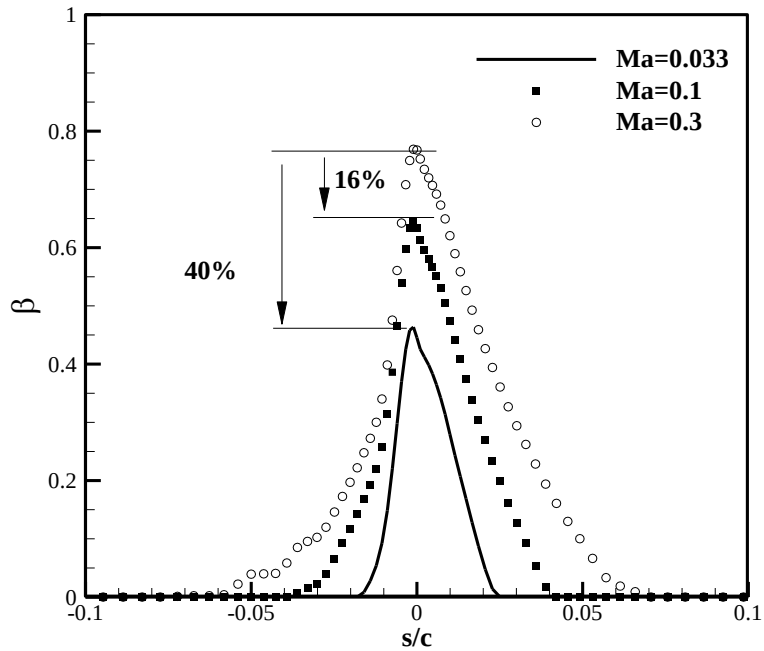

Fig. 3.12 Collection efficiency for the airfoil of HALE aircraft at Mach 0.033, 0.1, and 0.3

The low flight speed also changes the heat transfer characteristics. The heat transfer coefficient of HALE aircraft is much lower than that of conventional high subsonic aircraft. The heat transfer coefficients according to various Mach numbers are compared in Fig. 3.13, along with the heat transfer coefficient of the NASA IRT case using NACA0012 that is illustrated in Fig. 2.19 (b) as an ice horn case. The heat transfer coefficient of NASA IRT case is also calculated by the present numerical code.

Ice horns develop not by the existence of runback alone; rather, the runback must be frozen in regions with high local heat convection. In NASA's IRT case, the local

h_c value usually exceeds 1,000 kW/Km^2, and the runback water is sufficient to form ice horns around the stagnation region. In contrast, the HALE aircraft does not produce sufficient runback water; its heat convection coefficient is gradually distributed over the entire surface; and the peak value of the heat convection coefficient does not exceed 250 kW/Km^2, as shown in Fig. 3.13. Therefore, unfrozen runback water exists on the wing surface in the form of a water film.

The rime ice shape occurring on a low-speed HALE aircraft enables the application of the one-shot method to predict the ice accretion shapes. When the glaze ice shape occurs, the shape of the leading edge changes significantly according to the icing exposure time, and the multi-step method is required to predict the glaze ice shape accurately. However, the ice accretion shapes on the HALE aircraft are similar to the shape of the clean wing. The gradual growth of the ice thickness occurs while maintaining the direction of the ice formation, and no sudden change in the frontal shape appears during the exposure time.

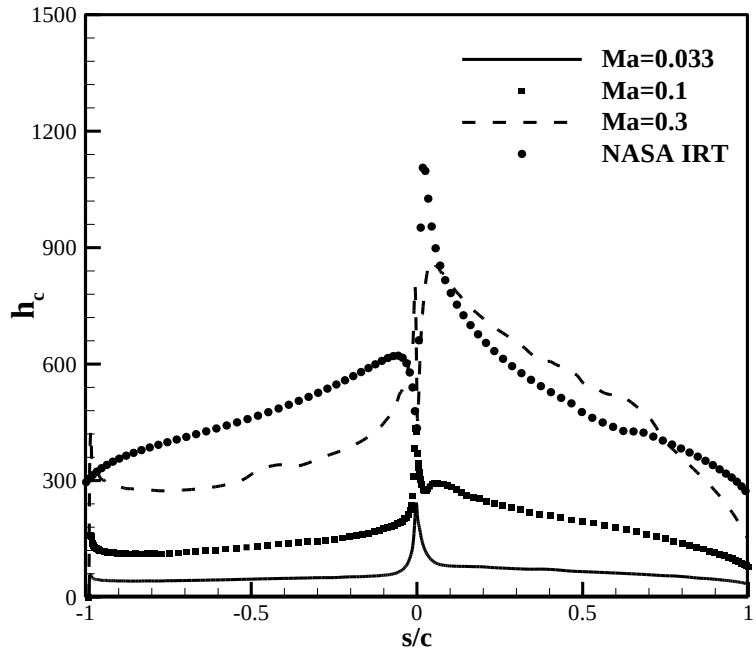

Fig. 3.13 Heat transfer coefficient for the airfoil of HALE aircraft at Mach 0.033, 0.1, and 0.3 and NASA IRT

The bar charts in Fig. 3.14 (a), (c), and (e) depict changes in the total mass of ice, lift, and drag coefficients calculated for the nine conditions. The figures show that the change in total weight of HALE aircraft due to the accumulated ice is negligible. Although ice accretes along the leading edge of the long wingspan, the narrowness of the ice-covered area and its limited maximum thickness, as observed in Fig. 3.7, limit the added weight due to the accreted ice. As can be seen in Fig. 3.11 (a), the total mass of ice is less than 3.5% of the MTOW of a clean HALE aircraft in all cases.

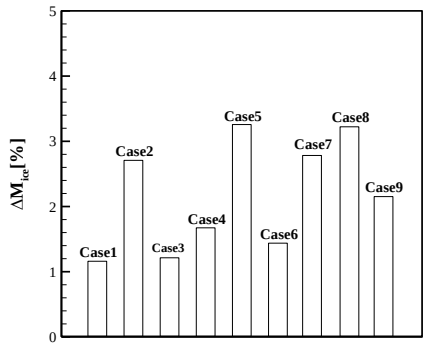

(a) ΔM_{ice} of nine cases

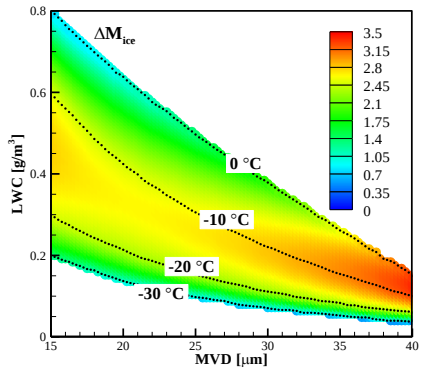

(b) ΔM_{ice} of RSM

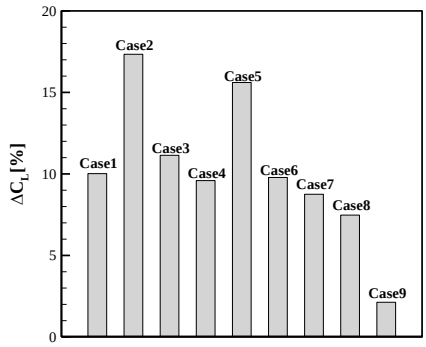

(c) ΔC_L of nine cases

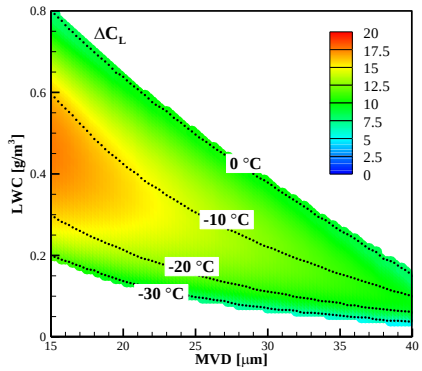

(d) ΔC_L of RSM

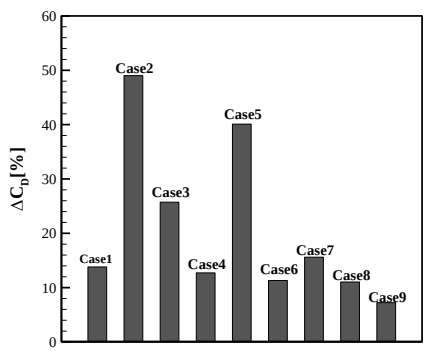

(e) ΔC_D of nine cases

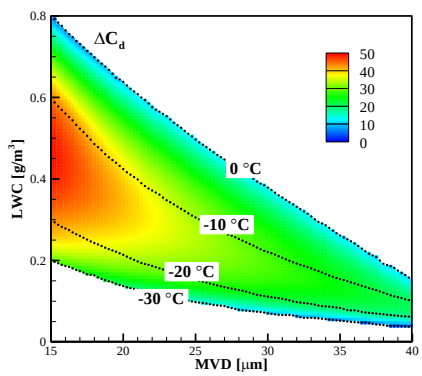

(f) ΔC_D of RSM

Fig. 3.14 ΔM_{ice}, ΔC_L, and ΔC_D results of nine cases and RSM

3.3.2 RSM Results

Fig. 3.14 (b), (d), and (f) illustrate the ΔM_{ice}, ΔC_L, and ΔC_D calculated with respect to MVD and LWC using the constructed RSMs. Thus, the variation in the aerodynamic performance of HALE aircraft due to accumulated ice is clearly shown in a quantitative manner.

The overall tendency of the RSM results follows the results of the nine cases as shown in Fig. 3.14 (a), (c), and (e). The RSM results also show that the tendency of ΔC_L and ΔC_D are different from that of ΔM_{ice}. Furthermore, the RSM results show that the tendencies of the two aerodynamic performance coefficients are similar to each other. Fig. 3.14 (d) and (f) also confirm that the significant decline in the aerodynamic performance corresponds to Cases 2 and 5 in Fig. 3.14 (c) and (e).

The operators can collect meteorological data such as LWC, MVD, and temperature before take-off. However, data gathered using various means can be varied and uncertain, and the probability distribution and range of variation of the meteorological data may not be known. The newly constructed RSM cannot consider such uncertainties in the meteorological data, and therefore a conservative approach is warranted to remain within the limits of the meteorological uncertainty. Using the proposed approach, both aerodynamic performance coefficients show the same tendency, and the degradations in the lift and drag performances are shown to increase in high LWC and low-temperature conditions, as in Fig. 3.14 (d) and (f). Taking a conservative perspective, the maximum LWC value and the minimum temperature value should be used when applying the proposed RSMs.

3.3.3 Analysis of Mission Success or Failure

Fig. 3.15 summarizes the ratio of required power to battery capacity ($W_{req}/W_{battery}$) for the selected icing environment in Section 2. Because the required thrust is proportional to the drag, it is expected that the required power matches qualitatively the drag increase in Fig. 3.14 (f).

In all conditions when icing occurs, the rapid reduction of L/D causes a drastic increase in the required power for the ice accumulated HALE aircraft in comparison to the clean HALE aircraft. The clean HALE aircraft only consumes 60% of its battery capacity to reach the mission altitude; hence, there is a battery margin of 40% at mission altitude. However, the ice-covered HALE aircraft uses at least 80% of its battery capacity. When MVD is over 27.5 μm, regardless of the ambient temperature, only 14% of the battery margin remains. When MVD is below 18 μm, and the ambient temperature is between -10°C and -20°C, more than 90% of the battery is consumed to reach the designated mission altitude, leaving a battery margin of only 10%. Icing on the propeller is not considered in the present study and the propeller efficiency (η_{pro}) is assumed to be 60%, which is the efficiency value of clean propellers. Considering the expected increase in required power, operators should carefully consider the operating conditions that cause the battery margin to be below 10%.

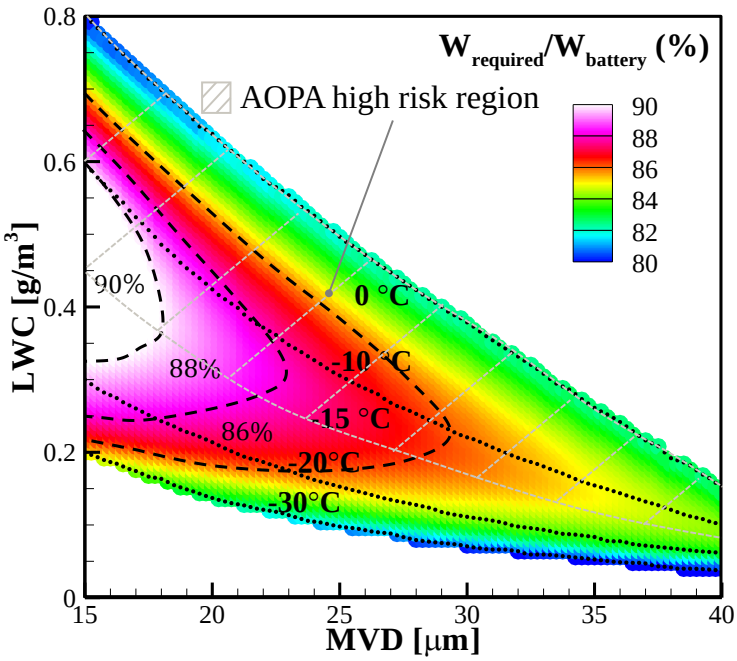

Fig. 3.15 Ratio of required power to battery capacity ($W_{required}/W_{battery}$) for climbing to mission altitude in FAR Part 25 Appendix C conditions

To compare the icing characteristics of transport category airplanes with the low-speed HALE aircraft, the high-risk region due to icing published by the Aircraft Owners and Pilots Association (AOPA) is plotted in Fig. 3.15. The aviation safety risks due to icing suggested by the AOPA with respect to ambient temperature [4] are summarized in Appendix C of the present paper.

For transport category airplanes, which are human-controlled aircraft that usually operate at Mach 0.1 or higher, the ambient temperature is regarded as the single most important parameter for aircraft flight safety with respect to icing. Transport category airplanes usually fly at higher speeds, resulting in a substantial amount of mass of

impinging and runback water even under low LWC, which in turn leads to the development of ice horns. Hence, it is reasonable to judge the flight safety of transport category airplanes based on the ambient temperature only.

In contrast, the maximum ice thickness significantly impairs aerodynamic performance in the HALE aircraft, and meteorological data such as LWC, MVD, and ambient temperature must be collected before launching a HALE aircraft. Therefore, the flight safety and mission success potential should be assessed based on the collected data and the constructed meta-models presented herein. Using the procedure presented in this study, the operator will be supplied with reliable information as to whether or not the mission can be successfully accomplished, establishing the conditions under which the launch should be canceled.

3.3 Summary

In an effort to increase the reliability of HALE aircraft under icing conditions, a novel procedure has been proposed to help determine whether or not the HALE aircraft can perform a given mission based on meteorological data. Toward this objective, the FAR Part 25 Appendix C was selected as the reference icing environment, and ice shapes on a HALE were numerically calculated for EAV-2H+ (MTOW of 20 kg, the mission altitude of 10 km and the wingspan of 11 m). Aerodynamic performance coefficients for the HALE with ice accreted on its surface were then determined, and RSMs were constructed to quantitatively correlate the relationships between the icing environment variables (ambient temperature and

LWC) and the aerodynamic performance degradation in terms of lift, drag, and ice mass. These RSMs were subsequently employed to determine if the HALE aircraft can climb to its mission altitude with its given battery capacity, thereby judging the possibility of mission success under icing conditions. Through a series of computations, the following conclusions are drawn.

1) Because of the low flight speed of a HALE aircraft, only a small number of water droplets adhere to its surface, and there is a low convective heat transfer, which tends to rime ice shapes even under the glaze ice temperature conditions (above -14.15 °C) that hold for transport category airplanes.

2) Using the procedures suggested in this study, a battery margin of 40% remains when the clean baseline HALE aircraft, EVA-2H+, reaches the mission altitude. However, when ice accumulates on the HALE aircraft, the battery margin falls below 20% under FAR Part 25 Appendix C conditions. In particular, when the LWC lies between 0.3 and 0.6 g/m³, the temperature is between -10 to -20°C, and the MVD is less than 18 μm, the battery margin decreases even further, below 10%. It is well-known that temperatures above -15°C are hazardous for transport category airplanes because of the occurrence of glaze ice. However, the severe icing condition for the HALE aircraft was found to be different. Hence, special attention is required when attempting to operate the HALE aircraft in these meteorological conditions.

3) Because of the characteristics of the rime ice shape, the one-shot method can be applied to obtain reasonably accurate ice accretion shapes. In addition, lift and

drag vary almost linearly over time as the ice thickness grows because the rime ice shapes on HALE aircraft are similar to the leading edge shape of the clean wing.

4) In order to ensure the numerical accuracy of the one-shot method, the computed ice shapes and resulting aerodynamic coefficients were systematically compared with those from the multi-step method. The results of the validation indicate that the density and flight speed should be taken midway (3.35 km) between the ground and the designated altitude (6.7 km); at the midpoint, the lift and drag coefficients show a difference of less than 3% compared to those determined with the multi-step method.

4. Helicopter Fuselage Icing

In this chapter, the ice accretion on the helicopter fuselage under the rotor-wake effects is systematically investigated. In order to check the validity of the previous studies which have been performed to the isolated fuselage like fixed-wing aircraft, the rotor inflow effects were examined by comparing the ice-accretion shapes with and without the rotor wake effects.

Next, the variation of the ice-accretion shape is also discussed with respect to the methods, actuator disk model and actuator surface model, for including the rotor-wake effects. The necessity of the accurate solver should be evaluated by comparing both results.

Finally, the variation of ice-accretion shapes was reviewed with respect to the advance ratio including hovering, low (μ=0.075) and high (μ=0.15, and μ=0.20) forward flight.

4.1 Rotor-Wake Effect

In this section, the effects of the rotor wake on the ice shapes are investigated in detail. To this end, ice-accretion analyses for forward flights both with and without the rotor effects were performed. Computations were performed with the same condition for the validation of the helicopter fuselage as shown in Table 2.4. The same grid system used for the flow-field analysis was employed.

First, the rotor-wake effects on the ice accretion were investigated so that the ice-accretion analyses are performed with and without the rotor system above the

fuselage. As mentioned previously, the flow-field analysis using rhoPimpleFOAM which is described in Section 2 was performed for isolated fuselage case. After that, the droplet-trajectory analysis, thermodynamic analysis, and grid regeneration were carried out.

In ASM, each rotor blade is treated as a source term in the momentum equations. The actual rotor blade geometries were not considered, so the ice accretion on the blade is not taken into account. The ice accretion on the rotor blades leads to a change in the rotor trim angle and the resultant inflow distribution on the rotor disk, which again influences the ice accretion on the helicopter fuselage. With this limitation in mind, the present study focuses on ice accretion on the helicopter fuselage under wake effects.

The computation was performed under unsteady assumptions for ASM. The time step was set such that the rotor rotates by an azimuth angle of 1° per iteration. To suppress the numerical instability due to impulsive starting, in this study, the slow-starting method proposed by Chung and Lee was applied [70]. The rotor tip speed increased in a gradual manner during the first rotor revolution.

The icing time is 30 min., which is a relatively long time compared to the time required for ten rotor revolutions. After ten rotor revolutions, a full periodicity was obtained in the rotor inflow. The droplet trajectory was attained, and thermodynamic analysis was performed based on the averaged velocity field during the last revolution.

A comparison of the collection efficiency on the fuselage both with and without the rotor system is shown in Fig. 4.1. Fig. 4.1 (a) shows the fuselage without rotor effects and Fig. 4.1 (b) shows the collection efficiency with ASM. To directly compare the collection efficiency of both cases, the collection efficiency is non-dimensionalized by the rotor tip speed of ASM, not forward-speed.

Without the rotor-wake effects, the fuselage in forward flight has a large collection efficiency on the engine inlet and front part of the fuselage. The collection efficiencies on the fuselage with respect to different inflow models show similar trends to Fig. 4.1 (a). However, the maximum collection efficiency is significantly lower than that without rotor effects. Water droplets were observed to be accreted on the windshields because of the rotor inflow.

The resultant ice-accretion shapes are compared in Fig. 4.1 (c) without rotor effects, and in Fig. 4.1 (d) with ASM. In Fig. 4.1 (c), it is clearly shown that as expected, there was significant ice accretion on the nose region of the fuselage and engine inlet. On the other hand, there is practically no ice accretion along the sidewall of the fuselage, whose attitude is parallel to the freestream. Even in Fig. 4.1 (c), ice accretion on the engine inlet and nose of the fuselage is clear. However, under the rotor-wake effects, the windshield region is fully covered with ice due to the modification of the droplet trajectories in the presence of the rotor downwash. The sidewalls of the fuselage did not undergo any change in the outer shape, and only the surface roughness changed slightly for both cases.

For the rotor-absent condition, the total weight of ice accreted on the fuselage amounts to 68.0g, whereas for the rotor-present condition, the total ice weight amounts to 56.8 g for ASM as shown in Fig. 4.2. In the presence of the rotor effects, it is expected that the droplets will be distributed, and accordingly, more ice will be accreted on the fuselage because of the wake effects. However, the resultant ice weight of the rotor-present conditions is estimated to be 16.5% smaller.

In Fig. 4.2, the mass distribution from each case (with and without rotor-wake effects) are seen to overlap, which enables thicker ice to appear on the fuselage. It is easily seen that the thicker ice was accumulated on the fuselage nose, windshield and engine inlet regions in both cases. Although the fuselage is located under the rotor inflow, less ice is accumulated on the overall fuselage in the rotor-fuselage interaction case compared to isolated fuselage case. The explanation for this is given as follows.

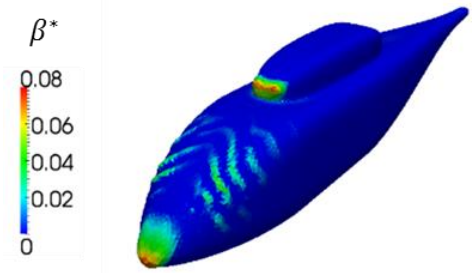

(a) Non-dimensionalized collection efficiency of fuselage only

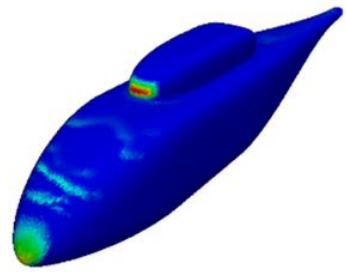

(a) Non-dimensionalized collection efficiency of ASM

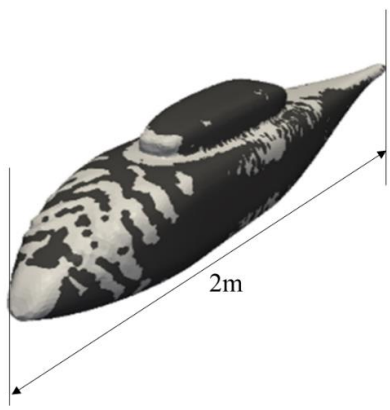

(c) Ice accretion shape of fuselage only

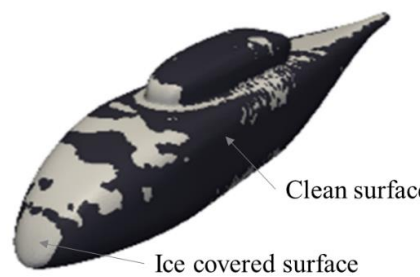

(d) Ice accretion shape of ASM

Fig. 4.1 Non-dimensionalized collection efficiency by rotor tip speed and Ice-accretion shapes at LWC = 0.6 g/m³, MVD = 20 μm, T = -10 °C, 30 min, μ = 0.15.

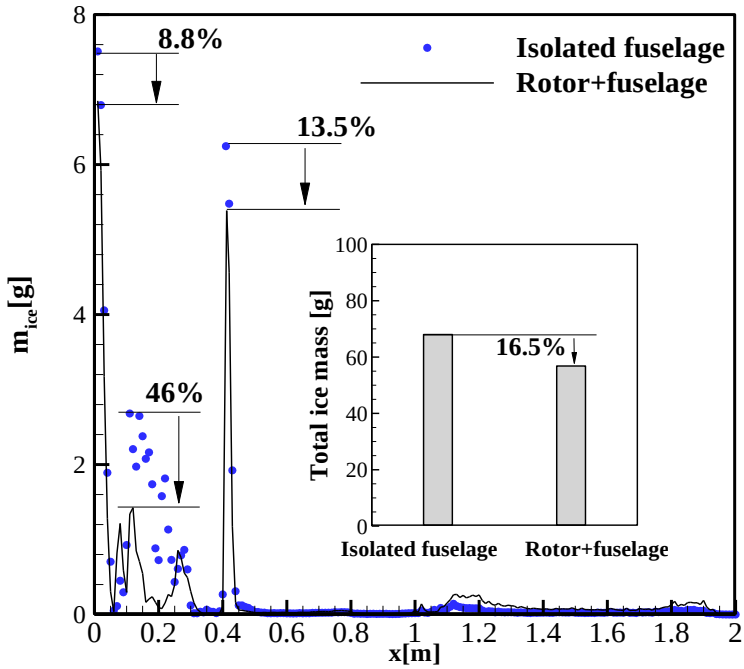

Fig. 4.2 Mass distribution along the longitudinal direction, LWC = 0.6 g/m³, MVD = 20 μm, T = -10°C, 30min, μ = 0.15.

Fig. 4.3 shows the sectional pressure and velocity magnitude contours along the center of the fuselage (y = 0). In the absence of the rotor effects (a), there is a stagnation point at the nose of the fuselage. Flow is rapidly accelerated to recover the speed from the stagnation to windshield before reaching to the engine inlet. The situation is very different for the cases in the presence of the rotor-wake effects. Because of the thrust on the rotor disk, there exists a high-pressure region under the rotor disk and a lower-pressure region above the rotor disk. The high-pressure region under the rotor disk affects the upper surface of the fuselage. As seen in Fig. 4.3, the

flow is slowed down between the rotor disk and the fuselage, which is smaller than the freestream velocity of 27 m/s.

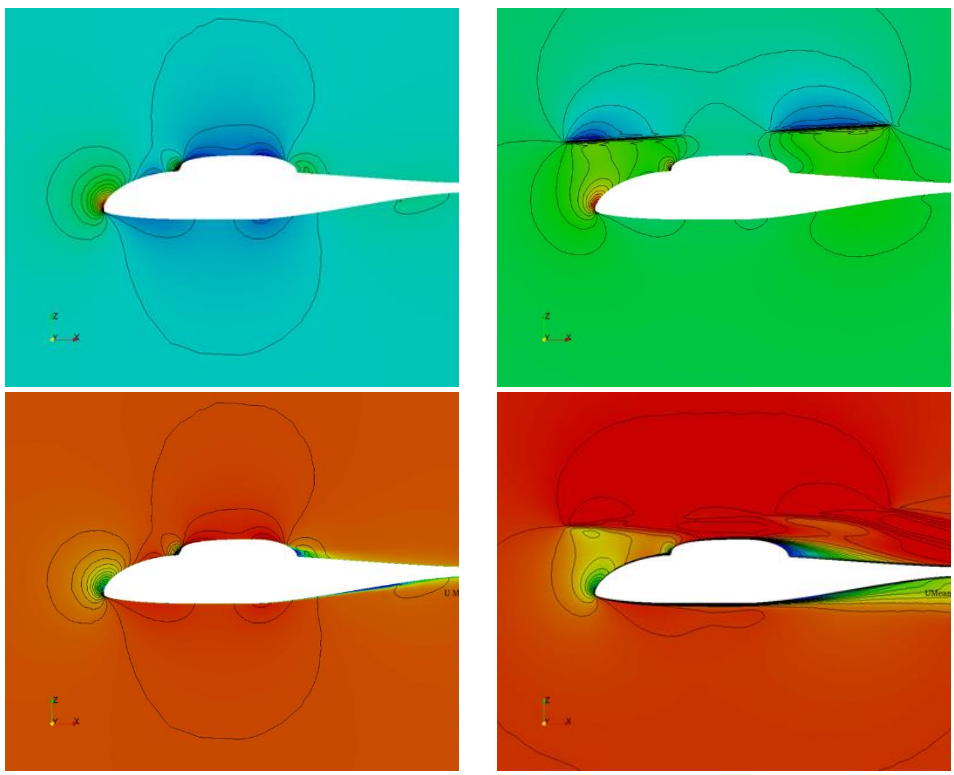

(a) Fuselage only **(b) ASM**

Fig. 4.3 Averaged pressure coefficient(top) and velocity(bottom) contour for 1 rotor revolution in LWC = 0.6 g/m³, MVD = 20 μm, T = -10 °C, 30 min, μ = 0.15.

As shown in Eq. (2-15), the drag on the droplet is proportional to the relative velocity between the freestream and the droplet. Accordingly, the drag tends to decrease in the region where the relative velocity decreases. If the drag on the droplet is zero, the droplet trajectory coincides with the streamline of the freestream. In

summary, as the relative velocity between the droplet and freestream decreases, the drag on the droplet also decreases. Hence, the droplets tend to avoid the surface without colliding with the surface, resulting in a substantial reduction of the collection efficiency.

The ice-accretion shapes and the effects of the rotor-fuselage interaction vary according to the icing parameters and forward-flight speed. The effects of LWC, MVD, ambient temperature, and forward-flight speed were analyzed, and the effect of these parameters was discussed.

The droplet inertia is the similarity parameter for the droplet behavior, as shown in Eq. (3-14). As the droplet diameter (MVD), decreases, the droplet-inertia parameter also declines exponentially. A small droplet is sensitive to the change of the flow field. The droplet path lines become like a streamline of flow fields. It means that the rotor inflow effect is important in small droplet size. Therefore, the difference in the ice-accretion shapes between the isolated fuselage case and the rotor-fuselage interaction case will increase for cases with small droplets. Further, the droplet-inertia parameter decreases as the forward-flight speed decreases. Besides, the area that is directly exposed to the rotor wake is increased as the wake-skew angle decreases in low-speed forward-flight conditions. It is important to consider the rotor-wake effects for conditions involving low-speed forward flight and a small droplet size. For a similar reason, the droplet-inertia parameter decreases as the forward-flight speed decreases. Further, the area that is directly exposed to the rotor wake is increased as the wake-skew angle decreases in low-speed forward-

flight conditions. Consequently, it is important to consider the rotor-wake effects for conditions involving low-speed forward flight.

The mass of the impinging water is linearly proportional to LWC. The ambient temperature determines the mass of freezing ice. However, LWC and the ambient temperature do not affect the droplet trajectories. The difference in the ice-accretion shapes between the isolated fuselage case and the rotor-fuselage interaction case is caused by the change in the droplet trajectories. It is expected that a lot of ice will be accumulated in the case of the rotor-fuselage interaction compared to that of the isolated fuselage, regardless of the LWC and the ambient temperature.

In this study, scale-size fuselage icing analysis was performed. As the test case, ROBIN from the NASA Langley Research Center was chosen because it provides a good database of information for validating the airflow solution. There is a requirement to apply the results of this study on the full-scale model. However, form the Eq. (3-14), the general tendency of the full-scale fuselage condition can be expected. In actual-size fuselage condition, the droplet-inertia parameter is inversely proportional to the scale factor. If the other parameters are identical to model helicopter conditions, the droplet inertia parameter of the full-scale helicopter is smaller than that of the model helicopter. Since the low inertia of droplets is sensitive to the rotor inflow, the differences of the total mass and its distribution between the isolated fuselage case and rotor-fuselage interaction case would increase. Therefore, the need for icing analysis, including the rotor wake, is more important for the full-scale fuselage.

4.2 Comparison of ADM and ASM

In this section, the difference between the ice-accretion shapes obtained by ADM and ASM was analyzed. Computations were performed with the same condition for the validation of the helicopter fuselage as shown in Table 2.4 except for the advance ratio of 0.075 (V_∞= 14.27 m/s).

(a) Actuator disk model **(b) ASM**

Fig. 4.4 Ice-accretions shapes, μ = 0.075, C_T = 0.0064, T = -10 °C, LWC = 0.6 g/m³, MVD = 20 μm, 30min.

As shown in Fig. 4.4, both ADM and ASM resulted in ice accretion on the nose section, windshield, the front side of the engine, the upper side of the cowl, and the tail boom; the positions of ice accretion were the same for both methods. However, there was a difference of 16% in the mass of ice accretions. Compared to ADM, ASM predicted a larger amount of ice accretion. ADM predicted ice accretion of 45.4 g, while ASM predicted 52.7 g. Fig. 4.5 shows the mass distribution of ice

accretions along the longitudinal direction of the fuselage. There is a large difference in the mass of accreted ice at the collision between the wake and fuselage, where x is greater than 1.5 relative to the nose sections and engine-intake sections.

0

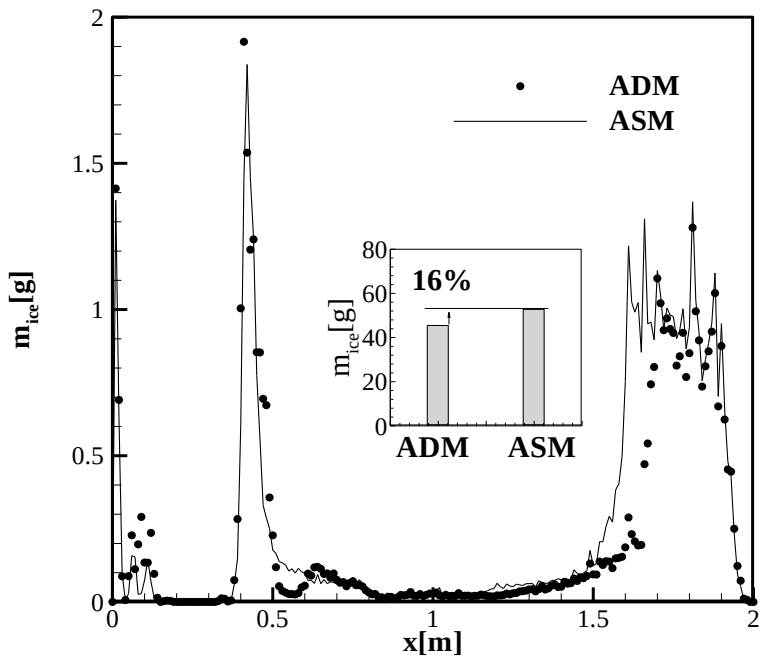

Fig. 4.5 Mass distribution along the longitudinal direction, and total ice mass; μ = 0.075, C_T = 0.0064, T = -10 °C, LWC = 0.6 g/m^3, MVD = 20 μm, 30min.

To visualize the flow structure, here the Q-criterion (Q), as described by Dubief and Delcayre [71] is used for the visualization of vortices:

$$Q = 1/2\left(\Omega_{ij}\Omega_{ij} - S_{ij}S_{ij}\right) \quad (4\text{-}1)$$

The meaning of Q is very intuitive: areas where Q > 0 indicate that the rotation rate $\Omega^2 = \Omega_{ij}\Omega_{ij}$ is higher than the strain rate, $S^2 = S_{ij}S_{ij}$, where $\Omega_{ij} = (u_{i,j} - u_{j,i})/2$ and $S_{ij} = (u_{i,j} + u_{j,i})/2$ are the antisymmetric and symmetric components of ∇u.

Fig. 4.6 shows the iso-surface at Q = 1000 using ASM and ADM. Fig. 4.6 (a) illustrates the instance Q when the blades are at 0°, 90°, 180°, and 270° azimuth angle using ASM. Fig. 4.6 (b), and (c) mean the averaged iso-surface at Q = 1000 for 1 rev. by using ASM and ADM respectively. As shown in Fig. 4.6 (a), the instance result of ASM is able to give a more precise prediction of the trailed vortex at inboard. However, regardless of rotor analysis methods and the averaging of the flow fields, the wake-skew angles differed by 1° as shown in Fig. 4.6 (a), (b) and (c). In addition, the trailed vortices are vanished by averaging for one rev in the result of ASM (Fig. 4.6 (b)). Although the averaged result of ASM is similar to the result of ADM, the position and strength of vortices in the wake which has dominant effects on the velocity and droplet fields are different at the tail boom region.

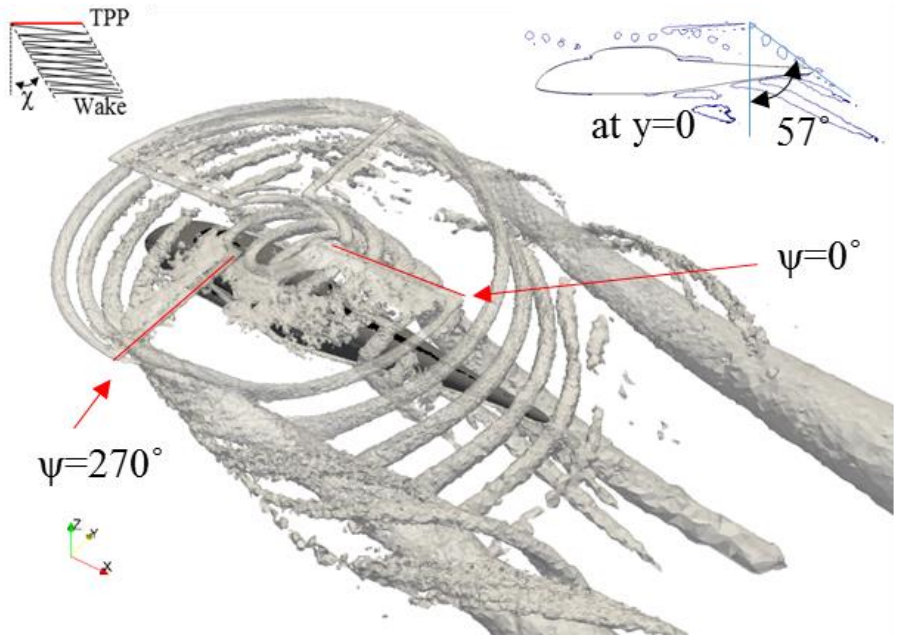

(a) The instance iso-surface at Q = 1000 using ASM

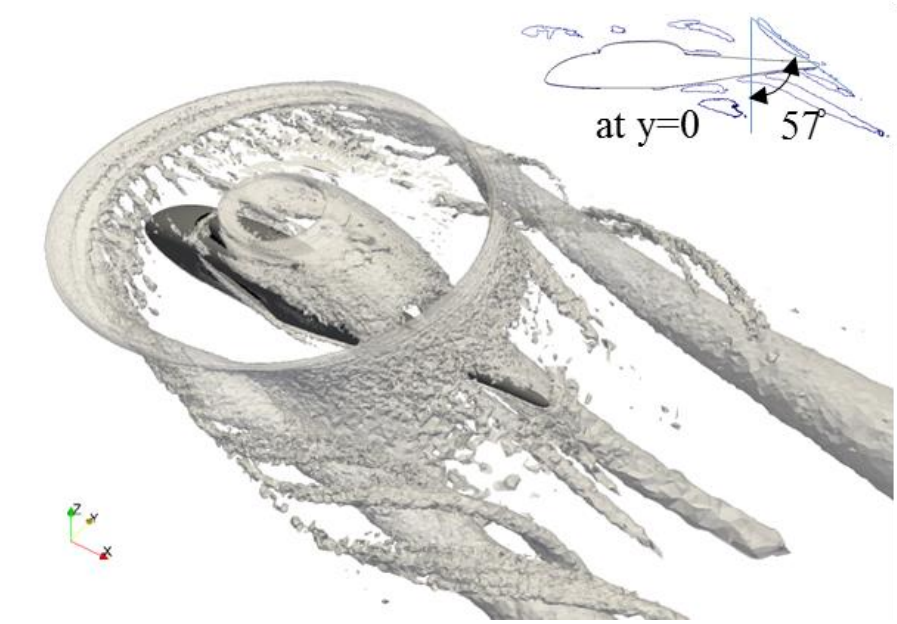

(b) The averaged iso-surface at Q = 1000 for 1 rev. using ASM

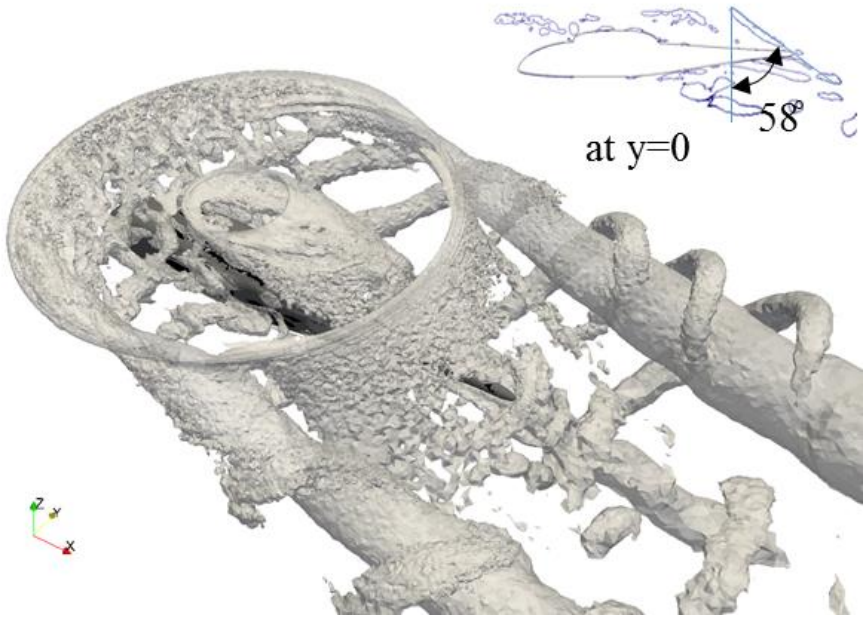

(c) The averaged iso-surface at Q = 1000 for 1 rev. using ADM

Fig. 4.6 Q-Criterion (Q = 1000); μ = 0.075, C_T = 0.0064.

To compare the details about the effects on the droplet fields by the position and strength of vortices in the wake, the velocity and droplet fields are illustrated in Fig. 4.7. Fig. 4.7 (a), (b), and (c) show the velocity contour of the airfield. The instance velocity field using ASM has illustrated velocity in Fig. 4.7 (a) and the averaged velocity field for one rev. using ASM, and ADM are plotted in Fig. 4.7 (b) and (c), respectively. The velocity contours of droplet field are also plotted in Fig. 4.7 (d), and (e). Fig. 4.7 (d), and (e) are obtained from averaged velocity fields using ASM, and ADM, respectively. The instance droplet field is not plotted because the droplet field was calculated based on the averaged velocity field.

As shown in Fig. 4.7 (b) and (c), compared to ADM, averaged ASM predicted a higher inflow with a larger area at the rear of the rotor hub. As shown in Fig. 4.7 (a), the blades periodically generate the strong tip vortices, and the tip vortices descend near the tail boom without dissipation resulting high induce velocity. These results have an effect on the averaged velocity field of ASM. Because of this, the higher droplet field velocity whose direction is perpendicular to the fuselage surface was predicted. Non-zero region of vertical component of droplet velocity is located from x = 1.3 to x = 2.0 in ASM as shown in Fig. 4.7 (d). However, in case of ADM plotted in Fig. 4.7 (e), the region is observed after x = 1.5. In summary, averaged ASM predicted a higher droplet field velocity and wider area at the tail boom region compared to ADM. Thus, ASM predicted higher collection efficiency and total ice mass compared to ADM.

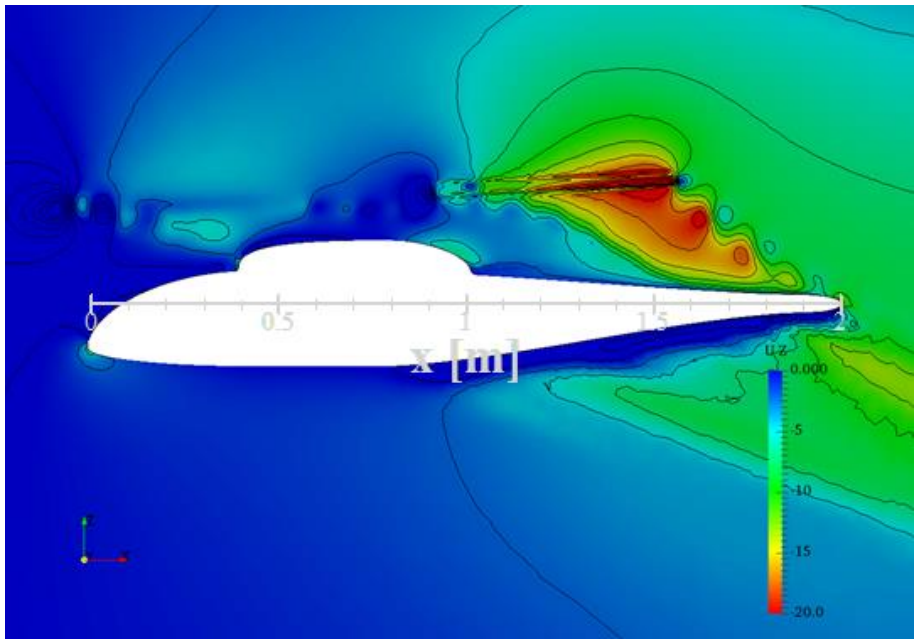

(a) Instance velocity field with the blades at 0° using ASM

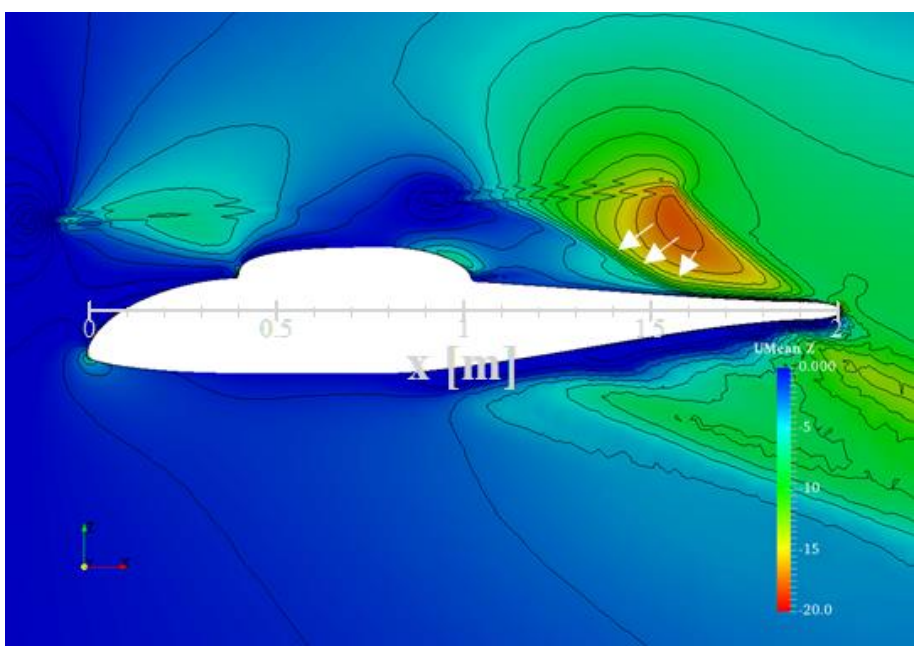

(b) Averaged velocity field using ASM

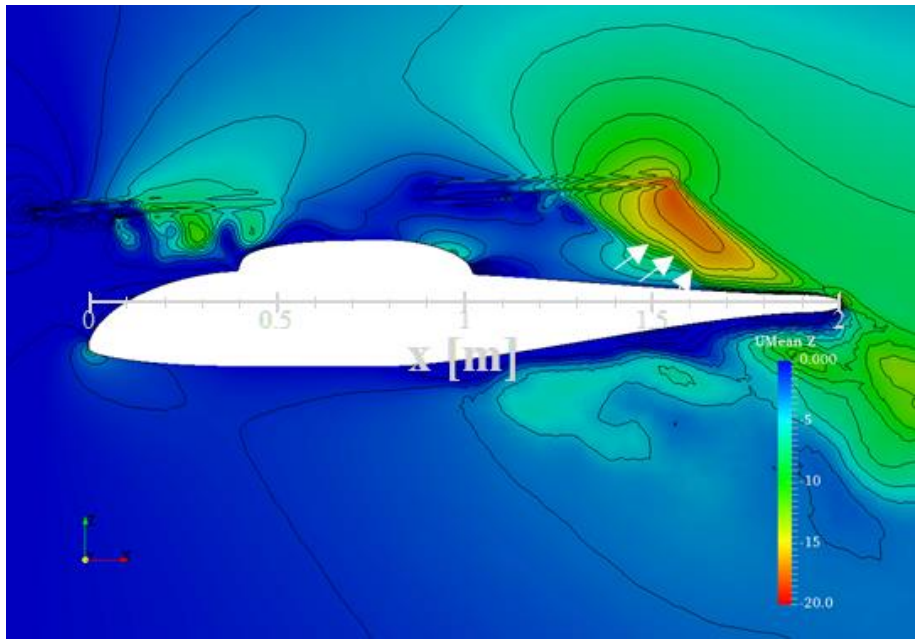

(c) Averaged velocity field using ADM

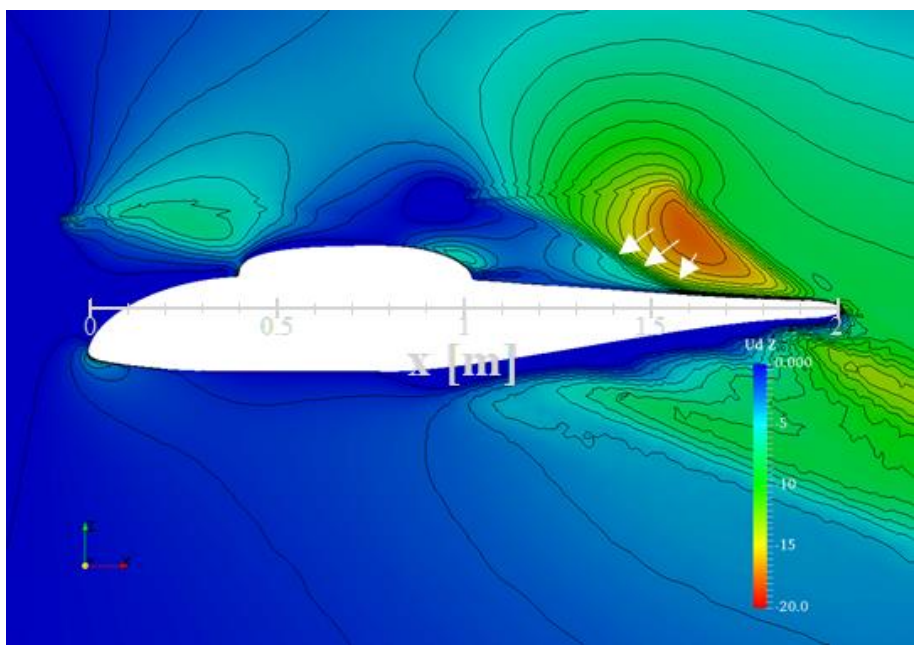

(d) Averaged droplet field using ASM

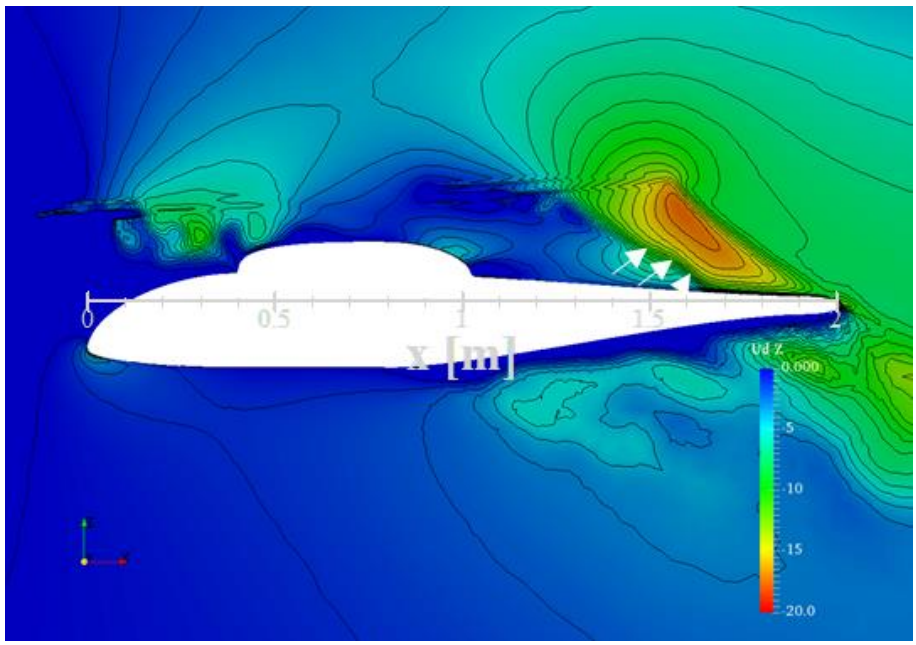

(e) Averaged droplet field using ADM

Fig. 4.7 Velocity contour of droplet and airfields in the z-direction (inflow direction), μ = 0.075, C_T = 0.0064.

In low-speed flight, where rotor-wake interaction occurs at the tail boom region, the total ice mass and distribution of ice accretion are different depending on the rotor analysis methods that are used. Although the velocity field was averaged for one rev. in ASM, the information of velocity field that includes the periodic generation of strong tip vortices and the collision to the surface is delivered to the droplet and thermodynamic model. Even when one rev. averaged flow fields with a long time exposure are used, two analysis models resulted in different ice shape, the total ice mass, and the distribution of ice accretion.

To obtain a more precise prediction of the shape of ice accretion, the discrete positions and the strengths of the tip vortices should be considered because they

affect the flow fields and droplet fields. In particular, when the tip vortex collides with the fuselage, or when it is even near the fuselage, the velocity of the droplet fields increases, causing more ice accretion. Thus, it is imperative to find and employ a model that can accurately predict the strengths and positions of the tip vortex with respect to the analysis of ice accretion.

With respect to the nose-up pitching moment caused by ice accretion, ASM had a computed result of 1.85×10^{-4} Nm, while ADM had a corresponding value of 1.32×10^{-4} Nm. This is the same as when the rotor's hub that thrusts with $C_T = 0.0064$ moves towards the tail section by 2.1×10^{-6} m. This value is not significant enough to require a change in the trim angles. However, depending on the rotor analysis methods employed, there may be a large difference in the nose-up pitching moment. Between x = 1.5 and x = 1.8, there is a significant difference in the ice distribution. That is longer moment arm region from the hub (x = 0.69) compared to fuselage nose and engine intake. Therefore, the difference of the nose-up pitching moment is up to 40%.

4.3 Variation of Ice-accretion Shape with Respect to Advance Ratio

With the increased advance ratio, the rotor wake was inclined backward because of the forward speed. Given the same thrust, the wake-skew angle increased with respect to the freestream velocity. Accordingly, the degree of the fuselage that is exposed to the wake effects decreases. Hence, the advance ratio – helicopter forward-

flight speed – is a crucial factor, which determines the rotor-wake effects on the fuselage.

To investigate the effects of the rotor wake on the ice-accretion shape on the fuselage, a series of numerical computations were performed with respect to various advance ratios; μ = 0.0 (hovering), μ = 0.075, 0.15, and 0.20 with the same meteorological condition for the validation of the helicopter fuselage as shown in Table 2.4.

In the previous study in Ref. [43], the surface roughness was set to 0.5 mm regardless of the ambient temperature and freestream velocity. However, the surface roughness is actually given as a function of ambient temperature, freestream velocity, MVD, and LWC. NASA LEWICE provided an empirical relation [12], which correlates the surface roughness with respect to the aforementioned parameters. Based on the empirical relation of NASA LEWICE, the surface roughness values were set to 1.72 mm, 1.51 mm, 1.7 mm, and 1.83 mm for advance ratios of 0 (hovering), 0.075, 0.15, and 0.20, respectively.

4.3.1 Collection efficiency and ice-accretion shapes

Fig. 4.8 shows the collection efficiency and ice-accretion shapes in hovering and when the advance ratio is 0.075, 0.15, and 0.2. As shown in Eq. 4, the collection efficiency is a dimensionless value that is determined by the freestream velocity. To compare the collection efficiencies regardless of the advance ratio, this study was

designed by setting the flight speed as the tip velocity instead of the freestream velocity, regardless of the advance ratio.

The ice-mass distribution and the position of the highest collection efficiency differ as the forward speed changes, which results in ice accretion. In hovering, there is no ice accretion at the nose due to no forward speed, but there is greater ice growth on the upper pylon. As the forward speed increases, a higher collection efficiency is expected at the nose and the front side of the engine intake. Ice accretion was shown at the nose and on the front side of the windshield.

To show the mass distribution of ice accretion more clearly, the longitudinal distribution of ice mass is depicted in the Fig. 4.9. In hovering, ice accretion occurred because of the inflow of the rotor, as mentioned before. It occurred between the rotor hub section and the rotor's tip section.

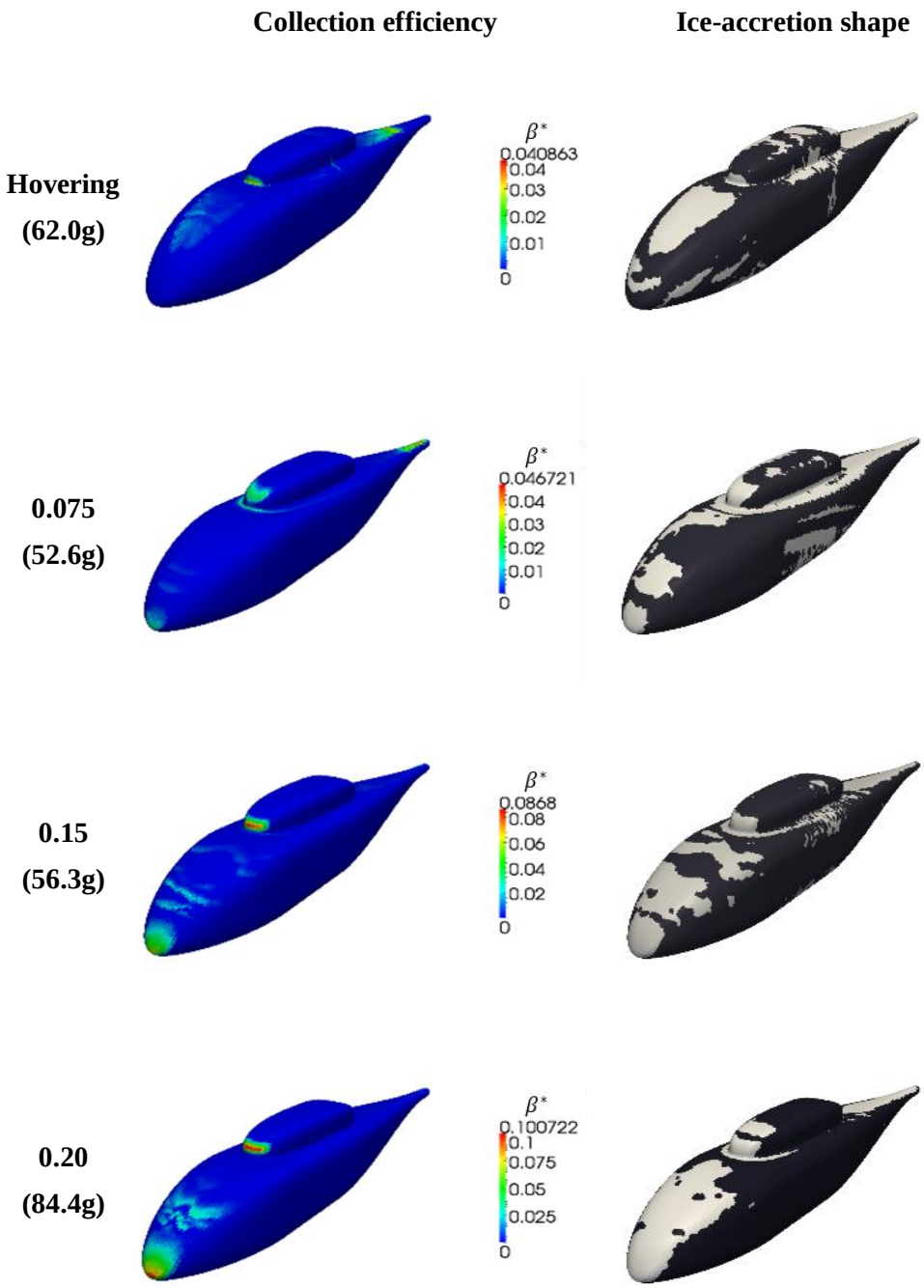

Fig. 4.8 Collection efficiency of non-dimensionalized rotor tip speed and ice-accretion shapes with various advance ratios by ASM.

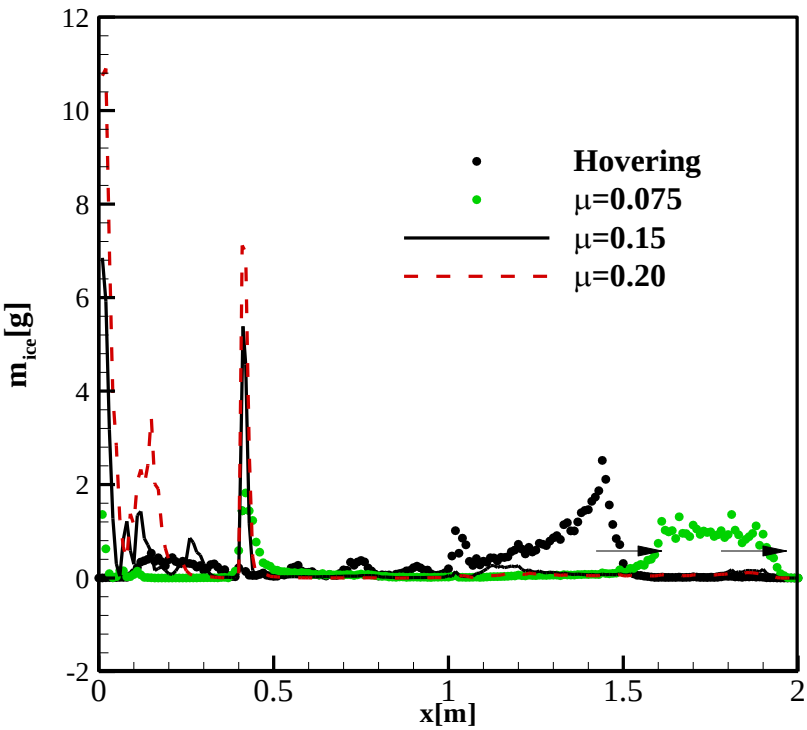

Fig. 4.9 Longitudinal ice-mass distribution with various forward speeds.

4.3.2 Hovering

As shown in Fig. 4.10, the significant ice is accumulated on not the fuselage nose, but the tail boom region (x = 1.0 ~ 1.5). In hovering, the tip vortex collides directly with the fuselage at the tail-boom as well as the nose. The massive ice accretion on the tail boom region is consistently described; the massive accretion of ice takes place in the region where the tip vortex collides with fuselage surface. However, the tip vortex collides with fuselage nose; the amount of ice on the nose region is noticeably less than that of tail boom region. To understand this unexpected

phenomenon, z-direction of the droplet velocity is illustrated in Fig. 4.10. The velocity of the droplet is accelerated after it passes the rotor surface. The velocity of droplet reaches about 20 m/s (forward speed is 28 m/s at an advance ratio of 0.15) both the tail boom and the nose region. On the tail boom region, the velocity vector of the droplet has opposite direction to the outward normal vector of the fuselage surface. In contrast, the velocity vector of the droplet is perpendicular to the outward normal vector of the fuselage surface on the fuselage nose region. The droplets dodge the fuselage nose without collision. Therefore, more ice accretion occurs at the tail boom compared to the nose section. It is hereby confirmed that the substantial ice accretion appears on the collision region between the fuselage surface and the tip vortex, and the droplet velocity vector should be perpendicular to the outward normal surface vector.

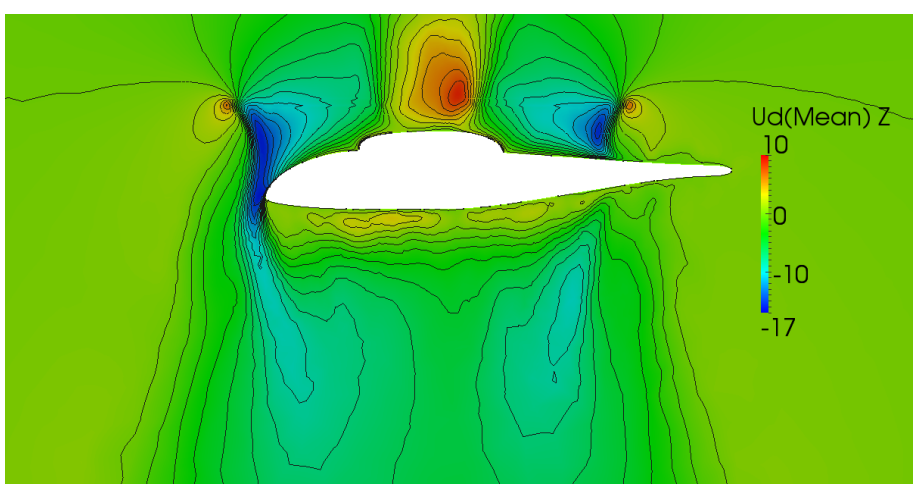

Fig. 4.10 The z-direction (inflow direction) droplet velocity contour in hovering.

Fig. 4.11 shows the total ice mass. As shown in this figure, more ice accretion occurs at hovering than at an advance ratio of 0.15. It can be seen that in hovering, the most ice accretion occurs in the large area of the upper side of the fuselage. The area of the upper side is four times larger than the area of the frontal side. In addition, the collision velocity of the droplets at the fuselage surface is 60% of the forward flight speed at an advance ratio of 0.15. Thus, the total ice mass of hovering is 9.1% higher than that of forward flight speed at an advance ratio of 0.15.

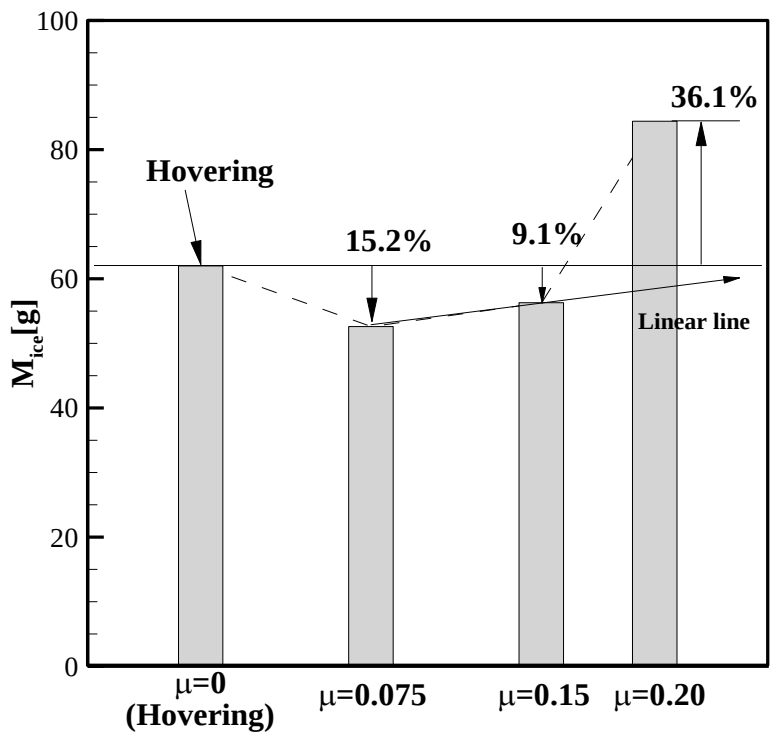

Fig. 4.11 Total ice mass with various forward speeds.

4.3.3 Low forward flight speed ($\mu = 0.075$)

The distinguishing phenomenon occurring at low forward flight speed ($\mu=0.075$) is that many droplets collide at the end of the tail-boom section. At a slow speed, the inertia of the droplets is small and is more affected by the amount of inflow. As shown in Fig. 4.12 (a), droplets move towards the inflow at a distance that is greater than 46% of the radius from the rotor. The velocity of the droplets accelerates as they pass the rotor and collide with the end of the fuselage at high speed. Therefore, the collection efficiency is the greatest at the end of the fuselage.

At an advance ratio of 0.075, asymmetric ice accretion occurs in front of the engine intake under conditions of different forward speeds. Ice accretion occurred at the front side rather than at the backside. As the wing tip vortex occurring at the rotor's leading edge descends, it collides with the fuselage, as shown in Fig. 4.12 (b) and (c). Because the rotor rotates counter-clockwise, the front side (right side) of the vortex collides with the fuselage. Thus, in front of the engine intake, ice accretion adapts an asymmetric shape.

In addition, for an advance ratio of 0.075, unique patterns are seen on the side of the fuselage as shown in Fig. 4.13. A vortex is produced due to the flow separation on the side of the fuselage, and as the vortex descends because of the inflow, it moves along the side of the fuselage as shown in Fig. 4.12 (c). This vortex then ends up colliding with the fuselage. In the separation region near the fuselage surface, the low value of the liquid water contents and droplet velocity are developed. Accordingly, the negligible value of collection efficiency is calculated in the flow

separation region. Consequently, the empty region of ice is formed at the side of the fuselage. Because the direction of the vortex movement is close to the skew angle, ice accretion in the shape of the skew angle occurs on the side.

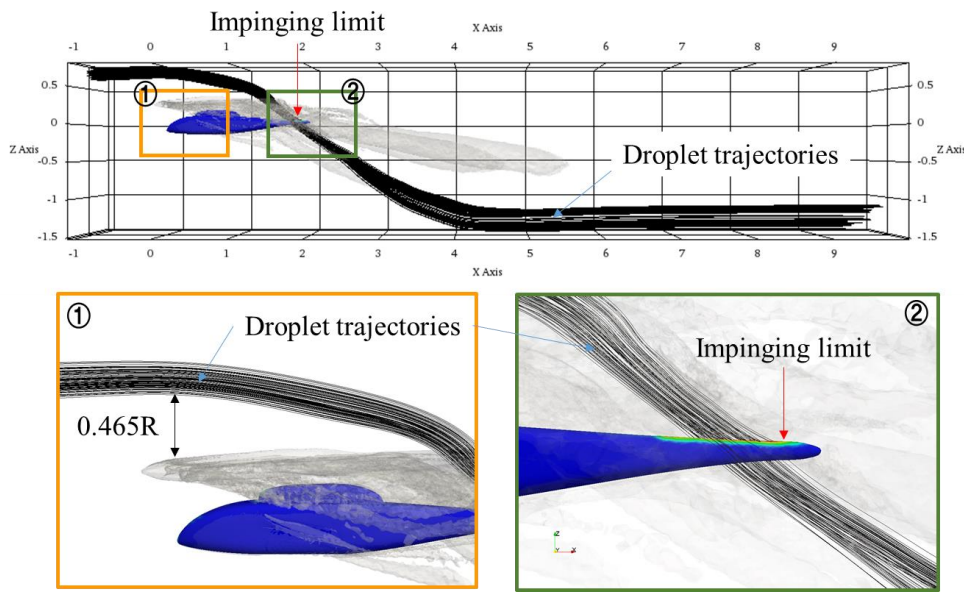

(a) The iso-surface contours of Q = 1000 and droplet trajectories in tail boom region at μ = 0.075

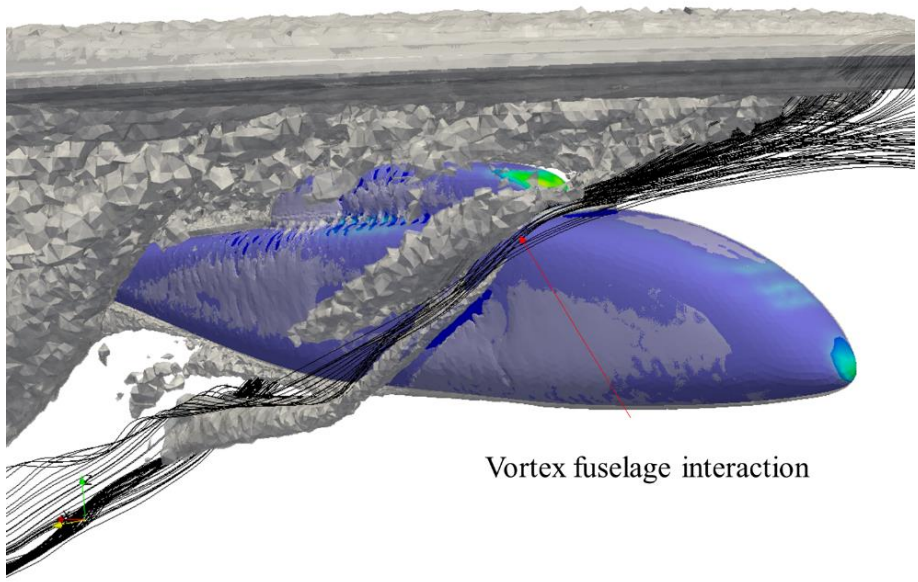

(b) The iso-surface contours of Q = 1000 and droplet trajectories in engine intake region at μ = 0.075

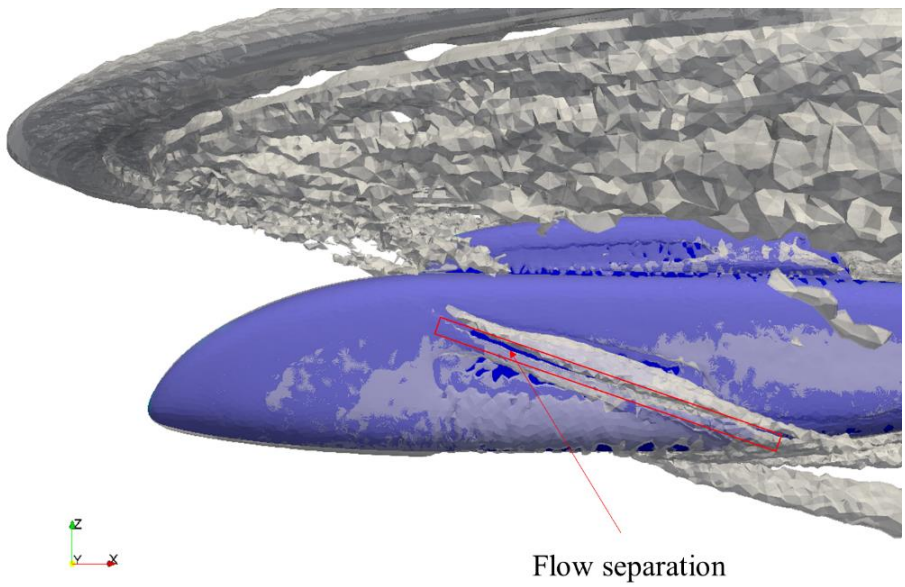

(c) The iso-surface contours of Q = 1000

Fig. 4.12 Particle trajectories and Q-Criterion at μ = 0.075 by ASM.

Fig. 4.13 Ice-accretion shape of fuselage side at μ = 0.075 of ASM.

4.3.4 High forward flight speed (μ = 0.15 and 0.20)

For advance ratios of 0.15 and 0.20 with high speed, the same characteristics of flow and ice accretion are shown. Because of the high forward speed, ice accretion occurs more frequently at the front. As shown in Fig. 4.14 (a) and Fig. 4.15 (a), the wake does not collide with the tail boom of the fuselage, and it merely flows towards the backside. For an advance ratio of 0.075, droplets on the surface of the rotor were accreted at the tail-boom section. However, when the forward speed is high, they do not collide with the fuselage after the hub region. The front side of the fuselage, engine intake, and windshield section had more droplets and ice accretion as shown in Fig. 4.14 (b), and Fig. 4.15 (b). When hovering and for an advance ratio of 0.075, more ice accretion occurred on the side. However, when the forward speed was high, no ice accretion was observed on the side of the fuselage because the total vector of the inflow and the forward speed is almost parallel to the forward speed. In addition,

the low value of the z-direction velocity for droplet field is observed near the tail boom region as shown in Fig. 4.14 (d), and Fig. 4.15 (d).

For advance ratios of 0.15 and 0.20, although the distributions of ice accretion at the nose and windshield sections are almost the same, there is a big difference in the mass of ice accretion. As shown in Fig. 4.11, even when the forward speed was increased by 33%, the ice mass increased by about 50%. As the speed increases, the droplet inertia also increases, and droplets collide at high speed with the fuselage in a linear trajectory. Therefore, as the forward speed increases, the collection efficiency and the thickness of ice increase on the front side. Then, as the forward speed grows from 0.075 to 0.15 and then to 0.2, the total mass of ice exponentially increases. This indicates that as the speed increases, there is more accretion on the frontal fuselage.

At low forward speed and in hovering, ice accretion occurred mostly at the tail boom. As the forward speed increased, ice accretion usually occurred at the windshield, nose of the fuselage, and engine intake. Such positions require a careful attention with respect to ice accretion. For example, when there is ice accretion on the windshield, it may be threatening to flight safety as it may block the pilot’s view. Most helicopters have windshields with defogging and defrosting capabilities, which are enabled using thin conductive film in the laminate or hot air [72].

The faster the forward speed, the more careful attention is required for pilots' vision. With respect to the nose of the fuselage, if there is a severe ice accretion due to the presence of the radome, the communication link may be lost. In reality, this

has already occurred in several cases. There are plans for most aircraft to be installed with anti-icing equipment near the radome sections, and there is the need for new anti-icing designs, considering the mass of ice accretion that is present at the highest forward speed.

Ice accretion at the engine intake can cause serious problems. First, the ice at the engine intake decrease the flow rate of air entering the engine. Second, the flow separation is induced by the ice at the intake lips. These can degrade the performance of the compressors of helicopters that use turboshaft engines. Third, ice accretion by foreign object damage (FOD) screen can cause engine failure. In addition, long-term exposure under icing conditions can cause the ice shedding. When the shaded ice crashes the extremely thin blades of turboshaft engine, it also lead to engine failure.

In this study, as the forward speed increases, more ice accretion occurs at the engine intake because the shape of the engine intake is perpendicular to the direction of flow. Thus, by controlling the direction of intake considering the inflow and forward speed, any risks that are caused by ice accretion can be minimized.

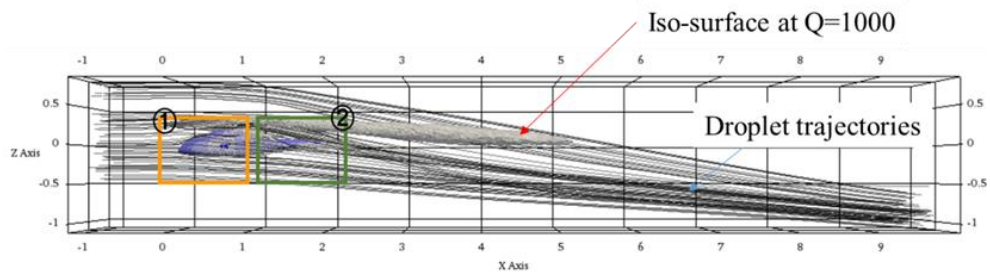

(a) Side view of μ = 0.15

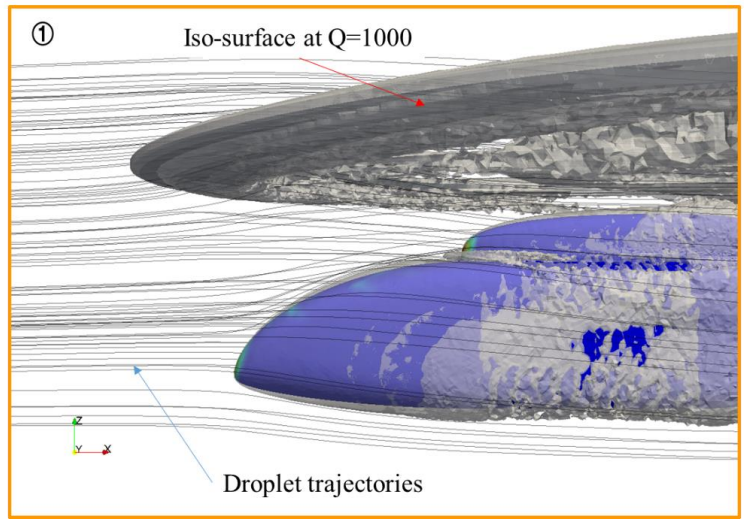

(b) Side view of μ = 0.15 with droplet trajectories

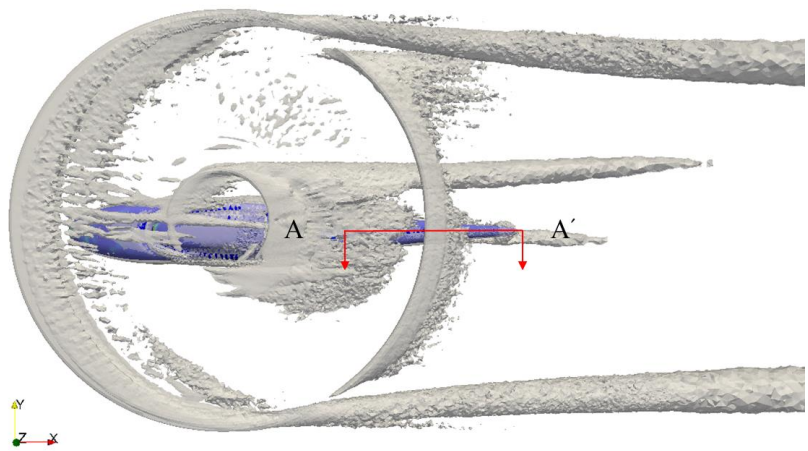

(c) Top view

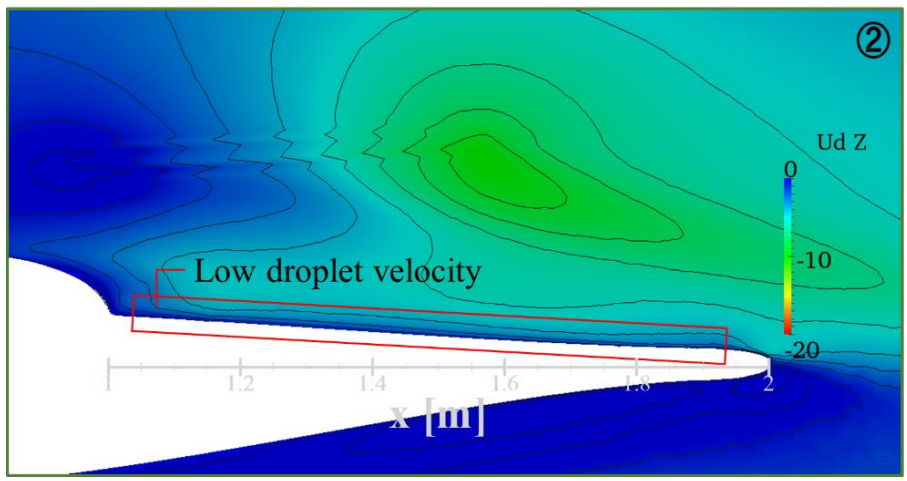

(d) Droplet z-direction velocity contour of μ = 0.15 at the fuselage center plane (AA' plane)

Fig. 4.14 The iso-surface contours of the Q-criteria (Q = 1000) and droplet trajectories at μ = 0.15

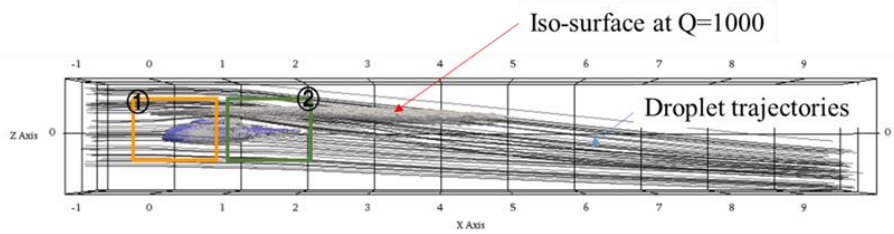

(a) Side view of μ = 0.20

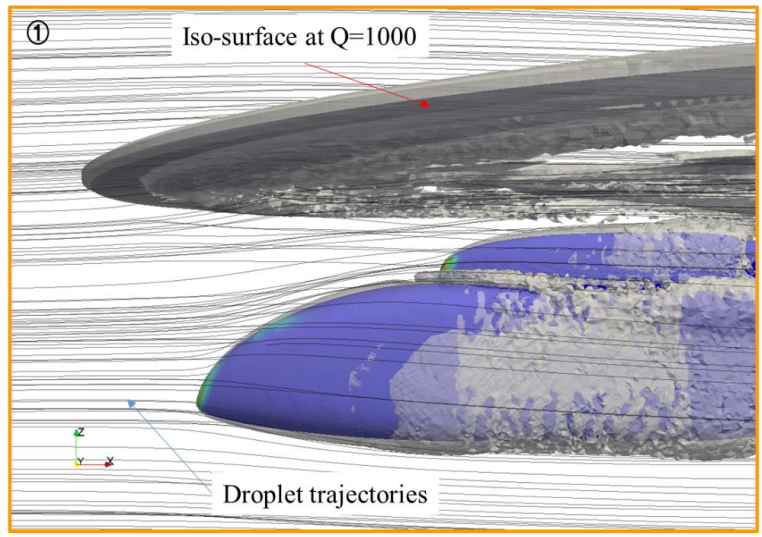

(b) Side view of μ = 0.20 with droplet trajectories

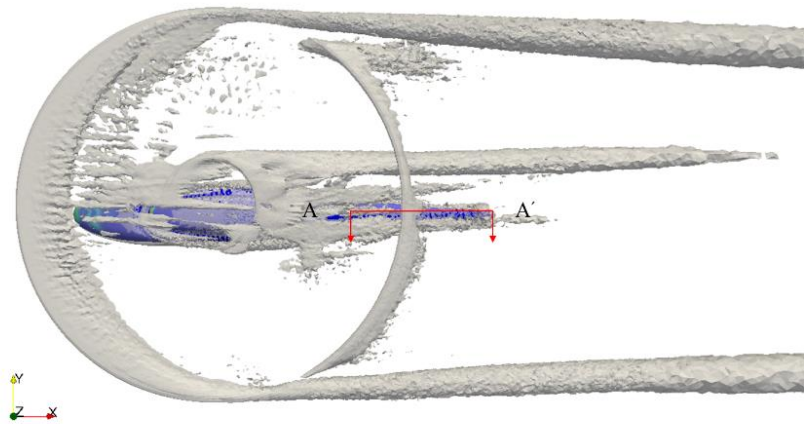

(c) Top view

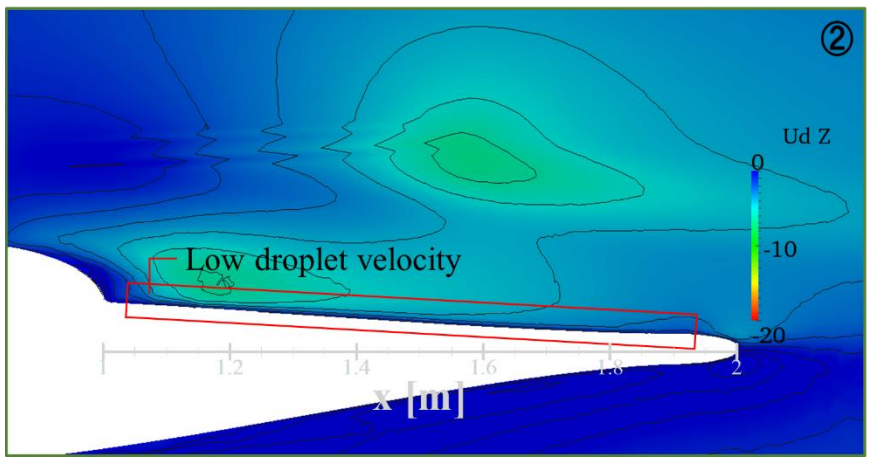

(d) Droplet z-direction velocity contour of μ = 0.20 at the fuselage center plane (AA' plane)

Fig. 4.15 The iso-surface contours of the Q-criteria (Q = 1000) and droplet trajectories at μ = 0.2

4.4 Summary

In the present study, an up-to-date numerical analysis program was developed for 3D ice-accretion shapes and applied it was applied to accurately predict the ice shape on the helicopter fuselage. To include the rotor-wake effects, the latest actuator surface method and actuator disk method were used to compare the resulting ice shapes. The droplet trajectories based on the Eulerian approach were calculated, enabling the collection efficiency in the regions of flow separation to be determined. For the thermodynamic analysis, the thin-water film mode was introduced.

It is expected that the wake behavior and the resultant ice shapes on the fuselage will be changed by the ice accumulated rotor blades. However, the ice accretion of the rotor blades is not taken into account by limiting the validity of the actuator surface and disk method. Within the limitation of the methodology, following studies

are conducted. First, ice shapes on the fuselage both with and without helicopter rotors were compared to investigate the rotor-wake effects on the ice accretion. Second, the ice shapes on the helicopter fuselage obtained by actuator disk model and actuator surface model were examined to compare the effects of rotor modeling methodology. Lastly, to analyze the effects of forward flight speed, ice shapes are compared with the various advance ratio (hovering, 0.075, 0.15, and 0.2).

Consequently, some interesting results were obtained.

1) Initially, because of the rotor inflow, more ice accretion was expected to accrete on the upper surface of the fuselage in the rotor-fuselage interaction case compared to the isolated fuselage case. However, the total mass of ice accreted on the fuselage under the rotor effects is smaller than that without rotor effects. The reason for this is that the drag on the droplet decreases because of the high-pressure region between the rotor disk and upper surface of the fuselage, resulting in a reduction of the collection efficiency. Because the change in the droplet trajectories determines the ice-accretion shape, it is essential to consider the rotor-wake effects for conditions of low-speed forward flight, small droplet size, and full-scale helicopter. The LWC and ambient temperature are not relevant icing parameters that played a significant role in changing droplet trajectories.

2) There is a slight variation in the ice shape with respect to the numerical methods considered for the rotor wake – actuator disk model and actuator surface model. The changes in the collection efficiency and the ice-accretion shape because of the flow and droplet fields were discussed; these changes are caused by the

strengths and positions of the tip vortex and inboard sheet. In particular, at the site of the collision between the tip vortex and fuselage, severe ice accretion was observed. Therefore, ice-accretion shapes can be accurately predicted when the vortex-fuselage interaction effects are taken into consideration. Actuator surface model, which models a discrete vortex, can predict the mass and distribution of ice accretion more accurately than actuator disk model, which is standardized by one disk side.

3) There is a strong dependency on the location and the quantity of ice accretion on the helicopter forward flight speed. Especially, mass ice accretion occurs on the regions of the collision between the tip vortex and the fuselage surface. As expected, for hovering and low forward flights (advance ratio = 0.075), most of the ice accretion occurs on the tail boom. On the other hand, as the forward flight speed increases up to advance ratios of 0.15 and 0.20, the distribution of the ice accretion becomes similar to that of rotor-absent conditions. Ice accumulated on the fuselage nose, windshield, and engine intake regions. Due to the large collision area with high speed of droplets, 15.2 and 9.1% much ice is accumulated in hovering case than that of forward flight case with the advance ratio 0.075 and 0.15, respectively. However, as the forward speed grows from 0.075 to 0.15 and then to 0.2, the total mass of ice exponentially increases. Thirty six percent more ice is accumulated in the advance ratio 0.2 than that of hovering case.

5. Conclusions and Future Works

5.1 Conclusions

Ice Shape Estimation and Performance Analysis Code (ISEPAC), a simulation program to analyze icing phenomena occurring on the 3D body, is developed by applying the latest numerical technique. ISEPAC is a second-generation icing analysis tool that is based on the Navier-Stoke equations, Eulerian droplet field calculation, and Messinger model with a shallow water film. ISEPAC can handle not only for the fixed-wing aircraft but also for the helicopter fuselage. The latest actuator surface model loaded on ISEPAC is able to capture the behavior of individual blade tip vortices. Since ISEPAC is loaded on the sing platform, there is no additional program to transfer and control the data among the individual modules. By using ISEPAC, the icing characteristics of HALE aircraft and helicopter fuselage are analyzed. As a result, the following conclusions were drawn.

First, there are no ice horns on HALE aircraft and helicopter fuselages with low-speed flight (Mach number less than 0.1). The droplet with small inertia can avoid the body without collision, resulting in a small amount of water film on the surface. The generated water film flows by the shear force of the air and concentrates on a specific region. At this time, the heat transfer is predicted to be small due to the low-speed characteristic, and the concentrated water film is not frozen. Therefore, the ice horn cannot be observed.

Second, a new procedure is proposed to determine whether an aircraft can be operated at the given icing environment for HALE aircraft which does not have anti-/de- icing devices due to the ultra-light design. Preferentially, the ice shapes and its aerodynamic performance change are obtained from ground to the mission altitude in the climbing stage under the given icing conditions. Then, the quantitative relation between aerodynamic performance coefficients and icing environment variables was established. It was possible to judge the success of the mission by comparing the required power and the mounted battery to reach the mission altitude. The fixed-wing aircraft with high-speed is known to generate ice horns at high temperatures; thereby the risk increases at high temperatures. However, ice horns cannot be observed under the stratiform clouds for HALE aircraft. Since there is no ice horn, the high-risk region of HALE aircraft is different from that of fixed-wing aircraft. The high-risk region of icing for HALE aircraft appears under high humidity and low-temperature conditions.

Third, because of the characteristics of the rime ice shape for HALE aircraft under low-speed, the one-shot method can yield accurate ice accretion shapes and its aerodynamic performance. This study suggests the reference altitude for the one-shot method. The suggested altitude for the density and flight speed is mid-altitude (3.35 km) which is between the maximum cloud altitude (6.7 km) and the ground. The validity of the one-shot method was confirmed by comparing both results obtained by the multi-step method and one-shot method. To set the reference altitude, this study evaluates the ice shapes and its aerodynamic performance obtained from both

mid-altitude and maximum cloud altitude. At the midpoint, the ice accretion shapes of mid-altitude were quantitatively and qualitatively similar to the results of the multi-step method. Moreover, the lift and drag coefficients show a difference of less than 3% compared to those determined with the multi-step method, at the midpoint.

Forth, when analyzing the icing on the body of the helicopter, accurate flow analysis should be accompanied. A relatively high-pressure and low-velocity region is formed under the rotor and above the fuselage. That region is located in the front part of the fuselage. Low-velocity region induces different droplet trajectories and heat transfer rate. Consequently, the differences of the total amount of ice and the ice distribution are clearly distinguished between the isolated fuselage and including rotor wake effect. In addition, since a large amount of icing occurs in the area where the tip vortex collides the body, it is necessary to apply a numerical code that can accurately predict the strength and position of the individual tip vortex.

Fifth, when design the anti-/de-icing devices for the helicopter fuselage, all ranges of flight-speed including hovering should be considered. According to the forward flight speed of helicopter, the significant differences can be observed in the amount of ice and its distribution on the helicopter fuselage. Since the fuselage is fully exposed under the rotor wake for hovering and low forward flights (advance ratio = 0.075), most of the ice accretion occurs on the upper surface of the fuselage. In particular, the massive ice is accumulated on the tail boom because of the collision between blade tip vortex and fuselage. On the other hand, at high forward flights (advance ratio = 0.15 and 0.2) the most ice is accreted in the frontal area such as

fuselage nose, windshield, engine intake. As the forward flight speed increases up to advance ratios of 0.15 and 0.20, the total amount of ice tends to increase dramatically, and the greatest amount of ice is recorded at the fastest speed. Especially, the severe ice can be observed in the fuselage nose and engine intake. As a result, the required power for the anti-/de-icing devices should be prepared for the highest flight speeds, and proper power distribution should be considered dependent on the flight speed.

5.2 Future Works

5.2.1 Helicopter blade icing

The developed simulation code should be modified to predict the ice accretion shapes on the helicopter rotor blades. Since this study is based on actuator surface method, the real rotor blades were substituted for numerical source terms. To overcome the inherent limitation, the aerodynamic module and droplet field module should take into account the actual blade and its rotation. The momentum equations of the thermodynamic module should be added the centrifugal force, which acts on the water film.

Even if each module is prepared for the rotor blade analysis, another problem remains. It is impossible to apply the steady state assumption. However, the quasi-steady assumption is widely used for the icing simulation codes. The helicopter changes its pitch angle periodically to compensate for the lift imbalance that occurs on the advance and retreating side forward flight. Because the blades rotate more than 200 times per one minute, the sectional and azimuthal changes occur in a very

short time. The icing analysis tool under the quasi-steady assumption has difficulty in unsteady characteristics.

Because there is no change in azimuthal direction hovering condition, BET can be applied to predict ice accretion shape under quasi-steady assumption. Narducci et al. [73] suggests a procedure to predict the ice accretion shapes on the rotor blades in hovering condition. Narducci calculated the airfield using the OVERFLOW which is based on the Computational Fluid Dynamics (CFD) and Computational Structural Dynamics (CSD) coupling solver in hovering condition, and then he extracted the effective angle of attack at each sectional location. From the obtained effective angle of attack, the sectional ice accretion shape is calculated by using the LEWICE based on BET.

Recently, a few studies have been conducted to predict the ice accretion shapes on the blades for forward flight conditions. Narducci et al. [74] extended the concept of hovering to forward flight. He applied very crude assumption. First, the ranges of pitch angles at each sectional location are calculated by using the OVERFLOW. Second, high-frequency pitching motion is ignored. Instead, he calculates the range of effective angle of attack and divides the range into four sections. The total icing exposer time was also divided into four according to the four sections. Third, from the given four effective angle of attacks, the ice accretion shapes were calculated and updated.

Later, Xi, C. et al. [75] improved the Narducci's approach. They used the hybrid method as an aerodynamic solver, which is coupled with N-S solver near the blades

and free-wake method in the far field. The droplet field also calculated using the Eulerian approach using the same grid system with the N-S solver. The centrifugal force is added to the water film model. Using the developed solver, they calculated the 3D ice accretion shapes every 15 degrees azimuthal interval. However, it has limitations to the long-term exposer time under icing condition. Though the hybrid method is relatively advanced technique, the method cannot simultaneously consider both rotors and fuselage.

Although various studies have been carried out for the flow analysis of helicopters, icing research for the helicopter blades is rarely performed. It deals only with the method how to divide the exposure time without physical background. The efficient algorithm should be developed based on the physical phenomenon with accurate modules including rotor aerodynamics and thermodynamic modules. Moreover, the helicopter icing tool should be considered both rotors and fuselage.

5.2.2 Surface roughness model

Since the latent heat released by the phase transition of the water into ice is balanced off by the heat convection, thus the prediction of the heat convection rate is an important factor in calculating the amount and the shape of ice accurately. The experimental studies have proven that the convective heat transfer is strongly affected by the surface roughness [76]. Therefore, the accurate prediction of surface roughness is important to the final ice accretion shapes for the icing simulations.

The actual surface roughness is not determined as a single value but has various distributions. Because the water film is frozen to ice, it appears smooth at the stagnation region. In the region away from the stagnation point, the collided droplets on the surface immediately freeze because of the high heat transfer rate. At this time, air pockets are formed, and the very rough surface appears. Until now, the physical model for the surface roughness is hardly known because of lack of the physical phenomenon. There have been some recent attempts, but there are still a lot of unclear areas.

Modeling of the surface roughness due to ice accretion has been studied since the 90's. The LEWICE tried the empirical correlation obtained by parametric studies from experimental results [77]. The surface roughness values can be estimated a function of velocity, temperature, and LWC. However, this simple modeling involves several problems. First, the empirical approach does not simulate the roughness distribution, but single value. Second, since it is correlated by using limited cases of experimental results, the range of applicable variables such as velocity, temperature, and LWC is also restricted. For those reasons, it is necessary to apply the physical roughness model, which can model the physical characteristics of the iced surface rather than the empirical correlation.

The experimental observations discover the facts that the surface roughness is in a transient state, and the surface state can be categorized by ice bead, water rivulet, and film. At this time, surface tension plays an important role to determine the surface state.

Fortin et al. [78] included the surface tension to describe the behavior of the water film on the surface, and they suggested criteria which can define the surface state at each location. Their analytical model also treats the unsteadiness of the surface roughness. However, the suggested model is based on the 2D and it has other unknown parameters to experimentally identify.

Croce et al. [79] improved the surface roughness model suggested by Fortin et al. [78] based on PDE. They extend the roughness model can handle the distribution of surface roughness for 3D arbitrarily bodies. However, they used the other unknown parameter named unsteady parameter, because the solver adopts the quasi-steady state assumption. Therefore, it has limitation to explain the initial state of the surface.

Although there were various attempts to model the distribution of surface roughness, the ambiguity still remains. The suggested roughness models should be validated under various icing conditions. To improve the accuracy of icing simulation codes, the physics-based model without the arbitrariness of empirical parameters should be developed urgently.

6. Appendix

6.1 Improved Actuator Surface Method

6.1.1 Extension to Handle Rotor

To incorporate the effects of the rotor in the CFD analysis, the grid should be generated to match the shape of the rotor blades and should be rotated in the computational domain to calculate the thrust. However, this CFD calculation requires a considerable amount of computational resources to process the numerous nodes in the grid system and to rotate the grid. One practical solution to overcome such difficulties in the CFD analysis is the use of the actuator surface model. This imports the aerodynamic effects of the rotor in a simpler way, through the import of the blade element model to the CFD algorithm, instead of directly calculating the rotor in the same CFD analysis.

This research provides the local aerodynamic coefficients using the blade element model, calculates the time-marching thrust on the blade cell, and embeds the thrust value as a source term into the momentum equation to account for the rotor effects in the CFD analysis. Fig. 6.1 illustrates the two methods that handle the boundary conditions and the additional source terms that have been referenced earlier in the introduction. First, when the pressure value is added to the boundary condition, the value is applied to the border of the adjacent cells. Second, if the source term is added, its value is added to the cells that have been designated as the rotor blade cells. In this study, adding a source term is based on a technique introduced previously by Réthoré and Sørensen [80]. Here, the numerical wiggle correction method is

employed in the developed solver, as reported previously [80]. According to this study, this numerical wiggle causes the disturbance on the relative velocity calculation in the BEM. Thus, the wiggle correction technique is adopted from a previous study. The cells that yield the source term are selected at each time step. The selected cells, called the actuator surfaces, represent the blade surfaces on the rotor disk at the specific iteration time. The actuator surfaces are set to have the same area as those of the real rotor blades.

The algorithm for the rotor analysis and the actuator surface model is shown in Fig. 6.2. The rotor analysis tool maintains the basic formation of the PIMPLE algorithm, introduced previously. Furthermore, it executes an extra process for momentum analysis to account for the effects of the rotor.

To incorporate the rotor effects on the momentum equation, the general incompressible momentum equation is modified in accordance to Eq. (2-2). The added source term is determined from the calculated thrust for the computed volume of the rotor disk, and it becomes zero for other computed volumes. In this way, the source term in the computation causes a pressure jump at the computation cells.

As the solver conducts an analysis of the momentum equation, the added source term represents force. To incorporate this, the local thrust obtained from the blade element model, as discussed in the following section, is transformed into terms of force per unit volume.

6.1.2 Blade Element Method

The BEM can calculate the air load quite efficiently at each generated cell volume, by dividing the rotor disk in azimuthal and radial directions. However, as the BEM does not account for viscous/unsteady phenomena, such as the dynamic stall, it requires additional modeling. For the wind turbine analysis, the BEM is sufficient because the unsteady effect is assumed negligible for analyzing the wind turbine performance under a normal operational state.

Fig. 6.3 shows the aerodynamic forces acting on a blade element. Here, α is the effective angle of attack and γ is the sectional pitch angle at the blade. The relative velocity acting on the element can be drawn in the figure, as determined by Eq. (6-1). Using Eq. (6-2), the local effective angle of attack, α, is calculated to find the aerodynamic coefficients c_l, c_d, and c_m for each element. The aerodynamic coefficients are derived using a table look-up from the aerodynamic performance tables, where the aerodynamic coefficients for the given local effective angles of attack are determined using the following equation:

$$V_{rel} = \sqrt{{V_z}^2 + (\omega r - V_\theta)^2} \tag{6-1}$$

To apply the forces from the rotor to the cells representing the imaginary blades, the thrust should be calculated for each cell using the local aerodynamic coefficients obtained based on the BEM. For a rotor with twist, the pitch angle should be adjusted

by the amount of the twist angle. Application of the angle of attack, based on Eq. (6-1), leads to the local induction angle of attack as shown in Eq. (6-2):

$$\varphi = \tan^{-1}\left(\frac{V_z}{\omega r - V_\theta}\right) \tag{6-2}$$

The local aerodynamic coefficients for each cell are determined at the angle of attack calculated above. The local thrust at each cell is calculated through a combination of the local lift and drag. This study used the BEM to estimate the local thrust on an unstructured mesh, as shown in Eq. (2-7).

The local thrust obtained above can now be applied to the CFD code with a proper transformation for the momentum equation. If the source term is added to the general momentum equation, the thrust has to be modified in the form of force per unit cell volume.

6.1.3 Improved Actuator Surface Model

As mentioned in Part 2.1.1, the BEM requires the induced velocity due to the tip vortex and wake to calculate the effective angle of attack, and thus the aerodynamic coefficients. In the present study, the improved method introduced eliminates the numerical ambiguity that existed in obtaining the induced velocities. The main concept of the present approach is shown schematically in Fig. 2.3. The symbol Γ in Fig. 2.3 indicates the bound circulation, calculated from the aerodynamic coefficients. The Γ values represent the divided sectional bound circulation on the

blade in the span-wise and chord-wise directions. Each Γ element is represented using the $\Gamma_{i,j}$ notation, where the subscripts i and j represent the panel location in the transverse and longitudinal directions, respectively. The superscript ‘ ’ represents values at the reference line. Furthermore, $\mathrm{d}\Gamma$ denotes the strength of the shed vortex due to the difference in circulation in the transverse direction. The symbol ‘h’ indicates the transverse length of the panel, and $r_{i,i}$ and $r_{i,i}$ represent the transverse distances between the indicated panels, such as the indicated blue lines (in the web version) in Fig. 2.3. In turn, ‘$r_{i,i}$’ represents the distance between the center of indicated panels and the $r_{i,i}$ is the distance between the center of ith panel (first indicator) and a position on the right boundary of the ith panel (second indicator). The symbols $l_{i,(i,j)}$ and $l'_{i,(i,j)}$ represent the distances between the panel center at location (i, j) and the quarterchord line and the center of the ith panel on the reference line, respectively.

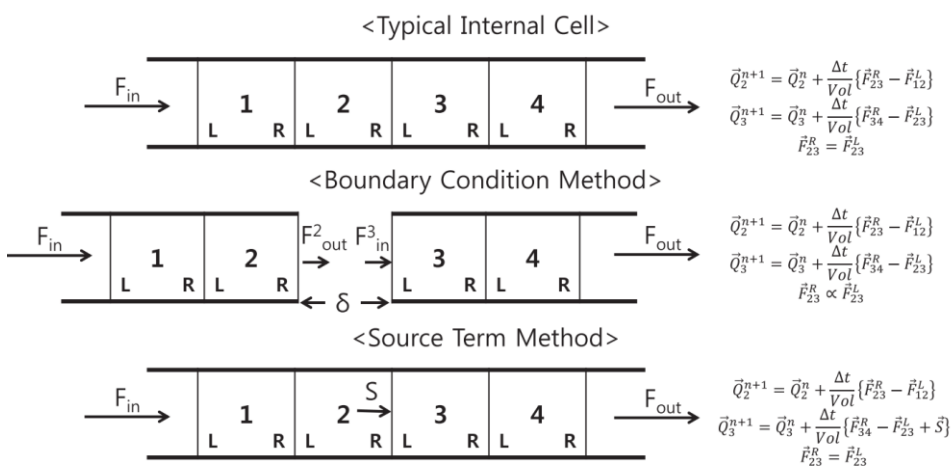

Fig. 6.1 Methods to reflect the rotor effect in the actuator surface model.

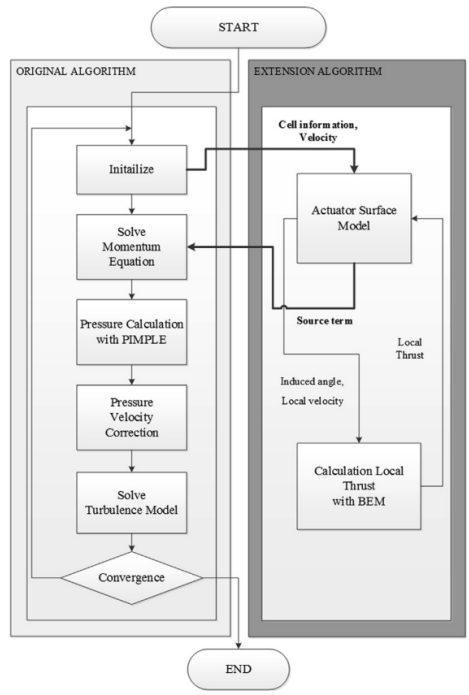

Fig. 6.2 Rotor analysis algorithm, based on an actuator surface model.

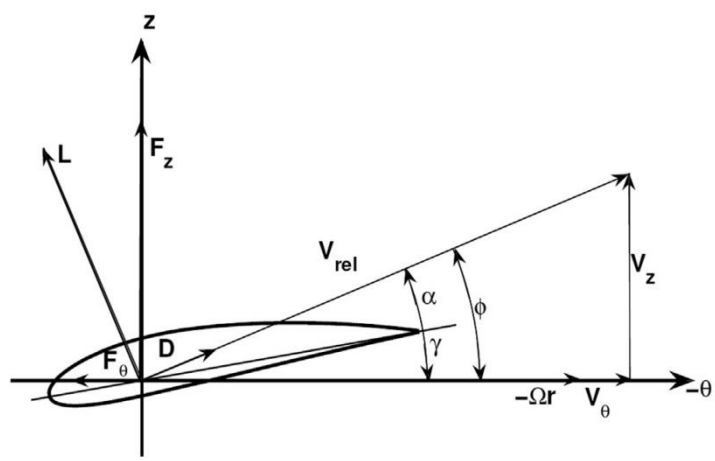

Fig. 6.3 . Aerodynamic environment of a blade element

The total strength of the circulation of the blade in Fig. 2.3 is given by Eq. (6-3). The distribution of the circulation along the longitudinal direction is in accordance to Eq. (6-4). In addition, the source term for the actuator model at the blade cells is added by Eq. (6-4). This distribution equation establishes the sectional circulation center at quarter-chord, hence the induced velocity value is almost zero at the quarter-chord line. In this way, the theory on relative velocity calculation is best explained according to the lifting line theory. This assumption is only applied for numerical calculations, and thus it does not describe the real physics. In this equation, the center of the symmetric function, like the use of the Gaussian function for other ALM/ASM methods, has been shifted so that the centerline of the blade is located at 0.25c. It should be noted that the total summation of the function values along the chord should equal to one. In order words, in all other ALM or ASM methods, Gaussian functions are used for the rotor force distribution; the center position of circulation in this method changes from the quarter-chord to the center position of the distribution function.

$$\Gamma_{blade} = \sum_{i=1}^{n} \sum_{j=1}^{m} \Gamma_{i,j} \tag{6-3}$$

$$0 \leq s < 0.25c, \qquad \Gamma_i(s) = \Gamma_i \left(0.4 + \left(\frac{3.04}{0.25} \right) \left(\frac{s}{c} \right) \right) \tag{6-4}$$

$$0.25c \le s < 0.5c, \qquad \Gamma_i(s) = \Gamma_i\left(3.44 - \left(\frac{3.2}{0.25}\right)\left(\left(\frac{s}{c}\right) - 0.25\right)\right)$$

$$0.5c \le s < 1c, \qquad \Gamma_i(s) = \Gamma_i\left(0.24 - \left(\frac{0.24}{0.5}\right)\left(\left(\frac{s}{c}\right) - 0.5\right)\right)$$

where s is the distance from the leading edge.

In this analysis, the induced velocity at the quarter-chord line derived from the lifting line theory is w_i. Because the induced velocity field obtained based on this theory is calculated from the difference of span-wise circulation, it can correctly replicate the lift distribution of a finite wing without additional tip-loss correction. Previous research was not successful in representing the span-wise difference of circulation due to the effects of the source term on the virtual blade area. This lack of clarity prevents the prediction of the 3D effects of the blade, such as the tip-loss effect. For this reason, previous research often used the tip-loss factor in the BEM to model the lift distribution at the tip region, an approach that has inherent limitations in predicting the induced velocities at the hub and tip regions of highaspect-ratio wind turbine blades. Moreover, it is customary to set a reference line at a given distance away from the blade to avoid the effects that incur due to the bound circulation of the blade. However, it is impossible to define the exact distance at which the bound circulation effects are completely eliminated, resulting in the discrepancy between the actual induced velocity and the numerically calculated velocity. Here, the velocity disturbance at the reference line due to the existence of

the blade is defined as a “displacement effect”. In the present study, the obscurity concerning the location of a reference line is overcome by the lifting line theory.

First, according to this theory, the induced velocity at the ith quarter-chord due to $\Gamma_{i,j}$ and $d\Gamma_{i,j}$ can be written as:

$$
\begin{aligned}
dw_{i,(i,j,di,dj)} &= dw_{i,(i,j)} + dw_{i,(di,dj)} \\
&= \frac{\Gamma_{i,j}}{4\pi}\int_{r_{i,i}-h}^{r_{i,i}+h} \frac{sin\theta}{\left(l_{i,(i,j)}\right)^2 + \left(r_{i,i}\right)^2} dl \\
&+ \frac{d\Gamma_{di,dj}}{4\pi}\int_{l_{i,(i,j)}}^{+\infty} \frac{sin\theta}{\left(l_{i,(i,j)}\right)^2 + \left(r_{i,di}\right)^2} dl \\
&= \frac{\Gamma_{i,j}}{4\pi}\int_{\tan^{-1}\frac{l_{i,(i,j)}}{r_{i,i}-h}}^{\tan^{-1}\frac{l_{i,(i,j)}}{r_{i,i}+h}} \frac{sin\theta}{l_{i,(i,j)}} d\theta \\
&+ \frac{d\Gamma_{di,dj}}{4\pi}\int_{\tan^{-1}\frac{r_{i,di}}{l_{i,(i,j)}}}^{\pi} \frac{sin\theta}{r_{i,di}} d\theta
\end{aligned}
\tag{6-5}
$$

The symbol ‘θ’ used in these equations represents the integral factor. On the other hand, the induced velocity at the ith reference line due to $\Gamma_{i,j}$ and $d\Gamma_{i,j}$ can be written as:

$$dw'_{i,(i,j,di,dj)} = dw'_{i,(i,j)} + dw'_{i,(di,dj)}$$

$$= \frac{\Gamma_{i,j}}{4\pi}\int_{r_{i,i}-h}^{r_{i,i}+h} \frac{sin\theta}{\left(l'_{i,(i,j)}\right)^2+\left(r_{i,i}\right)^2} dl$$

$$+ \frac{d\Gamma_{di,dj}}{4\pi}\int_{l'_{i,(i,j)}}^{+\infty} \frac{sin\theta}{\left(l'_{i,(i,j)}\right)^2+\left(r_{i,di}\right)^2} dl \qquad (6\text{-}6)$$

$$= \frac{\Gamma_{i,j}}{4\pi}\int_{\tan^{-1}\frac{l'_{i,(i,j)}}{r_{i,i}-h}}^{\tan^{-1}\frac{l'_{i,(i,j)}}{r_{i,i}+h}} \frac{sin\theta}{l'_{i,(i,j)}} d\theta$$

$$+ \frac{d\Gamma_{di,dj}}{4\pi}\int_{\tan^{-1}\frac{r_{i,di}}{l'_{i,(i,j)}}}^{\pi} \frac{sin\theta}{r_{i,di}} d\theta$$

Combining Eqs. (6-5) and (6-6), the induced velocity at the center of the ith quarter-chord is described as:

$$dw_{i,(i,j,di,dj)} = dw'_{i,(i,j,di,dj)} + \frac{\Gamma_{i,j}}{4\pi}\int_{\tan^{-1}\frac{l_{i,(i,j)}}{r_{i,i}-h}}^{\tan^{-1}\frac{l_{i,(i,j)}}{r_{i,i}+h}} \frac{sin\theta}{l_{i,(i,j)}} d\theta$$

$$- \frac{\Gamma_{i,j}}{4\pi}\int_{\tan^{-1}\frac{l'_{i,(i,j)}}{r_{i,i}-h}}^{\tan^{-1}\frac{l'_{i,(i,j)}}{r_{i,i}+h}} \frac{sin\theta}{l'_{i,(i,j)}} d\theta \qquad (6\text{-}7)$$

$$+ \frac{d\Gamma_{di,dj}}{4\pi}\int_{\tan^{-1}\frac{r_{i,di}}{l_{i,(i,j)}}}^{\tan^{-1}\frac{r_{i,di}}{l'_{i,(i,j)}}} \frac{sin\theta}{r_{i,di}} d\theta$$

Because the calculated induced velocity is derived from $\Gamma_{i,j}$ and $d\Gamma_{i,j}$, the resulting induced velocity from the entire Γ and $d\Gamma$ over the blade is written according to the following equation:

$$
\begin{aligned}
w_i = \sum_{i=1}^{n}\sum_{j=1}^{m}\left(dw'_{i,(i,j)}\right) + \sum_{di=0}^{n}\sum_{dj=1}^{m}\left(dw'_{i,(di,dj)}\right) \\
+ \sum_{i=1}^{n}\sum_{j=1}^{m}\left(\frac{\Gamma_{i,j}}{4\pi}\int_{\tan^{-1}\frac{l_{i,(i,j)}}{r_{i,i}-h}}^{\tan^{-1}\frac{l_{i,(i,j)}}{r_{i,i}+h}}\frac{sin\theta}{l_{i,(i,j)}}d\theta\right) \\
- \sum_{i=1}^{n}\sum_{j=1}^{m}\left(\frac{\Gamma_{i,j}}{4\pi}\int_{\tan^{-1}\frac{l'_{i,(i,j)}}{r_{i,i}-h}}^{\tan^{-1}\frac{l'_{i,(i,j)}}{r_{i,i}+h}}\frac{sin\theta}{l'_{i,(i,j)}}d\theta\right) \\
+ \sum_{di=0}^{n}\sum_{dj=1}^{m}\left(\frac{d\Gamma_{di,dj}}{4\pi}\int_{\tan^{-1}\frac{r_{i,di}}{l_{i,(i,j)}}}^{\tan^{-1}\frac{r_{i,di}}{l'_{i,(i,j)}}}\frac{sin\theta}{r_{i,di}}d\theta\right)
\end{aligned}
\tag{6-8}
$$

The first and second terms are the velocity components induced by the circulation of the blade at the reference line, and they are assumed identical to those obtained from the CFD calculation at the same locations. The fourth term compensates for the velocity component induced by the bound circulation of the same blade at the reference line, while the fifth term corrects for the displacement effect. The third term on the right-hand side of Eq. (6-7) is the integration of the bound circulation over the same blade region at the quarter-chord line. Based on Eq. (6-4), the induced velocity at the quarter-chord line due to the bound vortex is negligible. Hence, the resulting equation that will be actually used in the BEM calculation is:

$$w_i = w'_{cfd,i} - \sum_{i=1}^{n}\sum_{j=1}^{m}\left(\frac{\Gamma_{i,j}}{4\pi}\int_{\tan^{-1}\frac{l'_{i,(i,j)}}{r_{i,i}-h}}^{\tan^{-1}\frac{l'_{i,(i,j)}}{r_{i,i}+h}}\frac{sin\theta}{l'_{i,(i,j)}}d\theta\right) + \sum_{di=0}^{n}\sum_{dj=1}^{m}\left(\frac{d\Gamma_{di,dj}}{4\pi}\int_{\tan^{-1}\frac{r_{i,di}}{l_{i,(i,j)}}}^{\tan^{-1}\frac{r_{i,di}}{l'_{i,(i,j)}}}\frac{sin\theta}{r_{i,di}}d\theta\right) \quad (6\text{-}9)$$

As shown in Fig. 6.4, the new approach to calculate the effective angle of attack has been inserted into the original ASM algorithm, based on the previous equation.

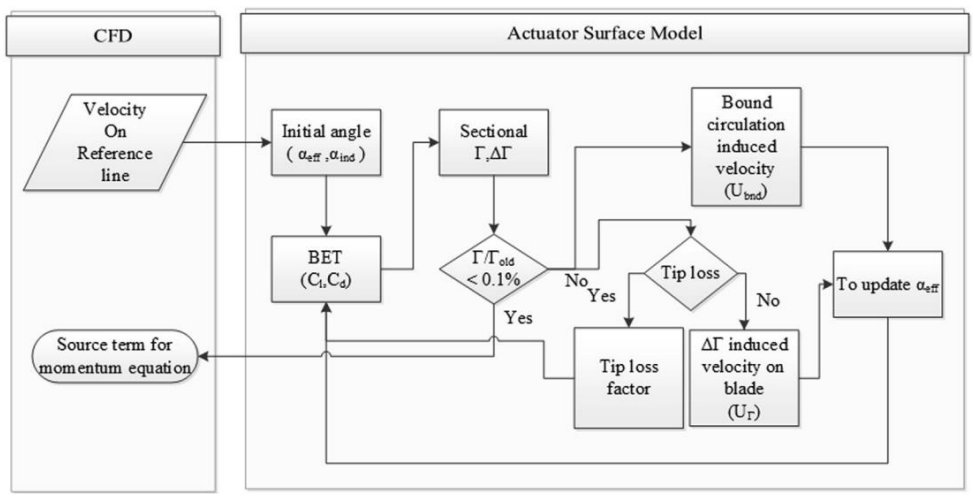

Fig. 6.4 Effective angle calculation algorithm in ASM.

6.2 Thermodynamic Model

The discretized forms of the convection terms for mass and energy conservation for finite volume method can be written as,

Mass conservation :

$$\int \nabla \cdot \left(\rho_w {h_f}^n \vec{U}_f\right) dV = \sum_{n_s} \vec{S}_n \cdot \rho_w {h_f}^n \vec{U}_f \tag{6-10}$$

Energy conservation :

$$\int \nabla \cdot \left(\rho_w {h_f}^n c_{p,w} T_{eq} \vec{U}_f\right) dV = \sum_{n_s} \vec{S}_n \cdot \rho_w {h_f}^n c_{p,w} T_{eq} \vec{U}_f \tag{6-11}$$

Here, $\vec{S}_n$ is the face vectors which is included wall adjacent cell, and n_s is the number of those faces.

The discretized forms of the mass and energy conservation are written as,

Mass conservation :

$$\rho_w \left(\frac{{h_f}^{n+1} - {h_f}^n}{\Delta t}\right) V + \sum_{n_s} \vec{S}_n \cdot {h_f}^n \rho_w \vec{U}_f = {\dot{m}_{com}}^n - {\dot{m}_{ice}}^{n+1} \tag{6-12}$$

Energy conservation :

$$\rho_w \left(\frac{\mathrm{h_f}^{n+1} c_{p,w} T_{eq}^{\,n+1} - \mathrm{h_f}^{n} c_{p,w} T_{eq}^{\,n}}{\Delta t} \right) V + \sum_{n_s} \vec{S}_n \cdot \rho_w \mathrm{h_f}^{n} c_{p,w} T_{eq} \vec{U}_f = \dot{m}_{com} \left[c_{p,w} T_{d,\infty} + \frac{1}{2} \left| \vec{U}_d \right|^2 \right] + \dot{m}_{ice}^{\,n+1} \left[L_{fus} - c_{p,i} T_{eq} \right] - h_c A \left(T_{eq} - T_\infty \right) \tag{6-13}$$

Where the superscript n and $n+1$ mean previous and current time step, respectively. Different approaches are applied according to the surface conditions such as (I) ice only, (II) water and ice, and (III) Water only.

(I) Ice only

$\mathrm{h_f}^{n+1}$ can be defined by assumption that the surface consists of ice. In the ice surface, the entire water film is freezing. Thus $\mathrm{h_f}^{n+1}$ is equal to zero. At the first step, $\dot{m}_{ice}^{\,n+1}$ is determined in the mass conservation. By using the determined $\dot{m}_{ice}^{\,n+1}$ in mass conservation, $T_{eq}^{\,n+1}$ is calculated from energy conservation. By applying $\mathrm{h_f}^{n+1} = 0$. The mass conservation can be expanded as,

$$\dot{m}_{ice}^{\,n+1} - \frac{V}{\Delta t} \rho_w \mathrm{h_f}^{n} + \sum_{n_s} \vec{S}_n \cdot \rho_w \mathrm{h_f}^{n} \vec{U}_f = \dot{m}_{com}^{\,n} \tag{6-14}$$

$$\dot{m}_{ice}^{\,n+1} = \dot{m}_{com}^{\,n} + \frac{V}{\Delta t} \rho_w \mathrm{h_f}^{n} - \sum_{n_s} \vec{S}_n \cdot \rho_w \mathrm{h_f}^{n} \vec{U}_f \tag{6-15}$$

The energy conservation can be expanded as,

$$-\frac{V}{\Delta t}\rho_w {h_f}^n {c_{p,w}} {T_{eq}}^n + \sum_{n_s} \vec{S}_n \cdot \rho_w {h_f}^n c_{p,w} T_{eq} \vec{U}_f = \dot{E}_{com} + {\dot{m}_{ice}}^{p+1}\left[L_{fus} - c_{p,i}T_{eq}\right] - h_c A {T_{eq}}^{n+1} + h_c A T_\infty \quad (6\text{-}16)$$

The updated $\dot{m}_{ice}$ form the mass conservation is denoted as ${\dot{m}_{ice}}^{p+1}$ in Eq. (6-15). The final equilibrium temperature (${T_{eq}}^{n+1}$) is given as,

$${T_{eq}}^{n+1} = \left(\frac{V}{\Delta t}\rho_w {h_f}^n {c_{p,w}} {T_{eq}}^n - \sum_{n_s} \vec{S}_n \cdot \rho_w {h_f}^n c_{p,w} T_{eq} \vec{U}_f + \dot{E}_{com} + {\dot{m}_{ice}}^{p+1} L_{fus} + h_c T_\infty\right) / \left({\dot{m}_{ice}}^{p+1} c_{p,i} + h_c A\right) \quad (6\text{-}17)$$

(II) Water and ice

For water and ice condition, the equilibrium temperature is assumed as 273.15K. The other two unknowns (${h_f}^{n+1}$ and ${\dot{m}_{ice}}^{n+1}$) are included in both mass and energy conservation. ${h_f}^{n+1}$ is calculated form the mass conservation, and then ${\dot{m}_{ice}}^{n+1}$ is determined form the energy conservation.

The mass conservation can be written as,

$$\frac{V}{\Delta t}\rho_w {h_f}^{n+1} - \frac{V}{\Delta t}\rho_w {h_f}^{n} + \sum_{n_s} \vec{S}_n \cdot \rho_w {h_f}^{n} \vec{U}_f = {\dot{m}_{com}}^{n} - {\dot{m}_{ice}}^{n} \tag{6-18}$$

The final ${h_f}^{n+1}$ is given as,

$$h_f{}^{n+1} = \frac{\left(\frac{V}{\Delta t}\rho_w {h_f}^{n}\right)}{\frac{\rho_w V}{\Delta t}} - \frac{\left(\sum_{n_s} \vec{S}_n \cdot \rho_w {h_f}^{n} \vec{U}_f\right)}{\frac{\rho_w V}{\Delta t}} + \frac{[{\dot{m}_{com}}^{n} - {\dot{m}_{ice}}^{n}]}{\frac{\rho_w V}{\Delta t}} \tag{6-19}$$

From the updated ${h_f}^{p+1}$ and the assumption of the surface temperature ($T_c = 273.15K$), the energy conservation can be given as,

$$\begin{aligned} \frac{V}{\Delta t}\rho_w {h_f}^{p+1}\ c_{p,w}T_c - \frac{V}{\Delta t}\rho_w {h_f}^{n} c_{p,w}{T_{eq}}^{n} \\ + \sum_{n_s} \vec{S}_n \cdot \rho_w {h_f}^{n} c_{p,w} T_{eq} \vec{U}_f \\ = {\dot{E}_{com}}^{n} + {\dot{m}_{ice}}^{n+1}\left[L_{fus} - c_{p,i}T_c\right] \\ - h_c A(T_c - T_\infty) \end{aligned} \tag{6-20}$$

The final ${\dot{m}_{ice}}^{n+1}$ is determined as shown in Eq. (6-21).

$$\dot{m}_{ice}{}^{n+1} = \frac{\frac{V}{\Delta t}\rho_w {h_f}^{p+1} c_{p,w} T_c - \frac{V}{\Delta t}\rho_h{}^n c_{p,w} {T_{eq}}^n + }{L_{fus} - c_{p,i} T_c}$$
$$+ \frac{\sum_{n_s} \vec{S}_n \cdot \rho_w {h_f}^n c_{p,w} T_{eq} \vec{U}_f}{L_{fus} - c_{p,i} T_c} \quad (6\text{-}21)$$
$$+ \frac{\left[\dot{E}_{com}{}^n + h_c A(\mathrm{T}_c - T_\infty)\right]}{L_{fus} - c_{p,i} T_c}$$

(III) Water only

For water condition, $\dot{m}_{ice}{}^{n+1}$ is assumed to be zero. The other two unknowns (${\mathrm{T}_{eq}}^{n+1}$ and ${\mathrm{h}_f}^{n+1}$) are included in both mass and energy conservation. Because ${\mathrm{T}_{eq}}^{n+1}$ is belong to energy conservation, ${\mathrm{h}_f}^{n+1}$ should be determined by mass conservation.

By neglecting $\dot{m}_{ice}{}^{n+1}$, mass conservation can be reduced as described in Eq. (6-22). From the Eq. (6-22), ${\mathrm{h}_f}^{n+1}$ is directly determined as shown in Eq. (6-23).

$$\left(\frac{\rho_w {h_f}^{n+1} - \rho_w {h_f}^n}{\Delta t}\right) V + \sum_{n_s} \vec{S}_n \cdot \rho_w {h_f}^n \vec{U}_f = \dot{m}_{com}{}^n \quad (6\text{-}22)$$

$$h_f{}^{n+1} = h_f{}^n - \frac{\Delta t \sum_{n_s} \vec{S}_n \cdot h_f{}^n \vec{U}_f}{V} + \frac{\Delta t \cdot \dot{m}_{com}{}^n}{\rho_w V} \quad (6\text{-}23)$$

The calculated ${\mathrm{h}_f}^{n+1}$ is treated as a source term, and $\dot{E}_{ice}{}^{n+1}$ is set to zero in energy conservation. Consequently, ${\mathrm{T}_{eq}}^{n+1}$ can be obtained by energy conservation. As shown in Eq. (6-24), ${T_{eq}}^{n+1}$ can be updated via Eq. (6-25).

$$\frac{V}{\Delta t}\rho_w {h_f}^{p+1} c_{p,w} {T_{eq}}^{n+1} - \frac{V}{\Delta t}\rho_w {h_f}^{n} c_{p,w} {T_{eq}}^{n} + \sum_{n_s} \vec{S_n} \cdot \rho_w {h_f}^{n} c_{p,w} T_{eq} \vec{U_f} = \dot{E}_{com} - h_c A {T_{eq}}^{n+1} + h_c A T_\infty \quad (6\text{-}24)$$

$${T_{eq}}^{n+1} = \frac{\frac{V}{\Delta t}\rho_w {h_f}^{n} c_{p,w} {T_{eq}}^{n}}{\frac{V}{\Delta t}\rho_w {h_f}^{p+1} c_{p,w} + h_c A} - \frac{\sum_{n_s} \vec{S_n} \cdot \rho_w {h_f}^{n} c_{p,w} T_{eq} \vec{U_f}}{\frac{V}{\Delta t}\rho_w {h_f}^{p+1} c_{p,w} + h_c A} + \frac{\dot{E}_{com} + h_c A T_\infty}{\frac{V}{\Delta t}\rho_w {h_f}^{p+1} c_{p,w} + h_c A} \quad (6\text{-}25)$$

6.3 Coefficient of RSM

Table 6.1 Regression coefficients based on EAV-2H+

	ΔM_{ice}(%)	ΔC_L(%)	ΔC_D(%)
C_0	-202.119	-809.135	-3292.91
C_1	100.983	321.3053	1271.152
C_2	1.451925	6.223222	25.321
C_{11}	5.264113	-19.7837	-41.8041
C_{12}	-0.40224	-1.10739	-4.53087
C_{22}	-0.00255	-0.01187	-0.04849

6.4 AOPA Icing Risk Table

The icing risk is categorized according to cloud type and temperature range in the AOPA report [4]. The icing AOPA's risk categories are summarized in Table 6.2.

Table 6.2 AOPA icing risk Table [4]

	Icing Risk		
Cloud type	Cumulus clouds	Stratiform clouds	Rain and drizzle
High	0 to -20°C	0 to -15°C	0°C and below
Medium	-20 to -40°C	-15 to -30°C	
Low	Less than -40°C	Less than -30°C	

7. Reference

[1] Han, T., “Theoretical and Experimental Study of Scaling Methods for Rotor Blade Ice Accretion Testing,” M.S. Thesis, Pennsylvania State University, Old Main, University Park, PA, 2011.

DOI: 10.13140/RG.2.1.2585.0485

[2] Gent, R. W., Dart, N. P., and Cansdale, J. T. Aircraft icing. Philosophical Transactions of the Royal Society of London A: Mathematical, Physical and Engineering Sciences, Vol. 358, No. 1776, pp. 2873-2911. 2000.

[3] AGARD (Advisory Group for Aerospace Research & Development), “Ice accretion simulation,” Report of Fluid Dynamics Panel, NATO report AGARD – AR - 344, December, 1997.

[4] “Aircraft Icing,” Safety Advisor, AOPA Air Safety Foundation, No. 1, 2002. http://www.asf.org.

[5] National Transportation Safety Board, “ Accident report – Loss of control on approach Colgan Air, Inc. operating as Continental Connection Flight 3407 Bombardier DHC-8-400, N200WQ Clarence Center," NTSB/AAR-10/01, February 12, 2009.

[6] Kubi, A. P., “U.S Inflight Icing Accidents and Incidents, 2006 to 2010,” M.S. Thesis, University of Tennessee, Knoxville, TN, 2011.

[7] Peck, L., Ryerson, C. C., and Martel, C. J., “Army Aircraft Icing,” U.S. Army Cold Regions Research and Engineering Lab. TR-02-13, Hanover, NH, Sept. 2002.

[8] “Title 14-Aeronautics and Space, Part 25—Airworthiness Standards: Transport Category Airplanes,” Code of Federal Regulations, Federal Aviation Administration, revised and reissued annually.

[9] Federal Aviation Administration, “Capabilities and Prospects for Improvement in Aircraft Icing Simulation Methods: Contributions to the 11C Working Group,” DOT/FAA/AR-01/28, Washington, D.C., May, 2001.

[10] Messinger, B. L., "Equilibrium Temperature of an Unheated Icing Surface as a Function of Air Speed," Journal of the Aeronautical Sciences, Vol. 20, No. 1, pp. 29-42, 1953.
https://doi.org/10.2514/8.2520

[11] Wright, W. B., "Users manual for the improved NASA Lewis ice accretion code LEWICE 1.6,” NASA CR 198355, 1995.

[12] Ruff, G. A., and Berkowitz, B. M., "Users’ Manual for the NASA Lewis Ice-accretion Prediction Code (LEWICE),” NASA CR 185129, pp. 55-58, 1990.

[13] Cebeci, T., Chen, H., and Alemdaroglu, N., “Fortified LEWICE with Viscous Effects,” 28th Aerospace Sciences Meeting, AIAA 90-0754, Reno, NV, Jan. 1990.

[14] Potapczuk, M. G., “LEWICE/E: An Euler Based Ice Accretion Code,” 30th Aerospace Sciences Meeting, AIAA 92-0037 Reno, NV, Jan. 1992.

[15] Wright, W. B., Gent, R. W., and Guffond, D., "DRA/NASA/ONERA Collaboration on Icing Research Part II-Prediction of Airfoil Ice Accretion," NASA CR 202349, Lewis Research Center, pp.1-5. 1997.

[16] Hedde, T., and Guffond, D., "ONERA Three-Dimensional Icing Model," AIAA Journal, Vol. 33, No. 6, 1995, pp. 1038-1045.

[17] Gent, R. W., "TRAJICE2–A Combined Water Droplet Trajectory and Ice Accretion Prediction Program for Aerofoils," Defence Research Agency, RAE-TR-90054, November, 1990.

[18] Tran, P., Brahimi, M. T., Paraschivoiu, I., Pueyo, A., and Tezok, F. "Ice Accretion on Aircraft Wings with Thermodynamic Effects," Journal of Aircraft, Vol. 32, No. 2, pp. 444–446. 1995.
https://doi.org/10.2514/3.46737

[19] Tran, P., Brahimi, M. T., Tezok, F., and Paraschivoiu, I., "Ice Accretion on Supercritical and Multi-Element Airfoils," 33rd Aerospace Sciences Meeting, AIAA 95-0754, Reno, NV, Jan. 1995.

[20] Pueyo, A., Chocron, D., and Kafyeke, F., "Improvements to the Ice Accretion Code CANICE," 8th Aerodynamic Symposium of 48th CASI Conference, Toronto, Canada, Apr. 2001.

[21] Beaugendre, H., Morency, F., and Habashi, W. G., "FENSAP-ICE's Three-Dimensional In-Flight Ice Accretion Module: ICE3D", Journal of Aircraft, Vol. 40, No. 2, pp. 239–247. 2003.
doi : 10.2514/2.3113

[22] Remaki, L., Beaugendre, H., and Habashi, W. G., "ISOD – An Anisotropic Isovalue-Oriented Diffusion Artificial Viscosity for the Euler and Navier–Stokes Equations," Journal of Computational Physics, Vol. 186, No. 1, pp. 279-

294, 2003.

https://doi.org/10.1016/S0021-9991(03)00066-4

[23] Bourgault, Y., Habashi, W.G., Dompierre, J. and Baruzzi, G.S., "A Finite Element Method Study of Eulerian Droplets Impingement Models," International Journal for Numerical Methods in Fluids, Vol. 29, pp. 429-449, 1999.

doi : 10.1002/(SICI)1097-0363(19990228)29:4<429::AID-FLD795>3.0.CO;2-F

[24] Beaugendre, H., Morency, F., Habashi, W. G., and Benquet, P., "Roughness implementation in FENSAP-ICE: Model Calibration and Influence on Ice Shapes," Journal of Aircraft, Vol. 40, No. 6, pp. 1212-1215, 2003.

https://doi.org/10.2514/2.7214

[25] Bartlett, P., "Development of a New Model of Ice Accretion on Aircraft," 9th International Workshop on Atmospheric Icing of Structures (IWAIS 2000), June, Chester, UK., 2000.

[26] Myers, T. G., "Extension to the Messinger Model for Aircraft Icing," AIAA Journal, Vol. 39, No. 2, pp. 211-218. 2001.

https://doi.org/10.2514/2.1312

[27] Verdin, P., Charpin, J. P. F., and Thompson, C. P., "Multistep Results in ICECREMO2". Journal of Aircraft, Vol. 46, No. 5, pp. 1607-1613. 2009.

https://doi.org/10.2514/1.41451

[28] Dow, Sr., J., Aliaga, C., Shah, S., Chen, J., Habashi, W. G., Siemens, J. L., "FENSAP-ICE in Aid of Certification: From CFD to Flight Testing," SAE Technical Paper 2011-38-0033, 2011 https://doi.org/10.4271/2011-38-0033

[29] Cebeci, T., Kafyeke, K., “Aircraft Icing,” Annual Review of Fluid Mechanics, Vol. 35, pp. 11-21., 2003. https://doi.org/10.1146/annurev.fluid.35.101101.161217

[30] Frink, T. N., Murphy , P. C., Atkins, H. L., Viken, S. A., Petrilli, J. L., Gopalarathnam, A., and Paul, R. C., "Computational Aerodynamic Modeling Tools for Aircraft Loss of Control", Journal of Guidance, Control, and Dynamics, Vol. 40, No. 4, pp. 789-803. 2017.

[31] O'brien, M., “Google, Facebook in Race to Build High-Altitude Aircraft,” Mercury News, August 12, 2016. http://www.mercurynews.com/2015/11/28/google-facebook-in-race-to-build-high-altitude-aircraft/

[32] Jung, S. K., “Korea's 'Surion' Helicopter Supply Halted After Test Failure,” DefenseNews, September 28, 2016. https://www.defensenews.com/digital-show-dailies/ausa/2016/09/28/korea-s-surion-helicopter-supply-halted-after-test-failure/

[33] Vogel, G. N., “Icing Considerations for HALE (High Altitude, Long Endurance) Aircraft,” No. NEPRF-TR-88-11, NAVAL Environmental Prediction Research Facility Monterey, CA, 1988.

[34] Iya, S. K., and Cook, D. E., “Icing Characteristics of a High-Altitude Long-Endurance Aircraft Wing Airfoil,” 29th Aerospace Sciences Meeting, AIAA 91-0562, Reno, NV, Jan. 1991.

[35] Bottyán, Z., “In-Flight Icing Characteristics of Unmanned Aerial Vehicles during Special Atmospheric Condition over the Carpathian-Basin,” Landscape and Environment, Vol. 7. No. 2, 2013. pp. 74–80.

[36] Srikumar, P., “Unmanned Aircraft Systems: Challenges and Opportunities,” International Journal of Advances in Engineering Sciences and Applied Mathematics, Vol. 6, No. 3, 2014, pp. 195–202.
doi : 10.1007/s12572-014-0116-8

[37] Hwang, S., Kim, S., Kim, C., and Lee Y., "Aerodynamic Design of the Solar-Powered High Altitude Long Endurance (HALE) Unmanned Aerial Vehicle (UAV)." International Journal of Aeronautical and Space Science, Vol. 17, No. 1, 2016, pp. 132–138.
doi : 10.5139/IJASS.2016.17.1.132

[38] Bailey, N., “Helicopter Pilot's Manual Vol 1: Principles of Flight and Helicopter Handling,” Crowood Press, Ramsbury, England, U.K., pp. 99-101, 2014.

[39] Szilderm, K., “Numerical Simulation of Ice Formation on a Helicopter Fuselage,” SAE Technical Paper series, 2007-01-3308, 2007.

[40] Szikder, K., and Kozowski, E., “Numerical Simulation of Cloud Drop Impingement on a Helicopter,” 27th International Congress of the Aeronautical Science, 2010.

[41] Aliaga, C. N., Aubé, M. S., Baruzzi, G. S., and Habashi, W. G., “FENSAP-ICE-Unsteady: Unified In-Flight Icing Simulation Methodology for Aircraft, Rotorcraft, and Jet Engines,” Journal of Aircraft, Vol. 48, No. 1, pp. 119–126, 2011.

[42] Ahn, G. B., Jung, K. Y., Myong, R. S., Shin, H. B., and Habashi, W. G., "Numerical and Experimental Investigation of Ice Accretion on Rotorcraft Engine Air Intake", Journal of Aircraft, Vol. 52, No. 3, pp. 903-909, 2015.

[43] Fouladi, H., Habashi, W. G., and Ozcer, I. A., “Quasi-Steady Modeling of Ice Accretion on a Helicopter Fuselage in Forward Flight,” Journal of Aircraft, Vol. 50, No. 4, pp. 1169–1178, 2013.

[44] Leishman, J. G., “Principles of Helicopter Aerodynamics,” Cambridge University Press, Cambridge, England, U.K. pp. 158-160, 2006.

[45] Kim, T., Oh, S., and Yee, K., “Improved Actuator Surface Method for Wind Turbine Application,” Renewable Energy, Vol. 76, pp. 16-26, 2015.

[46] O'Brien, D. M. Jr., “Analysis of Computational Modeling Techniques for Complete Rotorcraft Configurations,” Dissertation, Georgia Institute of Technology, Atlanta, Georgia, 2006.

[47] OpenFOAM: “The Open Source CFD Toolbox, User Guide, Version 2.3.1,” OpenFOAM, 2014.

[48] Ferziger, J. H., and Peric, M., “Computational Methods for Fluid Dynamics, 3rd edition” Vol. 3, Springer Berlin, 1996.

ISBN 978-540-42074-3

[49] Jasak, H., “Error Analysis and Estimation for the Finite Volume Method with Applications to Fluid Flows,” Ph.D. thesis, Imperial College, London, U.K., 1996.

[50] Issa, R. I., “Solution of the Implicitly Discretised Fluid Flow Equations by Operator-Splitting,” Journal of Computational physics, Vol. 62, No. 1, pp. 40 - 65, 1986.

[51] Versteeg, H. K., Malalasekera, W., “An Introduction to Computational Fluid Dynamics: The Finite Volume Method 2nd edition,” Pearson Education Limited, England, 2007.

ISBN 978-0-13-127498-3

[52] Spalart, P. R., Aupoix, B., “Extensions of the Spalart–Allmaras Turbulence Model to Account for Wall Roughness,” International Journal of Heat and Fluid Flow, Vol. 24, No. 4, pp. 454–462, 2001.

[53] Cao, Y., Zhang, Q., and Sheridan, J., “Numerical Simulation of Rime Ice Accretions on an Aerofoil Using an Eulerian Method,” The Aeronautical Journal, Vol. 112, No. 1131, pp. 243–249, 2008.

[54] Rivera, N. A. C., “An Unsteady Multiphase Approach to In-Flight Icing,” Thesis, McGill University, Montreal, Quebec, 2008.

[55] Broeren, A. P., Bragg, M. B., Addy, H. E., Lee, S., Moens, F., and Guffond, D. “Effect of High-Fidelity Ice-Accretion Simulations on Full-Scale Airfoil Performance,” Journal of Aircraft, Vol. 47, No. 1, 2010, pp. 240–254.

doi : 10.2514/1.45203

[56] Jin, W., and Lee, Y., “Drag Reduction Design for a Long-endurance Electric Powered UAV," International Journal of Aeronautical and Space Sciences, Vol. 16, No.2, 2015, pp. 311–324.
doi : 10.5139/IJASS.2015.16.2.311

[57] Elliot, J. W., Althoff, S. L., and Sailey R. H., “Inflow Measurement Made with a Laser Velocimeter on a Helicopter Model in Forward Flight-μ=0.15,” NASA-TM-100542, 1988.

[58] Kenyon A. R., and Brown R. E., “Wake Dynamics and Rotor Fuselage Aerodynamic Interactions,” Journal of the American Helicopter Society, Vol. 54, No. 1, pp. 12003, 2009.

[59] Nam, H. J., and Kwon, O. J., “Simulation of Unsteady Rotor-Fuselage Aerodynamic Interaction Using Unstructured Adaptive Meshes,” Journal of the American Helicopter Society, Vol. 51, No. 2, pp. 141-149, 2006.

[60] Mills, A. F., and Hang, X., “On the Skin Friction Coefficient for a Fully Rough Flat Plate,” Journal of Fluids Engineering, Vol. 105, No. 3, pp. 364–365, 1983.

[61] Breer, M. D., Yeong, H. W., Bidwell, C. S., Bencic, T. J., Hung, K. E., Papadakis, M., and Vu, G. T., “Experimental Investigation of Water Droplet Impingement on Airfoils, Finite Wings, and an S-duct Engine Inlet,” NASA/TM-2002-211700, 2002.

[62] Langmuir, I., and Blodgett, K., “Mathematical Investigation of Water Droplet Trajectories,” U.S. Army Air Force Tech. Rept. 5418, 1946.

[63] Wright, W. B., and Rutkowski, A., "Validation Results for LEWICE 2.0," NASA CR-1999-208690, 1999.

[64] Ozcer, I. A., Baruzzi, G. S., Reid, T., Habashi, W. G., Fossati, M., Croce, G., "FENSAP-ICE: Numerical Prediction of Ice Roughness Evolution, and its Effects on Ice Shapes," SAE International, Technical Paper 2011-38-0024, 2011. doi : 10.4271/2011-38-0024

[65] Nakakita, K., Nadarajah, S., Habashi, W., "Toward Real-Time Aero-Icing Simulation of Complete Aircraft via FENSAP-ICE," Journal of Aircraft, Vol. 47, No. 1, 2010, pp. 96–109.
doi : 10.2514/1.44077

[66] Wang, J., Rossow, W. B., and Zhang, Y. "Cloud Vertical Structure and Its Variations from a 20-yr Global Rawinsonde Dataset," Journal of Climate, Vol. 13, No. 17, 2000, pp. 3041–3056.
doi : https://doi.org/10.1175/1520-0442(2000)013<3041:CVSAIV>2.0.CO;2

[67] Wang, J., and William B. R. "Determination of Cloud Vertical Structure from Upper-Air Observations," Journal of Applied Meteorology, Vol. 34, No. 10, 1995, pp. 2243–2258.
doi : https://doi.org/10.1175/1520-0450(1995)034<2243:DOCVSF>2.0.CO;2

[68] Sand, W. R., Cooer W. A., Politovich, M. K., and Veal, D. L., "Icing Conditions Encountered by a Research Aircraft, Journal of Climate and Applied Meteorology, Vol. 23, No. 10, 1984, pp. 1427–1440.
doi : https://doi.org/10.1175/0733-3021-23.10.1427

[69] Myers, R. H., and Montgomery, D., C., Response Surface Methodology, JOHN WILEY & SONS, INC., New York, 1995, pp. 43–45.
ISBN : 0-417-58100-3

[70] Chung, K. H., and D. J. Lee., "Numerical Prediction of Rotor Tip-Vortex Pairing by Using a Time-Marching Free-Wake Method." Computational Fluid Dynamics Journal, Vol. 12, No. 1, pp. 80-88, 2003.

[71] Dubief, Y., and Franck, D., "On Coherent-Vortex Identification in Turbulence." Journal of Turbulence, Vol. 1. No. 11, pp. 1-22, 2000.

[72] Rosen, K. M., and Potash, M. L., “Forty Years of Helicopter Ice Protection Experience at Sikorsky Aircraft,” Journal of the American Helicopter Society, Vol. 26, No. 3, pp. 5-19, 1981.

[73] Narducci, R., and Kreeger, R. E. “Analysis of a Hovering Rotor in Icing Conditions,” NASA/TM-2012-217126, 2012.

[74] Narducci, R., Orr, S., and Kreeger, R. E., “Application of a High-Fidelity Icing Analysis Method to a Model-Scale Rotor in Forward Flight,” NASA/TM-2012-217122, 2012.

[75] Xi, C., and Qi, Z., "Numerical Simulations for Ice Accretion on Rotors Using New Three-Dimensional Icing Model", Journal of Aircraft, Vol. 54, No. 4, pp. 1428-1442, 2017.
https://doi.org/10.2514/1.C033986

[76] Achenbach , E., “The Effects of Surface Roughness on the Heat Transfer from a Circular Cylinder to the Cross Flow of Air,” International Journal of Heat

Mass Transfer, Vol. 20, No. 4, pp. 359-369, 1997.
https://doi.org/10.1016/0017-9310(77)90157-0

[77] J. Shin, “Characteristics of Surface Roughness Associated with Leading-Edge Ice Accretion,” Journal of Aircraft, Vol. 33, No. 2, pp. 316-321, 1996.
https://doi.org/10.2514/3.46940

[78] Fortin, G., Ilinca, A., Laforte, J., and Brandi, V., “New Roughness Computation Method and Geometric Accretion Model for Airfoil Icing”, Journal of Aircraft, Vol. 41, No. 1, pp. 119-127, 2004.
https://doi.org/10.2514/1.173

[79] Croce, G., Candido, E. G., Habashi, W. G., Munzar, J., Aubé, M. S., Baruzzi, G. S., and Aliaga, C. N., “FENSAP-ICE: Analytical model for spatial and Temporal Evolution of In-Flight Icing Roughness,” Journal of Aircraft, Vol. 47, No. 4, pp. 1283-1289, 2010.
https://doi.org/10.2514/1.47143

[80] Réthoré, P. E., and Sørensen, N. N., “A Discrete Force Allocation Algorithm for Modelling Wind Turbines in Computational Fluid Dynamics” Wind Energy, Vol. 15, No, 7, pp, 915-926, 2012.
doi :10.1002/we.525

8. Nomenclature

A	=	wing area, m^2
α	=	angle of attack, $^\circ$
α_i	=	local effective angle of attack, $^\circ$
α_s	=	shaft tilt angle, $^\circ$
b	=	span length, m
β	=	local collection efficiency
β_{tot}	=	total collection efficiency
β^*	=	non-dimensionalized collection efficiency by rotor tip speed
c	=	chord length, m
C	=	coefficients for response surface models
C_D	=	drag coefficient
C_L	=	lift coefficient
C_T	=	thrust coefficient
C_p	=	pressure coefficient
$C_{p,w}$	=	specific heat of water
$C_{p,i}$	=	specific heat of ice
D	=	single droplet diameter, m
Δt	=	exposed time in icing condition, s
E	=	total internal energy
η	=	efficiency
$\vec{g}$	=	gravitational acceleration, 9.81 m/s^2
γ	=	flight path angle, °
H	=	total enthalpy
h	=	height, m
h_t	=	ice thickness, m
h_c	=	heat convection coefficient, $W/m^2 \cdot K$
h_f	=	height of water film, m
h_{max}	=	non-dimensionalized maximum thickness of ice
K	=	droplet inertia parameter
l	=	length of fuselage, 2m

L_{fus}	=	latent heat of fusion, 334 kJ/kg
LWC	=	liquid water contents, g/m^3
$MTOW$	=	maximum take-off weight, kg
MVD	=	median volumetric droplet diameter, μm
$\dot{m}_{com}$	=	impinging water rate, kg/s
$\dot{m}_{ice}$	=	accumulated ice rate, kg/s
M_∞	=	Mach number
$\vec{n}$	=	outward normal vector of surface
μ	=	advance ratio, or viscosity of air, Pa·s
p	=	pressure, Pa
P	=	instant power, J/s
Q	=	Q-criterion
Re	=	Reynolds number
R_{std}	=	standardized residual
ρ	=	density, g/m^3
ρ_w	=	density of water, g/m^3
$\bar{\rho}$	=	bulk density, g/m^3
s	=	length of wrap-around direction, m
$\vec{S}_{act}$	=	source term of actuator surface and disk method
σ	=	deviation
t_{ice}	=	exposure time in icing conditions, s
t_m	=	total time to reach the mission altitude, s
T_∞	=	freestream temperature, K
$\tilde{T}_{eq}$	=	equilibrium temperature, ℃
$\vec{\tau}_{wall}$	=	shear stress on the water film from air, Pa
$\vec{u}$	=	velocity vector, m/s
$\overline{U}_f$	=	mean velocity of water film, m/s
V_∞	=	freestream velocity, m/s
V	=	volume of cell, m^3
$W_{battery}$	=	battery capacity, kWh
W_{req}	=	total required power, kWh
x	=	chord-wise location, m
ψ	=	azimuth angle, °

y	=	span-wise location, m

Sub

a	=	air properties
bat	=	battery
clean	=	properties of clean surface
con	=	controllers
conv	=	convection
d	=	droplet properties
h	=	horizontal axis
i	=	ice properties
ice	=	properties of surfaces with ice accumulation
∞	=	freestream
mot	=	motors
pro	=	propellers
tot	=	total
v	=	vertical axis
w	=	water properties

초 록

미국 연방 항공 규정에서는 항공기의 크기와 형태에 따라 항공기 등급을 지정하고 있고, 인증을 받아야 하는 착빙 환경을 제시하고 있다. 대부분의 항공기 착빙 연구는 미국 연방 항공 규정에서 제시된 10 명 이상의 승객이 탑승하는 고정익 항공기를 대상으로 한다. 승객이 탑승하는 고정익 항공기의 실속 속도가 실험 또는 수치적 방법의 주요 관심대상이다. 회전익 항공기의 경우, 고정익 항공기를 위해 제정된 규정과 착빙 환경을 따르고 있으며, 무인 항공기의 경우 관련 규정이 부재한 실정이다. 이러한 규정하에서 최근까지 수행된 항공기 착빙 연구는 다음과 같은 문제를 가지고 있다.

첫째, 규정에서 제시된 형태의 항공기와, 이러한 항공기의 실속 속도가 아닌 저속 비행 조건에서 발생하는 착빙 형상의 특징이 명확하게 밝혀지지 않았다. 최근까지도 착빙 형상을 지배하는 무차원화 변수가 알려지지 않았다. 따라서 고정익 항공기의 실속 속도를 대상으로 수행한 선행 연구 결과를 보다 저속 비행하는 타 항공기에 적용하는데 어려움이 있다. 따라서, 다양한 임무 형상을 가지는 항공기에 발생하는 착빙 형상의 특성과 이에 따른 공기역학적 성능을 분석할 필요가 있다.

둘째, 주어진 기상조건에서 항공기의 운항 가능성을 판단하는 것이 항공기 착빙 연구의 궁극적인 목표라 할 수 있다. 그러나 최근까지의 연구는 정밀한 착빙 형상 예측과 이에 따른 항공기의 성능 변화를 평가하고 있다. 착빙이 발생할 것이라 예상이 되는 기상조건이 제시되어 있더라도, 항공기의 운항 안전성을 평가할 수 있는 절차나 기법이

부재한 실정이다. 따라서 착빙 조건이 주어질 경우 항공기의 운항 안전성을 사전에 평가할 수 있는 새로운 기법이 필요하다.

셋째, 고정익 항공기에 초점을 맞추어 수치해석 기법이 발달하였기 때문에 헬리콥터 동체에 발생하는 착빙 형상을 예측하기 위한 정밀한 해석 도구가 부재하다. 정밀한 착빙 해석을 위하여 동체와 깃끝 와류의 간섭 효과를 고려하는 것은 필수적이다. 그러나 실험적 연구는 고정익 항공기와 동일하게 로터를 제외하고 순수 동체를 대상으로 하였다. 수치적 연구에서는 깃끝 와류의 거동을 모사할 수 없는 단순한 유동 해석 기법을 적용하고 있다. 따라서, 정밀한 유동 해석 기법과 착빙 해석 기법을 적용하여 선행 연구 결과의 타당성을 평가하고, 동체와 깃끝 와류의 간섭 효과에 의한 착빙 특성을 파악할 필요가 있다.

이에 본 연구에서는 최신의 수치해석 기법을 적용하여 3 차원 물체에 발생하는 착빙 현상을 해석하기 위한 시뮬레이션 프로그램인 Ice Shape Estimation and Performance Analysis Code (ISEPAC) 를 개발하였다. ISEPAC 은 고정익 항공기 및 회전익 항공기의 깃끝 와류의 생성과 이동, 소산을 직접 다룰 수 있는 유동 해석 기법이 적용된 2 세대 착빙 해석 도구이다. 이를 이용하여 저속 비행을 하는 고고도 무인 항공기와 헬리콥터 동체에 발생하는 착빙 특성을 분석하였다. 그 결과 다음과 같은 결론을 이끌어 낼 수 있었다.

첫째, 저속 비행(마하수 0.1 이하)을 하는 고고도 무인기와 헬리콥터 동체에는 얼음 뿔이 발생하지 않는다. 액적은 관성력이 작아 물체와 충돌없이 회피하였고, 표면에서 생성되는 수막(water film)의 질량이 작게 생성되었다. 수막은 외부 공기의 전단력에 의해 흐르게 되고, 대류의 냉각 효과가 크게 나타나는 특정 영역에서 얼어 붙는다. 이때,

저속 특성으로 인해 열전달 계수가 전반적으로 작게 예측되고, 특정한 영역에서 수막이 얼음으로 상변화 하는 현상이 발생하지 않았다. 따라서 저속 비행 조건에서는 얼음 뿔이 발생하지 않는다.

둘째, 저중량 설계로 인하여 제빙/방빙 장치를 적용할 수 없는 고고도 무인 항공기를 위하여 착빙 환경이 제시될 경우, 항공기의 운항 가능 여부를 판단할 수 있는 새로운 기법을 제시하였다. 우선, 지상에서 임무 고도까지 상승하면서 발생한 착빙 형상과 이에 따른 공기역학적 성능 계수를 획득하고, 공기역학적 성능 계수와 착빙 환경 변수 간의 관계식을 수립하였다. 이를 통해 주어진 착빙 환경에서 임무고도까지 가기 위해 필요한 요구 동력과 탑재된 배터리의 용량을 비교함으로써 임무 성공여부를 판단할 수 있었다. 고속의 고정익 항공기는 높은 온도에서 얼음 뿔이 발생하고, 이에 의해 위험성이 고온에서 높아지는 것으로 알려져 있다. 그러나 얼음 뿔이 발생하지 않는 고고도 무인기의 경우, 습도가 높고 대기 온도가 낮은 조건에서 착빙에 의한 위험성이 증가하였다.

셋째, 헬리콥터의 동체에 발생하는 착빙을 해석할 때, 정밀한 유동 해석이 수반되어야 한다. 로터면과 동체 사이에는 상대적으로 고압, 저속의 유동 영역이 형성된다. 따라서 로터를 무시한 순수 동체와 로터의 후류를 고려한 동체에 발생하는 전체 착빙량의 경우 전체 착빙량은 물론, 착빙 분포에서 차이를 보였다. 또한 저속 비행 조건에서는 깃끝 와류와 동체가 충돌하는 영역이 발생하는데, 이러한 영역에서 많은 착빙량이 발생하였다. 따라서, 헬리콥터의 동체에 발생하는 착빙 형상을 예측하기 위하여 깃끝 와류의 생성과 이동, 동체와의 충돌 위치를 정확하게 예측할 수 있는 수치적 기법을 적용할

필요가 있다.

주요어: 항공기 착빙, 고고도 무인기, 헬리콥터 동체, ISEPAC, 압력판 기법, 압력면 기법, 블레이드 깃끝 와류, 회귀 분석

학번: 2016-30186

성명: 손찬규